

# Minimizing Actuator-Induced Residual Error in Active Space Telescope Primary Mirrors

by

Matthew William Smith

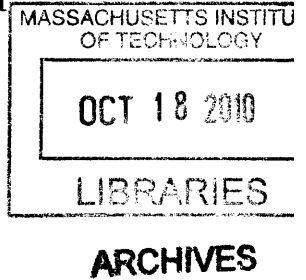
Submitted to the Department of Aeronautics and Astronautics  
in partial fulfillment of the requirements for the degree of

Master of Science in Aeronautics and Astronautics

at the

MASSACHUSETTS INSTITUTE OF TECHNOLOGY

September 2010



© Massachusetts Institute of Technology 2010. All rights reserved.

Author .....  
Department of Aeronautics and Astronautics  
August 19, 2010

Certified by .....  
David W. Miller  
Professor of Aeronautics and Astronautics  
Thesis Supervisor

Accepted by .....  
Eytan H. Modiano  
Associate Professor of Aeronautics and Astronautics  
Chair, Department Committee on Graduate Theses



# Minimizing Actuator-Induced Residual Error in Active Space Telescope Primary Mirrors

by

Matthew William Smith

Submitted to the Department of Aeronautics and Astronautics  
on August 19, 2010, in partial fulfillment of the  
requirements for the degree of  
Master of Science in Aeronautics and Astronautics

## Abstract

Heritage space telescope mirror technology—i.e. large, monolithic glass primary mirrors—has reached an upper limit on allowable aperture diameter given launch vehicle volume and mass constraints. The next generation of space telescopes will feature lightweight, actively controlled, segmented primary mirrors in order to achieve the advances in angular resolution and sensitivity that larger aperture diameters permit.

Active control via embedded surface-parallel electrostrictive actuators provides the capability to change a mirror segment's optical prescription on orbit, to correct either quasi-static disturbances or manufacturing errors. Commanding low-order prescription changes (e.g. radius of curvature) using discretely-placed actuators, however, induces high spatial frequency residual error in the mirror surface figure, resulting in wavefront error (WFE) that degrades optical performance. A key challenge is reducing this actuator-induced high frequency WFE to below acceptable levels while simultaneously commanding a particular change in global shape.

This thesis considers a new set of geometric design variables that affect high-spatial frequency residual error in an effort to mitigate actuator-induced WFE. Specifically, less conventional variations in rib height, actuator geometry, and rib-to-facesheet intersection geometry are exploited to achieve improved performance in silicon carbide (SiC) mirrors. A parametric finite element model is used to explore the trade space among these new parameters and to predict performance improvements. Simulation results show that these additional geometric considerations reduce actuator-induced WFE while keeping mirror mass and complexity constant.

Thesis Supervisor: David W. Miller  
Title: Professor of Aeronautics and Astronautics



## Acknowledgments

This work was supported by the Department of Defense and the National Aeronautics and Space Administration (NASA) Harriett G. Jenkins Pre-doctoral Fellowship Program (JPFP). I appreciate the support of these two institutions, along with the assistance provided by the United Negro College Fund (UNCF) Special Programs Corporation in administering the JPFP.

I gratefully acknowledge the invaluable advice and support of my academic advisor, Professor David Miller. I am also grateful to my fellow students on the MOST team, particularly Lucy Cohan and Thomas Gray, upon whose research this work was built. Thanks are also due to Dr. Howard MacEwen, whose expertise was much appreciated, and to fellow members of the Space Systems Laboratory (SSL)—students and staff alike—for their collaboration and camaraderie.

Finally, I am thankful for the support of my family and friends, especially Taylor Hathaway-Zepeda for her constant optimism and warmth. Special thanks are due to my mother Kathryn Smith for her selfless guidance, love, and support.



# Contents

<b>1</b>	<b>Introduction</b>	<b>19</b>
1.1	Background . . . . .	20
1.1.1	Hubble Space Telescope . . . . .	21
1.1.2	James Webb Space Telescope . . . . .	22
1.1.3	Highly integrated silicon carbide mirrors . . . . .	24
1.1.4	Summary . . . . .	25
1.2	Motivation and research objective . . . . .	26
1.3	MOST Overview . . . . .	28
1.3.1	Description of the MOST integrated model . . . . .	28
1.3.2	Prior work on MOST . . . . .	30
1.3.3	Contribution to MOST . . . . .	31
1.4	Thesis organization . . . . .	32
<b>2</b>	<b>Literature Review</b>	<b>33</b>
2.1	Finite element mirror modeling . . . . .	34
2.2	Rib-stiffened space telescope mirrors . . . . .	35
2.3	Shape optimization to decrease high frequency residual . . . . .	37
2.4	FE modeling for mirror shape optimization . . . . .	38
2.5	FE modeling of rib-stiffened mirrors . . . . .	42
2.6	Literature gap identification . . . . .	42
2.7	Summary . . . . .	43

<b>3</b>	<b>Approach</b>	<b>45</b>
3.1	Modeling process	45
3.2	Mirror model overview	47
3.3	Parameters	50
3.3.1	Optical figure	50
3.3.2	Rib geometry and terminology	53
3.3.3	Substrate	55
3.3.4	Constraints	56
3.3.5	Baseline parameters	57
3.4	Actuation	59
3.4.1	Actuator model	59
3.4.2	Influence function calculation	61
3.4.3	Command calculation	62
3.5	Figures of merit	63
3.5.1	Actuator-induced high frequency residual error (quilting)	64
3.5.2	Wavefront error (WFE)	65
3.5.3	Operational flexibility (max $\Delta$ RoC)	66
3.5.4	Strehl ratio	67
3.5.5	Figure of merit summary	70
3.6	Wavefront sensing	70
3.6.1	Shack-Hartmann wavefront sensor	71
3.6.2	Interferometry	72
3.6.3	Phase retrieval	74
3.6.4	Wavefront sensing summary	75
3.7	Validation	76
3.7.1	Mesh convergence behavior	77
3.7.2	Comparison with empirical data	78
3.7.3	Comparison with analytical models	79
3.8	Summary	79



<b>4</b>	<b>Actuator geometry</b>	<b>81</b>
4.1	Actuator length: MOST model . . . . .	81
4.1.1	Implementation . . . . .	82
4.1.2	Results . . . . .	83
4.1.3	Role of influence functions . . . . .	86
4.2	Actuator length: 1D beam model . . . . .	87
4.2.1	Pinned boundary conditions . . . . .	89
4.2.2	Rotational spring boundary conditions . . . . .	94
4.3	Number of actuators . . . . .	99
4.4	Patch actuators . . . . .	102
4.5	Summary . . . . .	105
<b>5</b>	<b>Substrate geometry</b>	<b>107</b>
5.1	Parabolic rib shaping . . . . .	108
5.1.1	Implementation . . . . .	109
5.1.2	Results . . . . .	109
5.2	Sinusoidal rib shaping . . . . .	111
5.2.1	Implementation . . . . .	111
5.2.2	Results . . . . .	112
5.2.3	Actuator length variation . . . . .	116
5.3	Rib blending . . . . .	118
5.3.1	Implementation . . . . .	119
5.3.2	Results . . . . .	120
5.3.3	Limitations . . . . .	121
5.4	Summary . . . . .	122
<b>6</b>	<b>Conclusion</b>	<b>125</b>
6.1	Thesis summary . . . . .	125
6.1.1	Modeling approach . . . . .	126
6.1.2	Results for actuator geometry variation . . . . .	127
6.1.3	Results for substrate geometry variation . . . . .	128

6.2	Thesis contributions . . . . .	130
6.3	Future work . . . . .	130

# List of Figures

1-1	(a) The Hubble Space Telescope (HST) in orbit around Earth [45] and (b) the HST primary mirror undergoing tests before the reflective surface has been applied [44]. . . . .	21
1-2	The James Webb Space Telescope (JWST) in its deployed configuration [29]. JWST has a 6.5 m diameter primary mirror formed out of 18 segments. . . . .	22
1-3	(a) The James Webb Space Telescope (JWST) primary mirror segment assembly (PMSA) showing the reaction structure [59] and (b) the arrangement of the seven actuators on each segment [29]. . . . .	23
1-4	(a) Reaction bonded SiC mirror substrate rib structure [21], (b) location of integrated surface-parallel electrostrictive actuators along the ribs [21] and (c) RoC change due to simultaneous commanding of all actuators [24]. . . . .	25
1-5	(a) Edge-on view of an un-deformed mirror with upward concavity due to its radius of curvature, (b) desired surface change for positive $\Delta\text{RoC}$ , (c) actual surface change for positive $\Delta\text{RoC}$ with discrete actuators, and (d) actuator-induced residual error (difference of b and c). . . . .	27
1-6	Main structural components of a sample MOST realization [31]. . . . .	29
1-7	Overview of the automated MOST process, adapted from [7]. . . . .	30
2-1	Three topic areas on which this thesis is based. A subset of authors and research programs is shown in each case. See text for additional authors. . . . .	33

2-2	Spherical Optical Primary Telescope (SPOT) mirror segment baseline design [4]. . . . .	38
2-3	(a) Finite element model of the baseline SPOT mirror segment and (b) surface plot of residual error (225 nm RMS, 1237 nm p-v) for 2 mm $\Delta$ RoC [4]. . . . .	39
2-4	(a) Finite element model of the optimized SPOT mirror segment and (b) surface plot of residual error (30.6 nm RMS, 198.3 nm p-v) for 2 mm $\Delta$ RoC [4]. . . . .	40
2-5	(a) Primary mirror model used by Park et al. [49] for topology optimization to minimize surface errors due to gravity loading and polishing pressure. (b) Detailed element geometry. . . . .	41
2-6	(a) Optimal density distribution and (b) corresponding verification model from Park et al. [49]. . . . .	41
3-1	Design process supported by the MOST finite element mirror model.	46
3-2	Static mirror modeling process using Matlab and MSC Nastran to simulate actuator-induced residual error. . . . .	47
3-3	Finite element mirror model; actuators are highlighted. . . . .	50
3-4	Generalized reflecting telescope geometry. . . . .	51
3-5	Parabolic reflector with focal length $f$ and spherical approximation. .	54
3-6	Mirror geometry definitions. . . . .	54
3-7	Mirror with two (a), three (b), and four (c) rib rings. . . . .	55
3-8	Point constraints used to emulate behavior of passive kinematic bipod mirror mounts. . . . .	57
3-9	Placement of actuator within mirror ribs [21] (left) and the finite element implementation using CBAR elements, zero-length RBAR elements (shown here with non-zero length), and CQUAD4 elements (right). . . . .	62
3-10	Sample influence function. . . . .	63

3-11	(a) Desired surface change for positive $\Delta\text{RoC}$ , (b) actual surface change for positive $\Delta\text{RoC}$ with discrete actuators, and (c) actuator-induced residual error (difference of a and b), termed here “actuator quilting”.	64
3-12	Geometry of residual error in a parabolic reflector. . . . .	66
3-13	(a) Pupil amplitude mask $A_{\text{pupil}}(x, y)$ and (b) phase mask $\phi_{\text{pupil}}(x, y)$ [rad] for 1 mm $\Delta\text{RoC}$ . . . . .	68
3-14	Simulated point spread functions for (a) a perfect hexagonal segment and (b) an actively-controlled hexagonal segment after commanding 1 mm $\Delta\text{RoC}$ . . . . .	69
3-15	Strehl ratio as a function of actuator quilting. . . . .	69
3-16	Shack-Hartmann wavefront sensor. . . . .	71
3-17	Twyman-Green interferometer for testing the wavefront error of a test lens $L_2$ , adapted from Hecht [36]. . . . .	73
3-18	Generalized representation of phase retrieval by iteratively transforming between the image and pupil planes while enforcing known constraints; from Dean et al. [14]. . . . .	74
3-19	Primary mirror mode frequencies as a function of mesh fidelity [31]. . . . .	77
3-20	Primary mirror quilting (42 actuator case) as a function of mesh fidelity [31]. . . . .	78
4-1	Varying actuator length $l$ in the MOST model: (a) $l = 2.4$ cm, (b) $l = 7.2$ cm (the baseline actuator length), and (c) $l = 12.0$ cm. . . . .	83
4-2	Actuator-induced quilting residual as a function of actuator length. Increasing the actuator length decreases the amount of quilting. . . . .	84
4-3	Operational flexibility (max $\Delta\text{RoC}$ ) as a function of actuator length. Increasing the actuator length increases the operational flexibility of the mirror. . . . .	84
4-4	Contour plots of actuator-induced residual due to a 1 mm $\Delta\text{RoC}$ maneuver for actuator lengths of (a) 7.2 cm and (b) 12.0 cm. The contours are in units of nanometers. . . . .	85

4-5	Overlaid slices from the residual contour plots, Figures 4-4a and b, at $y = 0$ . Vertical dashed lines show rib cell boundaries. . . . .	85
4-6	(a) Influence function for a single actuator and (b) zooming in on the local region around the actuator, which is shown as a solid black line. . . . .	86
4-7	Horizontal (a) and vertical (b) slices along the dashed lines shown in Figure 4-6b. . . . .	87
4-8	Deriving an analytical model from the mirror rib cell and actuator geometry. . . . .	88
4-9	Beam model with pinned boundary conditions. . . . .	90
4-10	Simulated deflection within a single rib cell using (a) the pinned-pinned beam model and (b) the finite element model. . . . .	94
4-11	Beam model with rotational spring boundary conditions. . . . .	95
4-12	Deflection of a clamped-clamped beam as a superposition of two clamped-free deflections. . . . .	96
4-13	Simulated deflection within a single rib cell using (a) the torsional spring beam model and (b) the finite element model. . . . .	98
4-14	Actuator-induced quilting residual as a function of number of rib rings (actuators) and actuator length. . . . .	101
4-15	Operational flexibility ( $\max \Delta RoC$ ) as a function of number of rib rings (actuators) and actuator length. . . . .	101
4-16	(a) Patch actuator implemented using 2D triangular plate elements and (b) detailed view of the patch actuator. . . . .	103
4-17	(a) Influence function of a patch actuator and (b) magnified view of the influence function. . . . .	104
5-1	Mirror with a parabolically shaped substrate; from Gray [31]. . . . .	108
5-2	Actuator-induced quilting residual as function of parabolic shaping parameter $a$ . . . . .	110
5-3	Operational flexibility ( $\max \Delta RoC$ ) as function of parabolic shaping parameter $a$ . . . . .	110

5-4	Side view of the sinusoidal shaping function applied to a set of rib cells, with shaping parameter $a$ . . . . .	111
5-5	Mirror ribs with (a) no shaping function applied and (b) sinusoidal shaping with $a = 10$ mm. . . . .	112
5-6	Actuator-induced quilting residual as function of sinusoidal shaping parameter $a$ . Quilting is minimized for $a = 12.5$ mm. . . . .	113
5-7	Operational flexibility (max $\Delta\text{RoC}$ ) as function of sinusoidal shaping parameter $a$ . Max $\Delta\text{RoC}$ is maximized for $a = 12.5$ mm. . . . .	113
5-8	Comparing residual across the mirror surface for zero rib shaping and sinusoidal shaping with $a = 12.5$ mm . . . . .	114
5-9	Zoomed view of an influence function for the case of (a) zero rib shaping and (b) sinusoidal shaping with $a = 12.5$ mm. . . . .	115
5-10	Horizontal (a) and vertical (b) slices along the dashed lines shown in Figure 5-9. . . . .	115
5-11	Actuator-induced quilting residual as function of sinusoidal shaping parameter $a$ for actuator lengths $l = \{2.4, 7.2, 12.0\}$ cm. . . . .	117
5-12	Operational flexibility (max $\Delta\text{RoC}$ ) as function of sinusoidal shaping parameter $a$ for actuator lengths $l = \{2.4, 7.2, 12.0\}$ cm. . . . .	117
5-13	Rib blending options. (a) Location of figures (b)-(d) in the mirror rib structure (white square), (b) a standard mirror rib wherein the rib-facesheet junction is $90^\circ$ , (c) rib that uses linear blending between the rib and facesheet, and (d) rib with smoothed rib-to-facesheet blending. . . . .	119
5-14	Linear rib-to-facesheet blending using 2D triangular plate elements with varying thickness. In this implementation, the facesheet thickness increases linearly from the center of the facesheet cell. . . . .	120
5-15	Zoomed view of an influence function (a) without blending and (b) with blending. . . . .	121
5-16	Horizontal (a) and vertical (b) slices along the dashed lines shown in Figure 5-15. . . . .	121

6-1	Concept for a new rib shape as an optimized sum of cosine shaping functions. A single rib cell is shown. . . . .	132
6-2	(a) Standard mirror substrate with constant rib height, (b) mirror substrate with along-rib shaping, and (c) mirror substrate with along-rib shaping and rib-to-facesheet blending. . . . .	132



# List of Tables

1.1	Comparison of space telescope primary mirror technologies [59, 29, 18, 51]. . . . .	26
3.1	Summary of reflecting telescope configurations. . . . .	52
3.2	Material properties of the SiC substrate. . . . .	55
3.3	Baseline mirror parameters. . . . .	59
3.4	Properties of the electrostrictive actuators. . . . .	60
3.5	Model performance compared to hardware test data. . . . .	78
4.1	Range of actuator lengths in units of physical distance, number of rib elements, and fraction of rib cell. Note that for the baseline mirror, the rib cell length is 14.4 cm. . . . .	82
4.2	Basic loadings and corresponding shears and bending moments, expressed using singularity functions; from Beer et al. [1]. . . . .	92
4.3	Number of actuators for a given number of rib rings. . . . .	99
4.4	Range of actuator lengths used when changing the number of actuators in a single mirror. . . . .	100
5.1	Summary of quilting results for combined shaping and actuator length variation. . . . .	118
5.2	Summary of operational flexibility (max $\Delta$ RoC) results for combined shaping and actuator length variation. . . . .	118



# Chapter 1

## Introduction

Space-based optical telescopes, like their ground-based counterparts, are typically designed with an emphasis on maximizing aperture diameter. In modern reflecting configurations (e.g. Ritchey-Chrétien [54]) the physical extent of the primary mirror defines the aperture stop. Larger apertures allow the telescope to resolve smaller objects, as given by the standard Rayleigh diffraction limit

$$\theta = \frac{1.22\lambda}{D}$$

where  $\theta$  is angular resolution,  $\lambda$  is the wavelength of interest, and  $D$  is the aperture diameter. Improved angular resolution is desirable because it allows the instrument to distinguish between closely separated point sources, or to capture the higher spatial frequency components of extended objects. Furthermore, larger apertures offer more available area to collect incident light. This is beneficial because greater photon flux generally increases the signal-to-noise ratio, providing greater sensitivity for precision science measurements such as photometry.

Therefore larger space telescope apertures offer distinct advantages with respect to resolution and sensitivity. However unlike ground systems, space telescopes are severely constrained by launch vehicle mass and volume limits. This necessitates creative design solutions for increasing aperture area with minimal corresponding mass and volume growth. One approach is the use of a low areal density segmented

primary mirror that launches in a compact stowed configuration and unfolds on orbit. In-space deployment addresses the volume constraint, while low areal density addresses the mass constraint. The challenge then becomes preserving optical performance in the presence of these design changes. For example, segmented mirrors may suffer optical errors due to incorrect phasing of the segments once deployed [52]. Likewise, low areal density mirrors have decreased stiffness, which can result in dynamic distortions of the optical figure [19].

Thus designing compact, lightweight, yet optically precise primary mirrors for space telescopes presents a significant challenge. This thesis presents solutions, particularly for the mass-constrained (i.e. low areal density) case. After discussing background information on the development of low areal density mirrors, the remainder of this chapter outlines the motivation for the work, formally states the research objective, provides a brief overview of the modeling tool used, and describes the organization for the rest of this thesis.

## 1.1 Background

Space offers an unprecedented vantage point from which to study the heavens and our own planet. Free from the turbulent atmosphere, space telescopes can observe astronomical objects with a level of detail that is barely achievable with even the most sophisticated ground-based instruments. Indeed, certain infrared observations are impossible to conduct on Earth due to atmospheric opacity in particular wavelength bands [62]. Furthermore, space provides a unique location from which to study the Earth itself. Orbital image data are of interest to the scientific, academic, military, and industrial communities in the United States and abroad.

The design of space-based optics has therefore been an active area of research and development for over 30 years and will continue to be so in the future as scientists and engineers strive for ever more capable telescopes [15, 40]. This section outlines the development of lightweight space telescope primary mirrors by considering representative cases from three generations of mirror technology. The general trend has been

a transition from relatively heavy, passive, monolithic primary mirrors to lightweight, actively controlled, segmented configurations [18].

### 1.1.1 Hubble Space Telescope

Launched in 1990, the Hubble Space Telescope (HST) is arguably NASA's flagship robotic spacecraft (see Figure 1-1a). From low Earth orbit, it observes astronomical objects primarily in the visible optical band with extensions into the near-infrared and ultraviolet [51].

With a diameter of 2.4 m, the HST primary mirror is constructed from ultra low expansion glass [35, 60]. To achieve sufficient stiffness with relatively low mass, the mirror consists of a tall but hollowed-out matrix layer of glass sandwiched between two large glass annuli, one of which serves as the reflecting surface (see figure 1-1b) [46]. The resulting primary mirror has an areal density of  $180 \text{ kg/m}^2$  and is passively stable to the required optical tolerances [59].

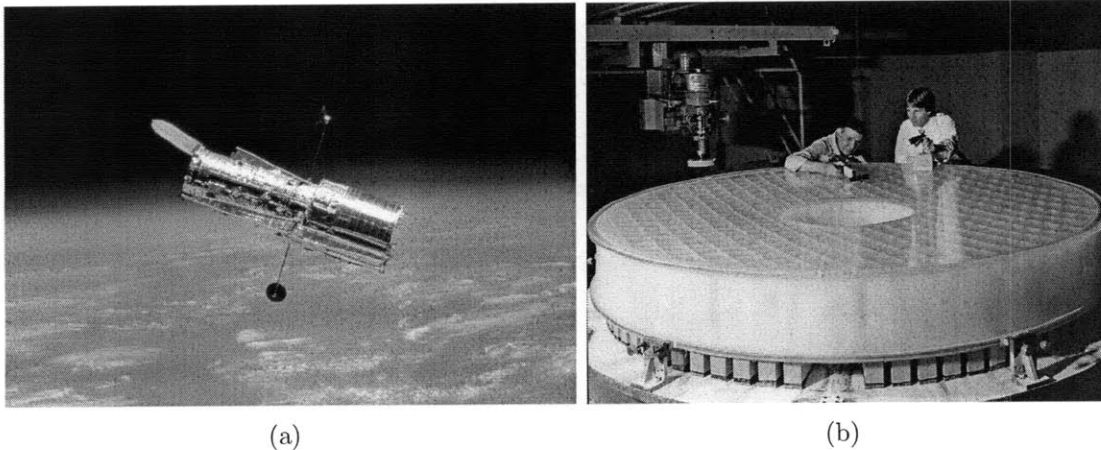


Figure 1-1: (a) The Hubble Space Telescope (HST) in orbit around Earth [45] and (b) the HST primary mirror undergoing tests before the reflective surface has been applied [44].

The HST primary mirror represents an early generation of space telescope mirror technology in which launch vehicle fairing size constrains aperture diameter, and stiffness is achieved through the bulk properties of glass itself, rather than by complex

rib structures. In these early space telescope mirrors, no segmentation is used and the mirror figure is passively stable.

### 1.1.2 James Webb Space Telescope

The James Web Space Telescope (JWST), currently targeting launch in 2014, embodies the move toward segmentation and low areal density described previously. Instead of a monolithic primary mirror, JWST uses 18 hexagonal segments to form a 6.5 m diameter aperture (see Figure 1-2). The individual segments are machined out of beryllium and consist of a thin reflective facesheet supported by an open rib back structure for stiffness (see Figure 1-3). This rib-stiffened design allows JWST to achieve an areal density of approximately  $30 \text{ kg/m}^2$  while still meeting structural rigidity requirements [60].

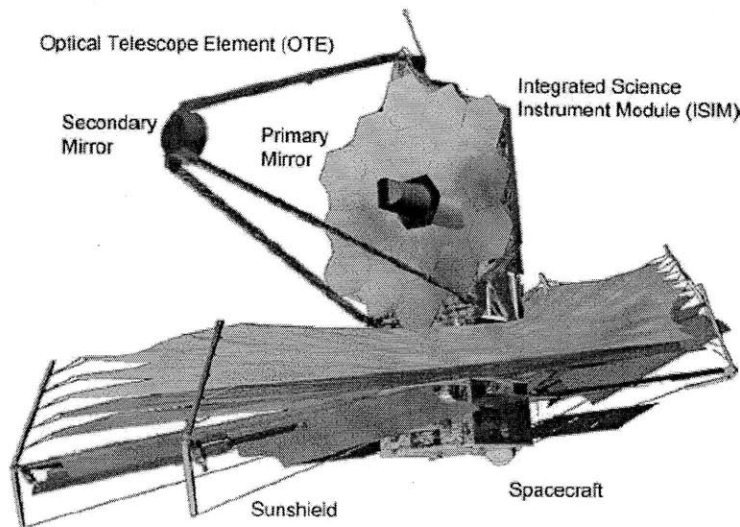


Figure 1-2: The James Webb Space Telescope (JWST) in its deployed configuration [29]. JWST has a 6.5 m diameter primary mirror formed out of 18 segments.

This segmented, rib-stiffened paradigm introduces the need for actuation. JWST launches with its primary mirror in a folded configuration. Once in space, the primary mirror unfolds and a complex series of phasing maneuvers takes place to create a single optical surface out of the 18 separate mirror segments [33]. Each segment is

actuated by cryogenic stepper motors that provide seven degrees of freedom: six rigid body movements and a radius of curvature (RoC) adjustment [29]. Note that the ability to adjust RoC relies on a rigid reaction structure against which the actuator pushes to change the segment figure (see Figure 1-3a). The seven degrees of freedom per segment are controlled during coarse and fine phasing maneuvers that together reduce primary mirror wavefront error from on the order of 1 mm root mean squared (RMS) immediately after deployment to less than 110 nm RMS once the process is complete [29].

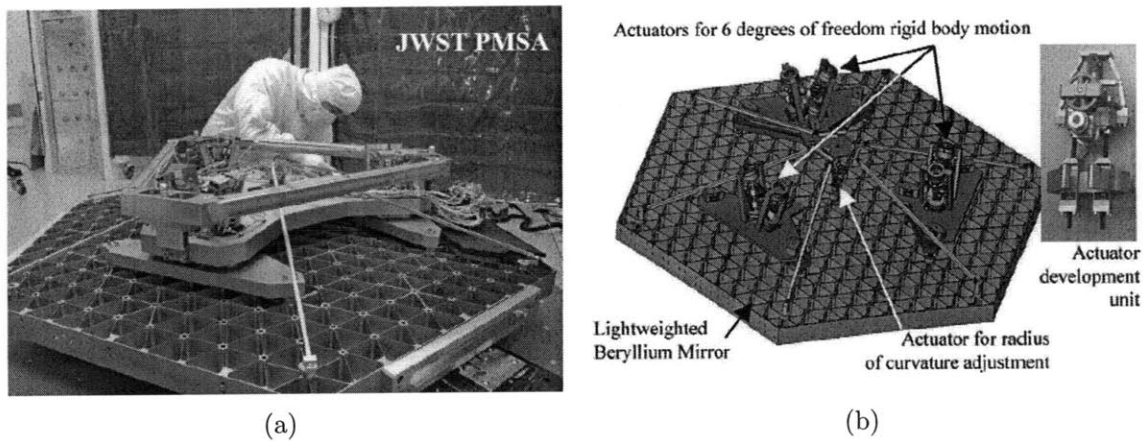


Figure 1-3: (a) The James Webb Space Telescope (JWST) primary mirror segment assembly (PMSA) showing the reaction structure [59] and (b) the arrangement of the seven actuators on each segment [29].

Note that there are several key differences between HST and JWST that make direct comparison difficult. For example, JWST is primarily an infrared observatory while HST observes in the near-infrared, visible, and ultraviolet bands. Therefore the mirror surface smoothness requirements are much more stringent in the case of HST. Furthermore, JWST is a cryogenic facility, with the entire optical assembly cooled to  $< 50$  K, compared to the 300 K operating temperature of HST's optics [60]. While these and other differences complicate any direct comparisons, JWST is nonetheless a successor both from a scientific and technological standpoint [56, 15]. With regard to space telescope primary mirrors, it represents a new generation in which segmentation and low areal density enable a revolutionary increase in aperture size.

### 1.1.3 Highly integrated silicon carbide mirrors

The JWST primary mirror still presents several challenges that limit the technology's applicability to future projects. While lightweight and stiff, beryllium is a relatively rare metal and poses manufacturing hazards due to the toxicity of beryllium powder [50]. The machining process used to create the thin rib lattice is also time consuming and expensive. Finally, the JWST RoC adjustment mechanism requires a large reaction structure against which the actuator can push or pull when changing the segment figure.

Over the past few decades, reaction bonded silicon carbide (SiC) has emerged as a promising material for space telescope mirrors [24]. It has a low coefficient of thermal expansion (CTE) relative to beryllium, which minimizes distortion; high thermal conductivity, which minimizes thermal gradients; a high elastic modulus, which provides structural stiffness; and relatively low density, which reduces mass [23]. SiC is therefore extremely well suited for in-space optical applications.

When an SiC substrate is augmented by embedded surface-parallel electrostrictive actuators, the result is a highly integrated active mirror system that can undergo changes in RoC without the need for a bulky reaction structure [20]. Furthermore, the actuators allow for on-orbit correction of figure errors due to CTE effects in a changing thermal environment. The actuators undergo a phase transition in the presence of an electric field, resulting in a lengthening or shortening [43]. This in turn causes a bending moment in the rib which alters the local curvature of the mirror. Lead-magnesium niobate (PMN) is a common actuator material because of its low (CTE), low hysteresis, and high dimensional stability [19]. Using many actuators together, it is possible to change the mirror's global RoC without the need for a reaction structure. Figure 1-4 shows the rib-stiffened substrate, the actuator locations along with outer rib edge, and a  $\Delta$ RoC maneuver accomplished by driving the actuators in a prescribed manner.

One of the primary benefits of SiC technology is its relative manufacturing ease, particularly for replicated optical elements such as primary mirror segments. Instead



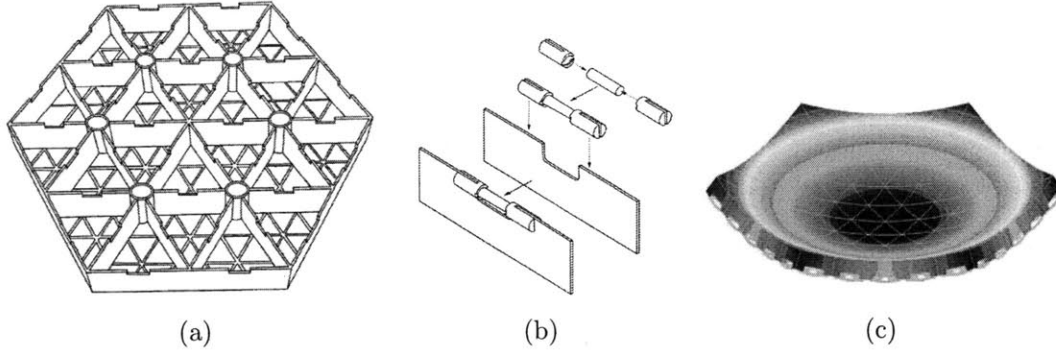


Figure 1-4: (a) Reaction bonded SiC mirror substrate rib structure [21], (b) location of integrated surface-parallel electrostrictive actuators along the ribs [21] and (c) RoC change due to simultaneous commanding of all actuators [24].

of machining from a solid piece of material as is the case with beryllium, the fabrication of SiC mirrors consists of casting the substrate into the desired shape using a mold, then firing the molded substrate to obtain a rigid mirror segment [17]. The firing process occurs at an extremely high temperature, which sinters the SiC [23]. After finish machining, a reflective nanolaminate is bonded to the facesheet, forming an optical surface [26]. The result is a lightweight precision optical element whose manufacture time and cost is low compared to other technologies.

#### 1.1.4 Summary

The general trend in space telescope primary mirrors has been a transition from passive monolithic architectures—represented by HST—to actively controlled rib-stiffened segmented configurations—represented by JWST—to highly integrated rapidly-manufacturable designs with numerous surface-parallel actuators. This evolution has continued to decrease areal density, a key design parameter for enabling large apertures in the presence of launch vehicle mass constraints. Table 1.1 summarizes this design evolution using the three representative cases described in Sections 1.1.1-1.1.3. With the exception of literature discussed in Chapter 2, the remainder of this thesis considers only rib-stiffened actively controlled SiC primary mirrors.

Table 1.1: Comparison of space telescope primary mirror technologies [59, 29, 18, 51].

Parameter	HST	JWST	Integrated SiC
Substrate material	ULE glass	Beryllium	Silicon Carbide
Aperture diameter	2.4 m	6.6 m (flat-flat)	-
Areal density	180 kg/m <sup>2</sup>	~ 30 kg/m <sup>2</sup>	< 15 kg/m <sup>2</sup>
Segmentation	None	18 segments	-
Segment diameter	n/a	1.32 m (flat-flat)	1 m (flat-flat, baseline)
Figure control	Passive	Active	Active
Actuator technology	n/a	Cryo. stepper motors	Electrostrictive
Actuator DOF	n/a	6 rigid + $\Delta$ RoC	> 100

## 1.2 Motivation and research objective

While highly integrated active SiC mirrors offer tremendous promise in terms of low areal density, complications arise as a result of actuator behavior. Specifically, the discrete placement and local influence of the actuators makes it difficult to command perfectly smooth low-order changes such as RoC adjustments.

Consider the initially unactuated mirror shown edge-on in Figure 1-5a. A phasing maneuver may require an increase in RoC. This is equivalent to seeking the mirror surface displacements shown in Figure 1-5b: for an increase in RoC, the mirror is flattened by commanding the edges to deflect downward relative to the center. Because of the discrete placement and localized influence of the actuators, however, the actual displacement is the shape shown in Figure 1-5c. Instead of being smooth, the actual displacements more closely resemble the surface of a golf ball, with the actuators introducing an unwanted high spatial frequency variation on top of the desired low order shape change. The difference between the optically perfect desired surface change and the actual surface change is termed *actuator-induced residual error*, and is shown in Figure 1-5d. This residual error acts as an optical aberration, degrading the image quality.

The severity of actuator-induced residual is dependent on the magnitude of the  $\Delta$ RoC maneuver, with larger changes in RoC causing more residual. Generally, a

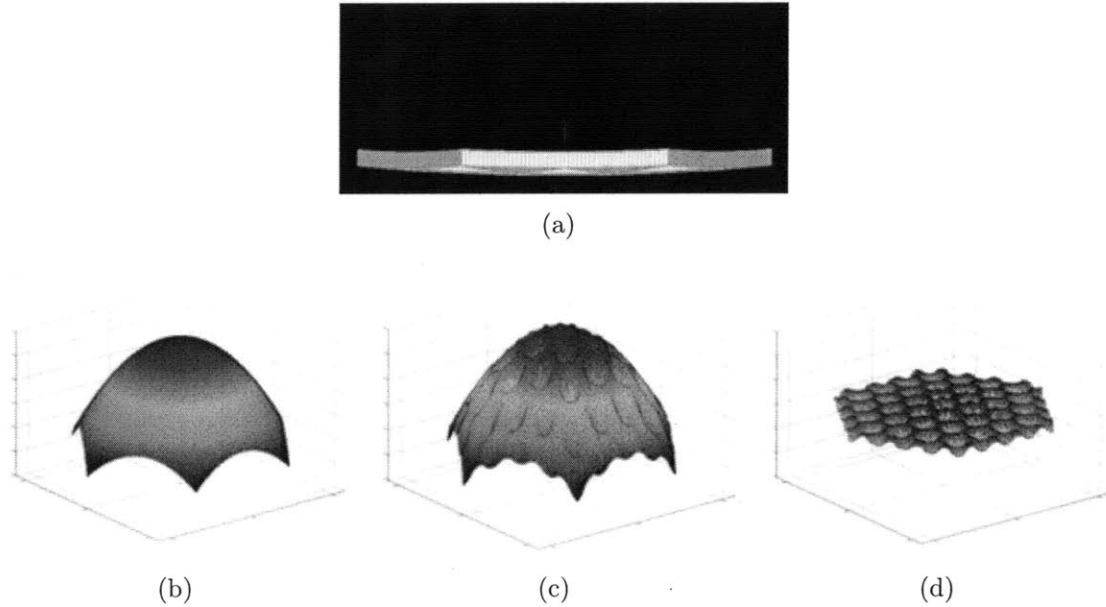


Figure 1-5: (a) Edge-on view of an un-deformed mirror with upward concavity due to its radius of curvature, (b) desired surface change for positive  $\Delta\text{RoC}$ , (c) actual surface change for positive  $\Delta\text{RoC}$  with discrete actuators, and (d) actuator-induced residual error (difference of b and c).

larger range of attainable RoC settings is desirable, as it improves operational flexibility on-orbit by allowing the primary mirror to compensate for greater segment mismatch due to manufacturing or phasing errors. It also allows the mirror to compensate for larger changes in the thermal environment that would otherwise alter its figure.

Thus the challenge is to preserve an ability to alter the mirror shape on-orbit, while simultaneously reducing high spatial frequency residual error caused by the actuators. If actuator-induced residual is too large, the operational benefits from having an adjustable radius of curvature are quickly negated. Furthermore, any residual mitigation should ideally be accomplished without adding mass or complexity to the mirror system. Recent work [31, 4] points to creative design of mirror geometry via finite element modeling as one possible way to decrease actuator-induced residual. Therefore the research objective of this thesis is the following: *to reduce actuator-induced high spatial frequency residual error by manipulating mirror geometry using a parametric finite element model, while keeping areal density and number of actuators*

*constant.*

## 1.3 MOST Overview

The Modular Optical Space Telescope (MOST) integrated model is a parametric finite element-based tool for exploring the tradespace of space telescope designs. It is the primary modeling tool used in this work. MOST features a high fidelity primary mirror model suitable for more detailed analysis and optimization of mirror configurations. This section briefly describes MOST, prior work using the model, and the contribution of this thesis to MOST.

Developed by the Space Systems Laboratory (SSL) at the Massachusetts Institute of Technology (MIT), MOST is a parametric tool to assist in the preliminary design of next-generation, lightweight space telescopes. The model allows rapid generation of unique spacecraft realizations across a user-defined trade space. Particularly at the early stages of space telescope design, there are many trades involving system parameters such as areal density, segment geometry, f-number, and mirror diameter. The interaction between these parameters is not immediately obvious and traditional design techniques are unlikely to find optimal solutions [65]. Parametric modeling is therefore needed to capture the complex interactions between design variables. Furthermore, next-generation space telescopes will use new technologies such as active control of lightweight, flexible structures to achieve low mass [9]. The MOST modeling environment allows the designer to incorporate these new approaches and evaluate the ability of a system with limited heritage to meet requirements.

### 1.3.1 Description of the MOST integrated model

Given a set of user-defined design parameters, the MOST model automatically generates the structural design of space telescope via Nastran, adds representative dynamic disturbances, simulates the application of control laws to mitigate such disturbances, and computes figures-of-merit that quantify the ability of an individual design to meet requirements. While MOST realizations can vary substantially, certain parameters

are invariant. The telescope is assumed to be in a Cassegrain configuration and it operates in the visible portion of the spectrum (nominal  $\lambda = 600$  nm). All realizations consist of an optical telescope assembly (OTA) containing the optical elements, and a spacecraft bus containing supporting subsystems. The latter is modeled as a collection of discretely located point masses using historical data as benchmarks. Figure 1-6 below shows a representative MOST realization.

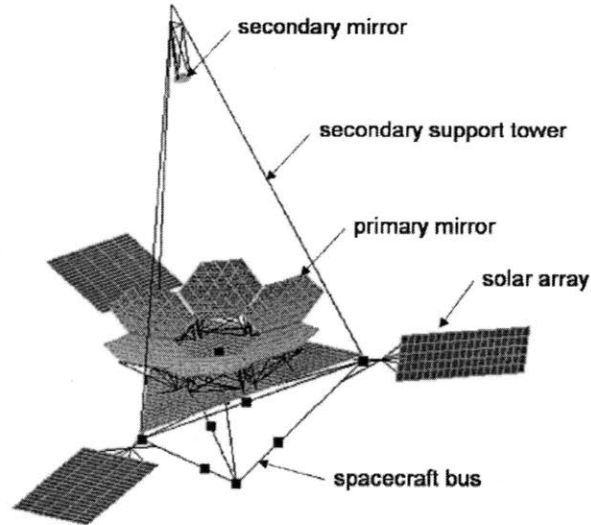


Figure 1-6: Main structural components of a sample MOST realization [31].

MOST is implemented as a modular collection of MATLAB functions that interact to construct and analyze the telescope model. All input parameters are stored in a single top-level input file which is then passed to the various modules. This modularity allows for the easy addition of new structural features, control systems, analysis routines, and operational environments. Performance metrics are calculated automatically to the specification of the user. Figures of merit are discussed in Chapter 3, but typical MOST outputs include line-of-sight (LOS) jitter, wavefront error (WFE), slew and settle time, control effort, stability margin, and mass. An overview of the MOST modeling and analysis process is shown in Figure 1-7.

MOST features a detailed finite element representation of a parabolic primary mirror. It is modeled after the highly integrated SiC architecture described in Section 1.1.3. Therefore the primary mirror model contains a rib-stiffened substrate

with embedded surface parallel electrostrictive actuators along the ribs. The investigations performed for this thesis use only the high fidelity primary mirror model, which Chapter 3 describes in detail; the spacecraft bus is not considered.

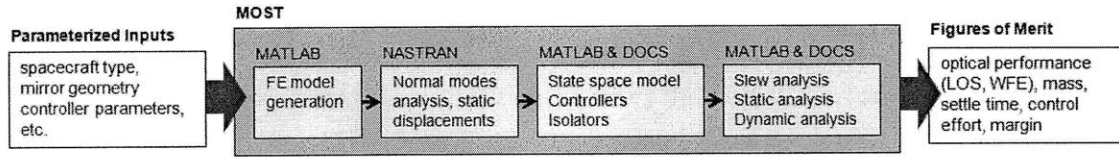


Figure 1-7: Overview of the automated MOST process, adapted from [7].

### 1.3.2 Prior work on MOST

Given its modularity and flexibility, the MOST model is well suited to a range of system-level analyses. Past work has focused primarily on trade space exploration and control design for a variety of disturbance environments. This section summarizes work on MOST that is not directly related to the present study but that still provides a useful context for the thesis. A comprehensive review of more closely-related literature is given in Chapter 2.

The MOST model has been used in the design of control systems for active space telescopes. Multiple control systems can be used to correct for dynamic errors, which include attitude control, fast steering mirror jitter control, and dynamic wavefront control. Cohan [7, 6] used the model to consider all control systems simultaneously with the goal of optimizing the entire control architecture, considering both performance gains and control costs, such as loss of stability margin.

Cohan [7, 10] also used the model to study the potential benefits of dynamic wavefront control for space telescopes. She demonstrates that wavefront error can be corrected through the use of the embedded actuators and rigid-body mirror segment control. The active wavefront control system considered uses a positive position feedback (PPF) controller for rigid body segment motion and a robust linear quadratic Gaussian (LQG) controller for figure control. Improvement in WFE of up to approx-

imately 50% was obtained without violating stability margin constraints.

Jordan [37, 38] employed the MOST model to investigate the use of embedded strain gauges and temperature sensors to measure mirror surface figure directly, as an alternative to optical wavefront sensing schemes (e.g. Shack-Hartman sensors). Control schemes using both strain gauges and temperature sensors are considered, however it was shown that using the latter alone, it is possible to reduce thermally-induced wavefront error from on the order of 1000 nm RMS to 10 nm RMS.

Finally, the MOST model has also been used for trade space analysis and optimization by varying the many different design parameters simultaneously. As described above, this method can be used during the conceptual design phase and results in an understanding of the trade space far earlier in the design process than with traditional approaches. Additionally, uncertainty is also considered in the early stages of design. Design of Experiments methods and analysis of variance have been used to identify critical uncertainty parameters. These parameter uncertainties are then propagated through the model in order to bound the uncertainty in the performance [64]. By using model-based analysis methods, this approach to conceptual design results in the early identification of superior architectures that are robust to uncertainty [63, 9].

### 1.3.3 Contribution to MOST

This work contributes to the primary mirror modeling aspect of MOST, specifically regarding rib-stiffened hexagonal segments with embedded surface-parallel actuators. It considers actuator-induced high spatial frequency residual error and arrives at designs that mitigate this effect through careful specification of actuator and segment geometry.

In particular, this thesis studies variation of actuator length and provides an analytical framework for explaining the role of actuator length in mirror controllability. In doing so, it evaluates the ability to change optical prescription to meet operational needs. Creative segment geometry, specifically rib shaping and rib-to-facesheet blending, is also used to reduce actuator-induced residual. Again the goal is to place bounds on the range of prescription changes available via surface-parallel actuation,

given limits on acceptable wavefront error.

## 1.4 Thesis organization

This thesis presents designs and design approaches that reduce actuator-induced residual errors in lightweight, rib-stiffened, actively controlled mirrors. Chapter 2 presents a review of relevant literature, including prior work in finite element mirror modeling and mirror shape optimization. A gap in the literature is identified, which motivates the present study.

Chapter 3 contains an overview of the modeling approach used. The model parameters (e.g. rib geometry, substrate, constraints, etc.) are discussed in detail, as are the actuators, figures of merit, and sensing methods. This chapter also discusses model validation.

Chapter 4 discusses the effect of changing actuator geometry. Specifically, the beneficial effect of lengthening surface-parallel actuators is identified and analyzed. The results are based both on finite element modeling and a one dimensional beam model. Two dimensional “patch” actuators are also discussed.

Chapter 5 presents results relating to changes in substrate geometry. Several methods are used to alter the shape of the rib back structure. Variations in rib height are shown to affect actuator-induced residual, as are changes in rib-to-facesheet blending. The combined effect of actuator lengthening and rib shaping is presented.

Finally, Chapter 6 offers a summary of the work, including main results and recommendations for designs that mitigate actuator-induced residual. Specific thesis contributions are given, along with several suggested topics of future work.



# Chapter 2

## Literature Review

This chapter summarizes prior work in the area of lightweight mirror design. The contributing literature is categorized into three main topics: finite element mirror modeling, rib-stiffened space telescope mirrors, and shape optimization to decrease high frequency residual. The research described in this thesis draws on all three areas (see Figure 2-1).

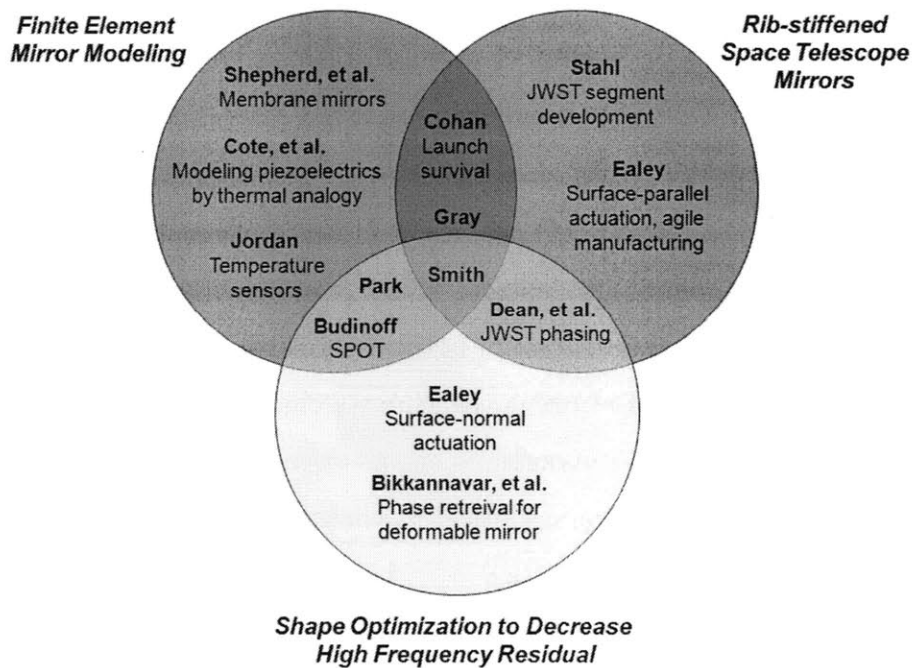


Figure 2-1: Three topic areas on which this thesis is based. A subset of authors and research programs is shown in each case. See text for additional authors.

The sections below first describe the literature that falls exclusively within a single topic area in Figure 2-1. Then the intersections between multiple topic areas are discussed, with particular emphasis on the Spherical Primary Optical Telescope (SPOT) primary mirror segment [4], prior MOST mirror design studies [12, 8, 32, 31], and topology optimization for residual mitigation (Park et al. [49]). A gap in the literature is identified wherein the substrate shaping approach used in SPOT and Park et al. is applicable to the MOST rib-stiffened mirror model. This gap is used to contextualize and motivate the research effort described in later chapters.

## 2.1 Finite element mirror modeling

Finite element models are an essential tool in structural design and have been used to explore a number of advanced lightweight mirror concepts. This topic area is represented by the upper left-hand circle in Figure 2-1. Shepherd et al. [58] apply finite element models to the case of membrane mirrors. Their work discusses the utilization of two different basis systems for the description of membrane mirror displacements: Zernike polynomials and Bessel functions. The authors employ a piezoelectrically-actuated membrane mirror model implemented using MSC Nastran to calculate the static displacements of the mirror surface.

Thermal analysis is a common application of finite element modeling in mirror design. Nied and Rudmann [46] illustrate how instantaneous coefficients of thermal expansion (CTE) were taken into account in the design of the HST primary mirror. By incorporating CTE spatial variations in their finite element model, the authors predict the effect of thermally induced distortions on the mirror surface figure. The authors point out that prior to their work, optical-mechanical analysis of optical elements occurred in three distinct phases: thermal, structural, and optical. While combined structural and optical studies had been conducted previously, Nied and Rudmann are novel in adapting a more multi-disciplinary approach that combines structural, thermal, and optical considerations into a single analysis of space telescope mirrors.

The thermal modeling capability of Nastran has also been used to model elec-

trostrictive actuators through thermal analogy. Côté et al. [13] exploit an exact correspondence between thermal and piezoelectric strains to model an active piezoelectric composite structure using MSC Nastran. They show that the voltage actuation of an electrostrictive ceramic can be simulated using the thermal strain properties of finite elements. Their work also includes experimental validation of the simulation results. Modeling by thermal analogy is useful, as Nastran lacks native support for piezoelectric materials but does incorporate material CTE. Thermal analogy is therefore the actuator modeling approach used in MOST and this thesis. Details and potential drawbacks of the method are discussed in Section 3.4.1.

Finally, Jordan [37, 38] uses a finite element plate model in MOST to study the effects of thermal disturbances on the shape of a SiC mirror. The author considers low-order temperature distributions over the mirror surface and the resulting quasi-static thermal distortions. Instead of feedback from an optical wavefront sensor, a novel approach is presented that uses embedded temperature sensors and strain gauges as inputs to the mirror control law. Simulation results show that correction is possible using these non-traditional sensors.

## 2.2 Rib-stiffened space telescope mirrors

An essential means of decreasing space telescope primary mirror mass is the utilization of rib-stiffened designs. This topic area is represented by the upper right-hand circle in Figure 2-1. As exemplified by the designs discussed in Sections 1.1.2 and 1.1.3, rib-stiffened mirrors consist of a thin reflective facesheet supported by a lattice of relatively thin ribs that provide structural support without high mass. As also discussed above, active control becomes necessary in such designs in order to phase segments or remove figure errors due to on-orbit disturbances.

A robust technology development program over the past decade and a half has steadily increased the technology readiness level (TRL) of rib-stiffened space telescope mirrors [59]. The Subscale Beryllium Mirror Demonstrator (SBMD), built by Ball Aerospace & Technologies Corporation and tested at Marshall Space Flight Center

(MSFC), demonstrated enabling technologies for lightweight cryogenic mirrors as a precursor to JWST. With a diameter of approximately 0.5 m and an adjustable RoC, the SBMD demonstrated, among other requirements, a surface figure roughness of less than  $\lambda/4$  peak to valley (p-v) at  $\lambda = 633$  nm under cryogenic vacuum conditions [53]. Experience from SBMD was applied to the Advanced Mirror System Demonstrator (AMSD), a 1.4 m diameter rib-stiffened beryllium hexagonal mirror segment with four degrees of freedom (piston, tip/tilt,  $\Delta$ RoC). Cryogenic performance of this mirror also met requirements and results were used to guide JWST segment design [5].

The current state of the art in rib-stiffened beryllium mirrors is the JWST segmented primary. The Primary Mirror Segment Assembly (PMSA) was a technology pathfinder that demonstrated a Technology Readiness Level (TRL) of 6 for the JWST primary mirror by verifying segment requirements in the relevant environment [60]. Design elements whose TRL-6 compliance was demonstrated include areal density, figure thermal stability, optical coating cryo-survivability, and surface figure error [59]. Details of the JWST segment fabrication process are discussed by Parsonage [50].

As discussed in Section 1.1.3, reaction bonded SiC is a promising substrate material for future rib-stiffened space telescope mirrors due to its advantages in terms of performance and manufacturing ease. Ealey and Northrop Grumman Xinetics have been at the forefront of rib-stiffened SiC mirror design and fabrication over the past decade and a half, having obtained the relevant intellectual property from United Technologies Corporation in 1995 and subsequently developed the technology since [23, 18]. Ealey et al. [17, 67, 26] describe an agile substrate casting process wherein mirror blanks can be fabricated in weeks rather than the months or years required for other optical materials. Likewise, Mulvihill and Ealey [43] describe the fabrication of electrostrictive actuators. Combining the substrate and actuators in the manner described in Section 1.1.3 yields a low mass, highly integrated meniscus mirror for space telescope applications [24, 19, 20].

## 2.3 Shape optimization to decrease high frequency residual

A number of authors have sought to decrease high frequency residual error in optical systems by optimizing the shape of various reflective elements. This topic area is represented by the lower circle in Figure 2-1. Ealey et al. [22, 25] have developed thin facesheet deformable mirrors driven by surface-normal actuators that serve this purpose. The actuator spatial density and high actuator bandwidth make these mirror well suited to remove residual errors that occur at high spatial and temporal frequencies. This technology finds extensive application in ground-based adaptive optics (AO).

Oppenheimer et al. [48] investigate the performance of a thin facesheet a deformable mirror on the Hale Telescope AO system at Palomar Mountain Observatory. The deformable mirror is downstream of the primary and secondary mirrors, with optical path difference (OPD) measurements from a Shack-Hartmann wavefront sensor. The goal if this system is to correct for time-varying high spatial frequency aberrations due to atmospheric turbulence. It should be noted that these thin facesheet surface-normal mirrors have typical diameters on the order of tens of centimeters and are used in astronomical AO systems operating at bandwidths in the kilohertz range. This is distinct from *active* optics, which is the term applied to the much lower bandwidth case of on-orbit actively controlled primary mirrors.

Still, the principles of shape optimization are applicable in both regimes. Bikkannavar et al. [2] use the Palomar deformable mirror to remove quasi-static non-common path errors in optics between the wavefront sensor and the science camera. This is accomplished using iterative phase retrieval with the science camera to optimize the deformable mirror shape. Feinberg et al. [27] use the same technique as the baseline JWST fine phasing algorithm, in which case the active mirror is a rib-stiffened design, rather than the thin facesheet surface-normal construction.

## 2.4 FE modeling for mirror shape optimization

Of particular interest to this thesis is the intersection between finite element modeling and mirror shape optimization (see Figure 2-1). It is difficult to optimize mirror shapes quickly or cost effectively using hardware iteration. Designing a mirror, fabricating it, performing the necessary analysis, and repeating this process is simply too costly. Furthermore, it constrains the tradespace to a small number of points, potentially eliminating higher-performing designs that were not explored. Finite element models, particularly when parameterized for rapid and automated trade space exploration, provide a solution. Design iteration then occurs in software and only the final optimized configuration is implemented in hardware.

The work of Budinoff and Michels [4] on the Spherical Primary Optical Telescope (SPOT) primary mirror segment provides a highly relevant example of the above process. Each SPOT segment consists of a 0.86 m (point-to-point) substrate with a single linear surface-normal actuator affixed to the non-reflecting side (See Figure 2-2). Extending or contracting the actuator causes the center of the mirror to move relative to the edges, which are connected to the actuator by rigid struts. The result is a change in RoC.

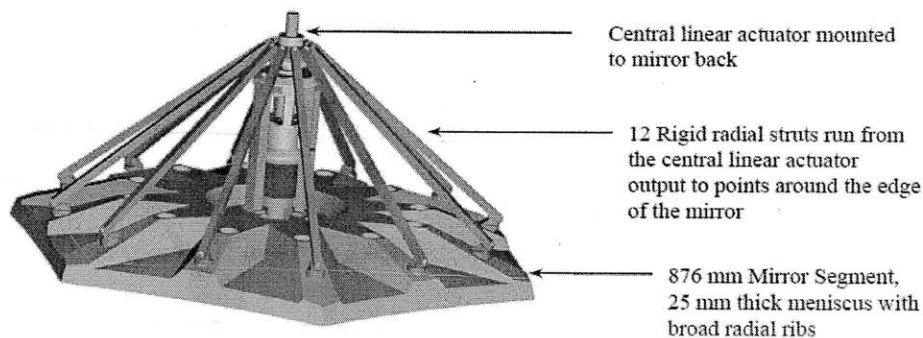


Figure 2-2: Spherical Optical Primary Telescope (SPOT) mirror segment baseline design [4].

Using MSC Nastran, the authors created a finite element model of the baseline design, including the RoC actuator and rigid struts. The design was found to produce

an unacceptably high amount of actuator-induced residual error when RoC changes were commanded (see Figure 2-3).

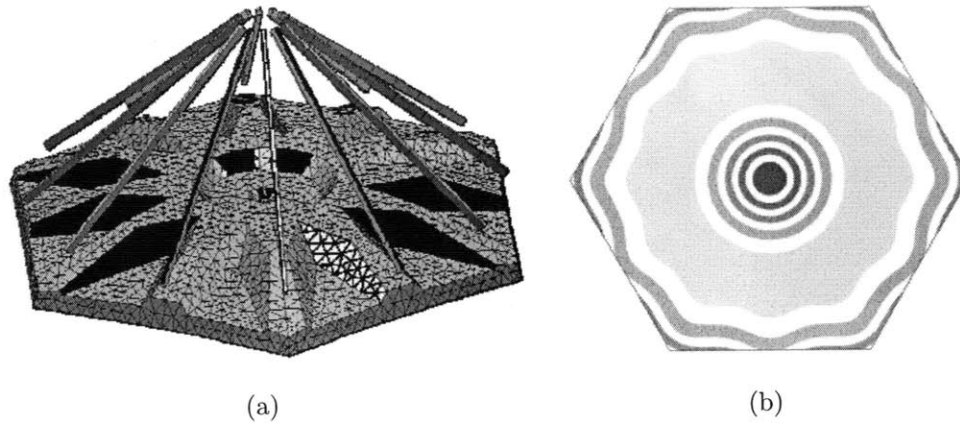


Figure 2-3: (a) Finite element model of the baseline SPOT mirror segment and (b) surface plot of residual error (225 nm RMS, 1237 nm p-v) for 2 mm  $\Delta$  RoC [4].

The substrate is fabricated by casting hot Pyrex using a mold of the segment. The segment substrate shape can therefore be controlled by altering the mold. Given the poor residual performance of the baseline design, Budinoff and Michels seek to take advantage of this manufacturing flexibility by varying the shape of the mirror back to reduce actuator-induced errors. The authors parameterized the shape of the mirror back using a summation of basis functions defined in polar coordinates. The shape function  $f$  takes the general form,

$$\begin{aligned}
 f(r, \theta) = & a_0 + a_1r + a_2r^2 + a_3r^3 + a_4r^4 + \\
 & (b_1r + b_2r^2 + b_3r^3 + b_4r^4) \cos(6\theta) + \\
 & (c_1r + c_2r^2 + c_3r^3 + c_4r^4) \cos(12\theta)
 \end{aligned}
 \tag{2.1}$$

i.e. a radially-varying power series with circumferentially-varying oscillations corresponding to the 6- and 12-fold symmetry of the segment and struts. The coefficients  $a_i$ ,  $b_i$  and  $c_i$  are design parameters, as are the locations of the attachment points between the mirror and actuator struts. An optimization routine is used to solve for the values of these design variables that minimized actuator-induced residual. The

resulting mirror back shape and post-actuation residual are shown in Figure 2-4. For 2 mm  $\Delta\text{RoC}$ , surface error was reduced from 225 nm RMS to 30.6 nm RMS.

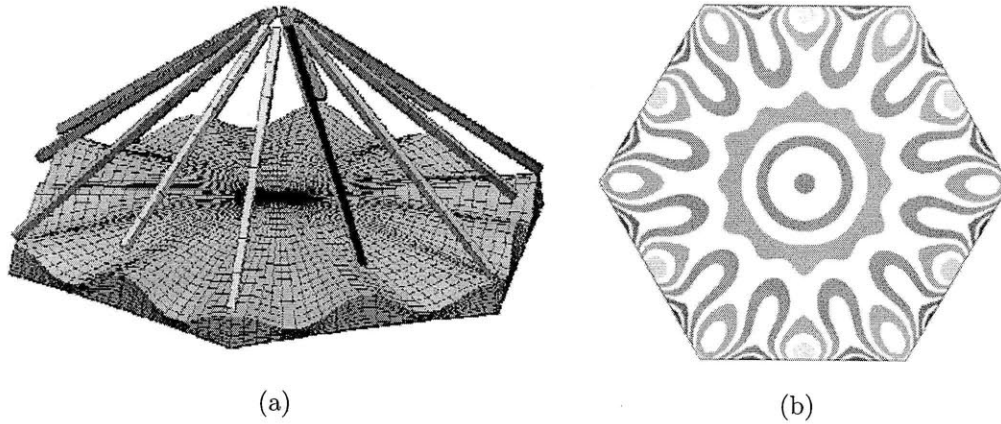


Figure 2-4: (a) Finite element model of the optimized SPOT mirror segment and (b) surface plot of residual error (30.6 nm RMS, 198.3 nm p-v) for 2 mm  $\Delta\text{RoC}$  [4].

The work of Park et al. [49] is a similarly relevant example of geometry optimization using FE modeling to reduce mirror residual. In this case, however, the authors attempt to mitigate errors due to gravity sag and manufacturing print-through rather than actuator effects. Also, it should be noted that this mirror does not contain any actuators; rather, it relies on passive dimensional stiffness for control of the optical figure.

Instead of parameterizing the substrate according to a set of basis functions that define the shape, Park et al. parameterize by the material density at all points in the structure. Discretization is introduced by the authors' use of finite elements to represent the substrate. Three dimensional volume elements are used to create a mirror model with an arbitrarily variable density pattern. The geometry of the FE model is shown in Figure 2-5.

The authors seek to minimize the RMS surface error via optimization. The design variables are the material densities in the individual volume elements. Their results show a monotonic decrease in the RMS surface error from 90 nm to 39.4 nm. A verification model is manufactured using Zerodur, a low-expansion glass ceramic. The optimal density distribution is incorporated into this verification model, which



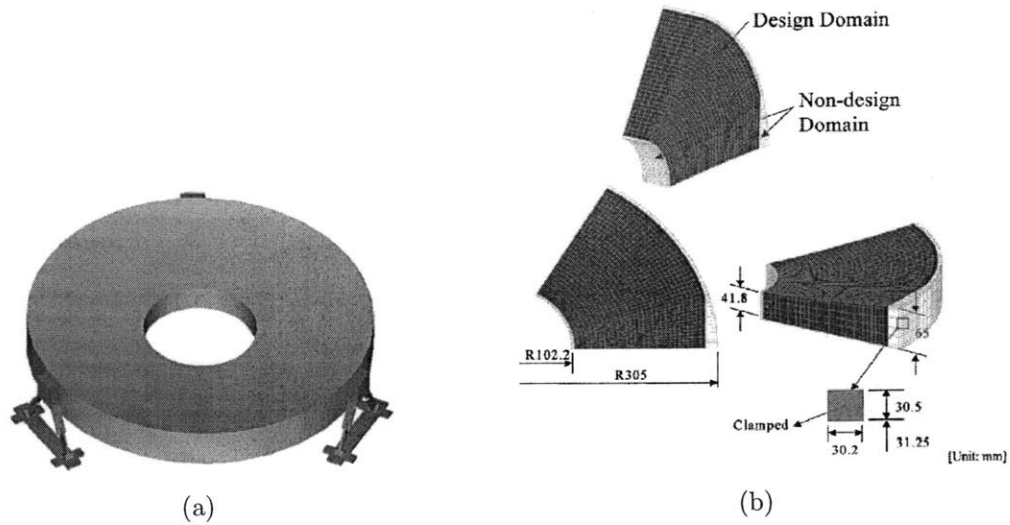


Figure 2-5: (a) Primary mirror model used by Park et al. [49] for topology optimization to minimize surface errors due to gravity loading and polishing pressure. (b) Detailed element geometry.

due to manufacturing constraints has a mass ratio with respect to the non-optimized mirror of 35% (rather than the theoretical 22% predicted by the optimization routine). Comparing the verification model to a more typical hexagonal cell mirror, the authors find a 22.1 nm RMS (14%) improvement with respect to errors due to polishing pressure loading. The optimal density distribution and corresponding verification model are shown in Figure 2-6.

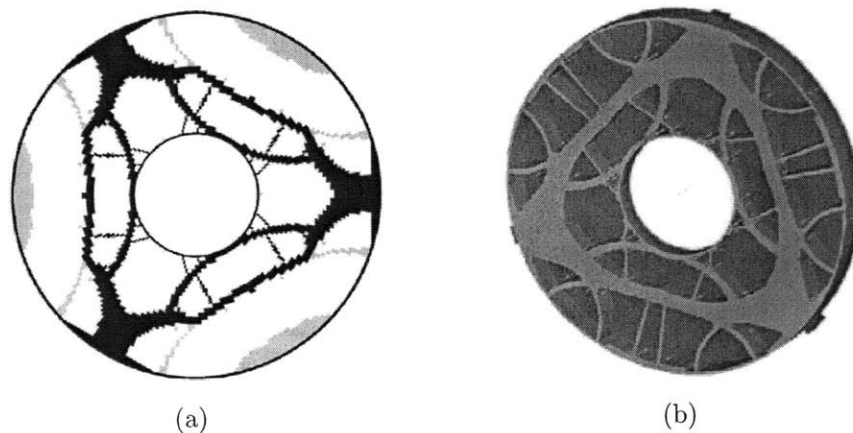


Figure 2-6: (a) Optimal density distribution and (b) corresponding verification model from Park et al. [49].

## 2.5 FE modeling of rib-stiffened mirrors

Also of significant interest to this thesis is the interaction between finite element modeling and rib-stiffened mirror design (see Figure 2-1). A bulk of the recent work on MOST lies at this intersection. Cohan [8, 11, 12] has used a parametric active primary mirror model to determine optimal designs for launch survivability and on-orbit performance. Tailoring a mirror design for launch survival produces a mirror that is not optimal for on-orbit operations, and vice versa. Hence integrated modeling becomes essential for designing a mirror that is suitable for both environments. Cohan also demonstrates several launch load alleviation techniques, such as resistive shunting and active damping, both using the embedded electrostrictive actuators.

Like Cohan, work by Gray [31, 32] lies at the intersection of finite element modeling and rib-stiffened lightweight mirror design. However, in the latter case there is a greater emphasis on optimizing the mirror shape to mitigate residual errors. Gray simulates the effects of two high spatial frequency error sources using the MOST finite element mirror model: manufacturing-induced print-through and actuator-induced quilting (see Section 3.5.1 for a description of the later). Single-axis trades are conducted with respect to mirror areal density, f-number, and actuator length to document the effect of these design parameters on the modeled error sources. After determining the parameters with the largest influence on overall residual error, optimizations are carried out to derive a set of optimal design relationships that minimize uncorrectable high spatial frequency error while satisfying manufacturing constraints.

## 2.6 Literature gap identification

A gap in the literature exists at the intersection between finite element mirror modeling, design of rib-stiffened mirrors, and shape optimization for mitigating residual. Specifically, there are no attempts in the literature to apply the mirror shaping approach for residual mitigation embodied by SPOT to the case of rib-stiffened SiC mirrors. Gray began the process of exploring this gap through the optimizations de-

scribed above. It was demonstrated that mirror geometry (e.g. rib aspect ratio) could be exploited to reduce high spatial frequency residual errors, including those caused by actuator effects. However, the potential benefits of more extreme shape variations remain relatively unexplored for the case of rib-stiffened mirrors. SPOT showed that optimization over additional geometric parameters can significantly reduce actuator-induced residual, albeit using a different actuator and substrate technology. Utilizing a suitably large number of geometric design variables was key to success in the SPOT optimization process [41]. Likewise, Park et al. spatially vary the mirror substrate density. The same approach has not been thoroughly explored in the literature on rib-stiffened designs. This thesis will address the identified research gap between Gray, Budinoff, and Park by utilizing additional geometric variations to reduce actuator-induced residual error in rib-stiffened mirror segments.

## 2.7 Summary

The contributing literature for this thesis has been separated into three topic areas: (1) finite element mirror modeling, (2) rib-stiffened space telescope mirrors, and (3) shape optimization to decrease high frequency residual. Gray uses limited geometrical optimization to minimize two types of high spatial frequency residual—manufacturing-induced print through and actuator-induced quilting—and other work points to the benefits of exploring additional geometric design parameters. Specifically, the SPOT mirror segment provides an example wherein unconventional geometric design changes led to a reduction in actuator-induced residual. Similarly, Park et al. show that geometry optimization can reduce static residual in lightweight passive mirrors. This thesis follows on the combined work of Gray, Budinoff, and Park in using geometrical variation as a means to reduce actuator-induced residual error in SiC space telescope mirrors.



# Chapter 3

## Approach

The literature gap identified in Chapter 2 motivates and contextualizes the research objective of this thesis: to reduce actuator-induced high spatial frequency residual error in active space telescope mirrors by manipulating mirror geometry. Furthermore, it is desirable to accomplish this while keeping areal density and number of actuators constant. This chapter describes the approach adopted by this thesis, namely the use of a parametric finite element (FE) mirror model. An overview of the modeling process is presented, followed by details concerning model parameters and geometry, actuation, figures of merit, and wavefront sensing. The chapter then concludes with a discussion of model verification.

### 3.1 Modeling process

The MOST mirror model is a finite element representation of a rib-stiffened actively controlled SiC space telescope mirror of the type described in Section 1.1.3. The utility of the model lies in its parametric nature: by changing a single input variable, the user can alter global parameters such as segment diameter, rib geometry, actuator distribution, etc. Because the model code automatically generates a new finite element mirror representation, this process is much less time consuming and burdensome to the user than it would be if the grid points and elements were changed by hand. In this way, parametrization allows for rapid trade space generation, design iteration,

and optimization. Figure 3-1 depicts this process. Note that the figure shows the static analysis case, which is used in this thesis given that the mirror is correcting quasi-static disturbances such as thermal deformation or segment RoC mismatch. For examples of the MOST mirror model being used for dynamic analysis, see Cohan [7, 8, 12] and Jordan [37].

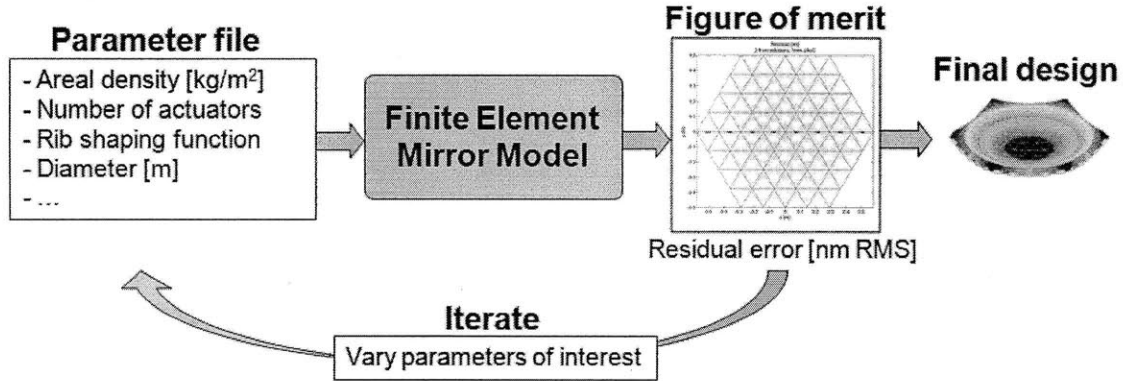


Figure 3-1: Design process supported by the MOST finite element mirror model.

The design process begins with the user creating a single parameter file that contains global parameters describing the mirror geometry, materials, actuator layout, finite element mesh density, and other aspects of the mirror. Parameters relevant to this thesis are discussed further in Section 3.3. The parameter file is passed to the model, which automatically generates a finite element representation of the mirror and computes the desired figures of merit. Figure 3-1 shows residual error as one example but others are possible. Figures of merit are discussed in Section 3.5.

The path from parameter file to FE mirror model to figure of merit reflects a single model execution. The model-based design process adds an iteration loop in which the user varies parameters of interest in an effort to identify mirror configurations that maximize performance, minimize cost, or otherwise meet requirements. The iteration loop can be used to populate a multi-dimensional objective space, after which Pareto-efficient designs may be identified [8, 64]. Alternatively, the iteration loop can take the form of an optimization routine that traces a path through the

trade space to an optimal design [31]. After the iteration process is complete, the final mirror configuration can be carried into the next phase of development (e.g. additional detailed design work or fabrication and testing). This model-based process is faster and less time consuming than hardware-intensive design studies and considers a larger region of the trade space. See Cohan [8] for a more extensive discussion of model-based design using MOST.

### 3.2 Mirror model overview

This section considers modeling steps conducted within the finite element mirror model itself, i.e. those processes that are abstracted in Figure 3-1 to a single box. Figure 3-2 shows an expansion of these processes.

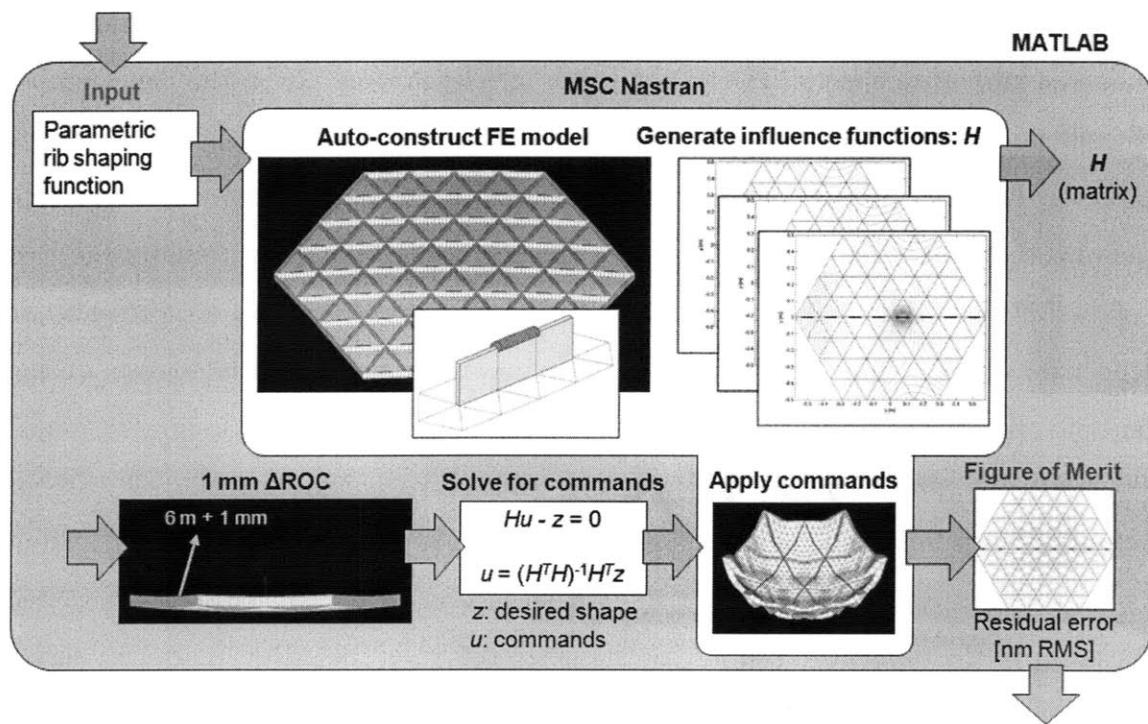


Figure 3-2: Static mirror modeling process using Matlab and MSC Nastran to simulate actuator-induced residual error.

The MOST mirror model is implemented in Matlab, which makes calls to MSC Nastran to auto-construct the FE mirror representation, generate influence functions, and

apply actuator commands. After receiving input parameters from the user, the finite element auto-construction process begins. In Matlab, the model builds a series of data structures that define the grid point locations, element types, element connectivity, material properties, and constraints. These data structures are written to an ASCII Nastran input file.

Following mirror auto-generation, Nastran is called sequentially to generate an influence function for each actuator. Described in detail in Section 3.4.2, an influence function is a collection of mirror surface node displacements for a single actuator command. The influence functions are particular to a given mirror geometry, thus they are re-calculated whenever mirror parameters change. The model assembles the influence functions into a matrix  $H$ , which is used to compute actuator commands given to the entire mirror.

Once influence functions are calculated and assembled, the model commands a radius of curvature change ( $\Delta\text{RoC}$ ) of 1 mm for the mirror. Given the high number of embedded surface-parallel actuators, many other commanded shape changes are possible. For the purposes of this thesis, however, 1 mm  $\Delta\text{RoC}$  serves as a representative actuation maneuver from which performance with respect to actuator-induced residual is evaluated. Several reasons drive the choice of  $\Delta\text{RoC}$  as a representative maneuver. First, changing mirror RoC is common for segmented telescopes during phasing operations [4, 14, 27, 47, 52]. Second,  $\Delta\text{RoC}$  is a low spatial frequency, global change to the mirror shape. The maneuver thus serves as an extreme test case for actuators with localized regions of influence and a high spatial frequency distribution. I.e. it is difficult to achieve smooth surface changes using discretely-located actuators of the type discussed in this thesis. In this way, the  $\Delta\text{RoC}$  maneuver serves as a worst-case example. Finally, changing RoC is a common means for evaluating actuator-induced high spatial frequency error [4, 5].

In order to convert from a desired shape change (1 mm  $\Delta\text{RoC}$ ) to actuator commands, the model uses the previously-computed influence function matrix  $H$ . The mathematical details of this process are discussed in Section 3.4.3. Following command calculation, which occurs within Matlab, the model again calls Nastran to



execute the commands. The result is a statically deformed mirror whose surface node locations are recorded. As introduced in Section 1.2 and detailed in Section 3.5.1, the deformed mirror shape is similar to the dimpled surface of a golf ball due to the discrete location and localized influence of the actuators. The desired mirror shape, on the other hand, is completely smooth. The model takes the node-by-node difference between these two shapes to produce a map of the actuator-induced residual error over the surface of the mirror. This map is returned to the user, along with any other figures of merit.

The following is a summary of the FE mirror modeling process used by this thesis and shown in Figure 3-2:

1. Receive input file with mirror parameters (Matlab)
2. Auto-construct finite element model
  - (a) Assemble grid points, elements, constraints, case control data, etc. (Matlab)
  - (b) Export model data structures to ASCII Nastran input file (Matlab)
3. Calculate influence functions
  - (a) Deform actuator #1 (Nastran)
  - (b) Record mirror surface node displacements (Matlab)
  - (c) Repeat for all actutors, exploring symmetry (Nastran, Matlab)
  - (d) Assemble influence function matrix  $H$  (Matlab)
4. Command 1 mm  $\Delta RoC$ 
  - (a) Calculate actuator commands using influence functions (Matlab)
  - (b) Apply commands to mirror (Nastran)
  - (c) Record displacements (Matlab)
5. Calculate figure(s) of merit and return to user (Matlab)

The sections that follow describe in greater detail the various elements introduced above.

### 3.3 Parameters

The MOST model features many user-adjustable design parameters, a subset of which are used in this thesis. These design parameters automatically define the finite element mirror model generated as a result of the input file. Figure 3-3 shows a sample instantiation of the model.

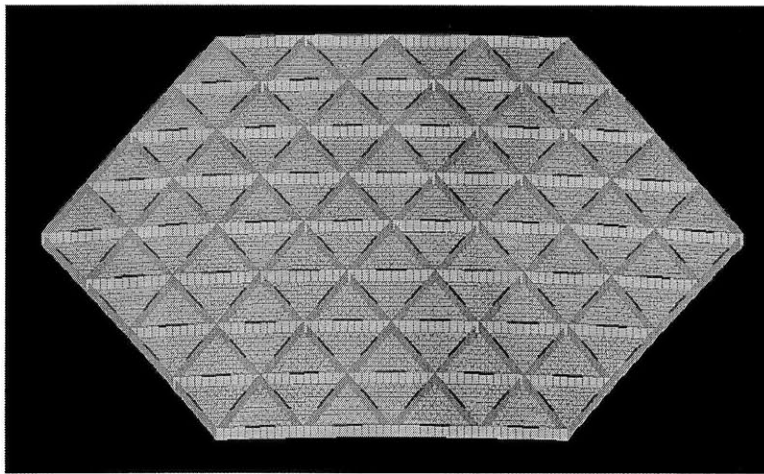


Figure 3-3: Finite element mirror model; actuators are highlighted.

Figure 3-3 shows the back surface of the mirror; the reflecting surface is facing into the page. The ribs are visible, forming a triangular lattice that supports the facesheet. Actuators reside along the edge of the ribs furthest from the facesheet and between rib intersections; they are highlighted in red.

#### 3.3.1 Optical figure

The typical arrangement of a reflecting telescope is shown in Figure 3-4. Reflecting configurations are much more common than refracting designs—particularly in space applications—due to their lower mass for a given aperture size and a lack of chromatic aberration from dispersion in transmissive elements. In general, reflecting telescopes

use a concave primary mirror followed by a convex, flat, or concave secondary mirror.

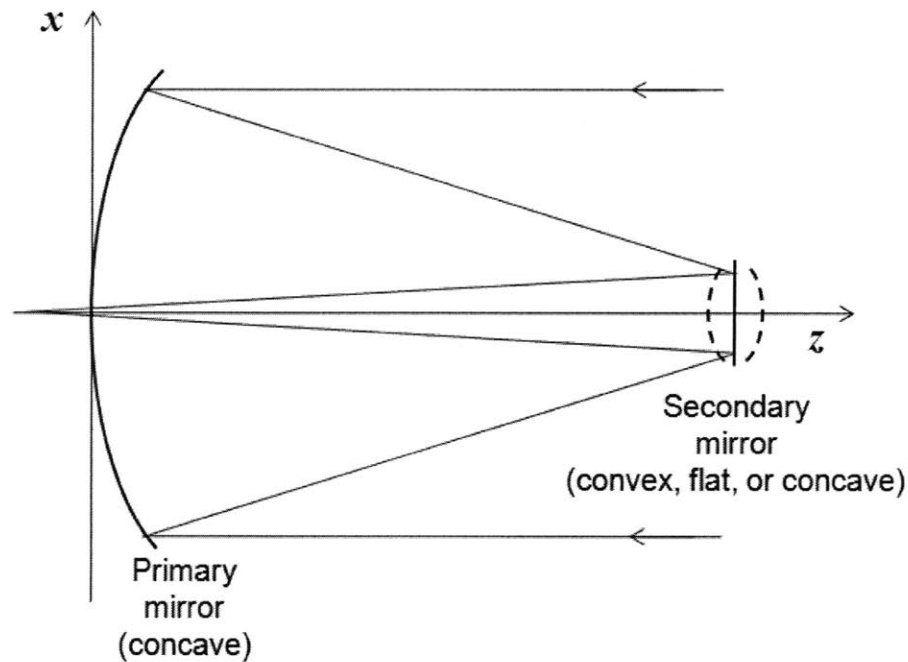


Figure 3-4: Generalized reflecting telescope geometry.

There exists a wide variety of reflecting telescope designs. The geometry of the mirrors determines the optical aberrations that are introduced, and hence the quality and flexibility of the instrument. The simplest designs use a parabolic primary mirror and a flat (Newtonian), concave ellipsoidal (Gregorian), or convex hyperboloid (Cassegrain) secondary mirror. Another variation is the Schmidt Cassegrain, which uses spherical primary and secondary mirrors, plus a toroidal correcting plate to control for spherical aberration. All of these designs focus perfectly on-axis but suffer from coma off-axis, which limits their usable field of view. The Ritchey-Chrétien telescope is a subtype of Cassegrain, however it uses a hyperbolic primary and hyperbolic secondary. The result is negligible amounts of coma and a much larger usable field of view. Many of the most sophisticated instruments (e.g. HST, Spitzer Space Telescope, Keck Telescopes) are Ritchey-Chrétien designs. These telescopes still suffer from astigmatism, however. To alleviate this, recent designs use a tertiary mirror

to correct for astigmatism and further improve image quality over a wide field [39]. Examples of this Three Mirror Anastigmat (TMA) design include JWST and the ground-based Large Synoptic Survey Telescope (LSST). Table 3.1 summarizes these various telescope configurations and mirror geometries. Information on the non-TMA telescopes is from Hecht [36], Born & Wolf [3], and Schroeder [54].

Table 3.1: Summary of reflecting telescope configurations.

Name	Primary	Secondary	Tertiary	Correction
Newtonian	Paraboloid	None/flat	None	Spherical (has coma)
Gregorian	Paraboloid	Ellipsoidal	None	Spherical (has coma)
Classic Cassegrain	Paraboloid	Hyperboloid	None	Spherical (has coma)
Schmidt Cassegrain	Spherical + corrector plate	Spherical	None	Spherical (has coma)
Ritchey-Chrétien	Hyperboloid	Hyperboloid	None	Spherical, coma (has astigmatism)
Three Mirror Anastigmat (TMA)	Ellipsoid*	Hyperboloid*	Ellipsoid*	Spherical, coma, astigmatism

\*One possible arrangement; others exist [39].

The baseline mirror used in this thesis is a single hexagonal on-axis parabolic segment. While only a subset of mirror designs use parabolic primary mirrors, the results and trends are applicable to any concave reflector. In order to facilitate comparison with other optical figures, this work uses radius of curvature (RoC) to quantify the mirror shape. RoC is a convenient measure of the optical prescription because any conic section of revolution can be approximated as spherical in the paraxial region close to the optical axis.

Figure 3-5 shows the relationship between RoC and the focal length  $f$  of a parabolic reflector. This relationship can be expressed mathematically as well; recall that the definition of a parabola is,

$$s(x) = \frac{x^2}{4f}. \quad (3.1)$$

The sphere that best matches the paraboloidal curvature near the optical axis can be defined as,

$$(s + RoC)^2 + x^2 = RoC^2$$

or re-arranging,

$$\begin{aligned} s &= -RoC + \sqrt{RoC^2 - x^2} \\ &= RoC \left[ -1 + \sqrt{1 - \frac{x^2}{RoC^2}} \right] \\ &\approx RoC \left[ -1 + \left( 1 - \frac{x^2}{2RoC} \right) \right] \\ &= -\frac{x^2}{2RoC} \end{aligned} \tag{3.2}$$

where the second to last step is accomplished by Taylor expanding in  $(x/RoC)^2$ . Ignoring the sign difference and instead considering just the distances involved, comparing (3.1) and (3.2) gives,

$$RoC = 2f. \tag{3.3}$$

### 3.3.2 Rib geometry and terminology

Figure 3-6 shows a more detailed view of the geometry of the mirror rib structure. This section briefly discusses the terminology used throughout this thesis to describe various aspects of mirror geometry.

**Rib vertices** are locations where multiple ribs intersect. Six ribs join at each vertex in the interior of the mirror, while the number is less for edges (four) and corners (three). A **rib cell** is the portion of a rib between two rib vertices. A rib cell has two long edges: one that is coincident with the facesheet and an opposite edge that is free. Part of the free edge in each rib cell is occupied by a surface-parallel actuator, whose length can be defined in terms of the fractional rib cell length it takes up. Contrasted with rib cells, **facesheet cells** are the planar triangular regions of facesheet area bounded by three rib cells.

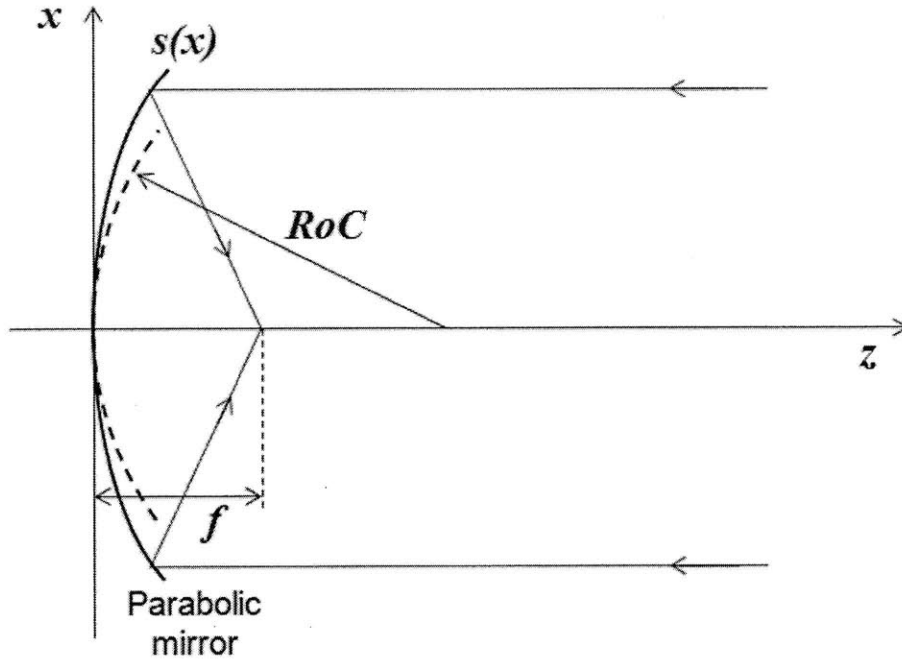


Figure 3-5: Parabolic reflector with focal length  $f$  and spherical approximation.

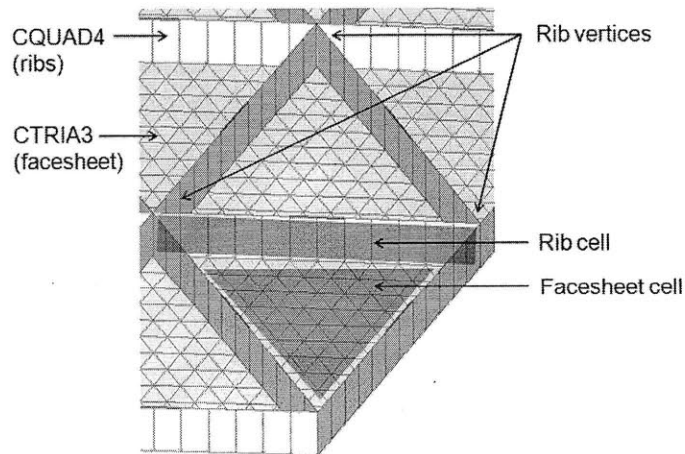


Figure 3-6: Mirror geometry definitions.

An adjustable parameter in the MOST model is the number of *rib rings*. This defines the number of concentric hexagonal rings present in the rib structure. It is assumed that each rib cell contains a single actuator, thus changing the number of rib rings also changes the number of actuators present in the mirror. Figure 3-7 shows three mirrors with differing numbers of rib rings.

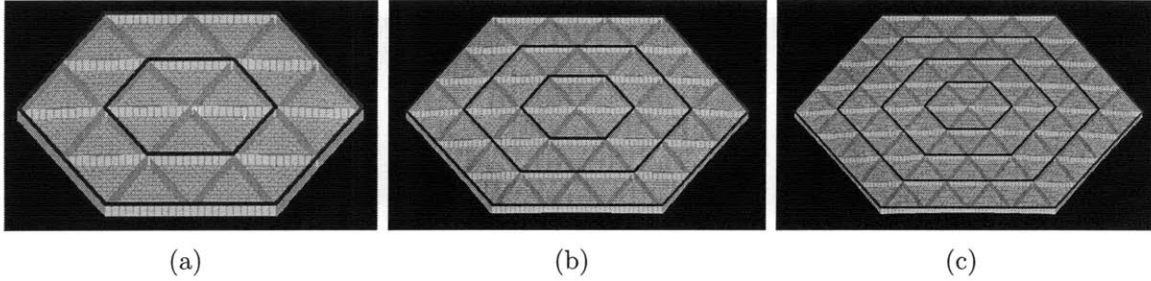


Figure 3-7: Mirror with two (a), three (b), and four (c) rib rings.

### 3.3.3 Substrate

In order to accurately reflect reaction bonded mirrors of the type described in Section 1.1.3, the MOST model assumes that the substrate is cast from homogenous SiC. Table 3.2 gives the properties of this material.

Table 3.2: Material properties of the SiC substrate.

Material property	Symbol	Value
Elastic modulus	$E$	375 GPa
Shear modulus	$G$	26 GPa
Poisson's ratio	$\nu$	0.17
Density	$\rho$	3200 kg/m <sup>3</sup>
Coefficient of thermal expansion (CTE)	$\alpha$	$4.5 \times 10^{-6}$ m/°C

The substrate is implemented using 2D plate elements in MSC Nastran. These elements are well-suited to the thin facesheet and thin, high aspect ratio ribs (see Table 3.3). Furthermore, the use of 2D elements instead of 3D elements reduces computation time, which is essential for rapid trade space exploration. The nature of the mirror geometry dictates which types of elements are used for the different features. The facesheet is constructed from triangular CTRIA3 elements given that the facesheet cells are most readily partitioned into triangles. Likewise, the rectangular geometry of the ribs motivates the use of quadrilateral CQUAD4 elements for those features (see Figure 3-6). The 1D nature of the embedded actuators drives the decision to model them using cylindrical CBAR elements (see Section 3.4.1).

The user is able to specify the rib and facesheet mass fractions, which determine

the percentage of total mass that resides in the ribs and in the facesheet, respectively. It is also possible to include secondary “cathedral” ribs that offer additional structural support to the interior of the facesheet cells. This introduces a cathedral mass fraction, which the user can also specify. Cathedral ribs are not addressed in this thesis, Gray [31] considers them in detail. Finally, it should be noted that the facesheet mass fraction includes only the SiC that resides in the facesheet. An actual mirror would have a thin reflecting layer on top of the bare SiC, however this is assumed to have negligible mass compared to the SiC facesheet material and its contribution to areal density is ignored.

### 3.3.4 Constraints

Rib-stiffened mirrors of the type discussed in this thesis are typically mounted to the optical telescope assembly using a set of kinematic bipod mounts. These mounts can be passive, however for most segmented telescopes the mounts are actively controlled. It is impractical to use the embedded surface-parallel actuators for rigid body motions, due to their limited stroke and localized influence. Therefore actuating rigid body motions is typically the task of active bipod mounts, often during the phasing operation of segmented space telescopes such as JWST [59].

In the FE model used in this work, kinematic bipod mounts are modeled using Nastran single point constraints (SPCs) at three nodes on the back surface of the mirror. This thesis is only concerned with the embedded actuator effects when commanding radius of curvature changes. Therefore because the rigid body motions used in phasing are outside of the scope of this work, the modeled bipod mounts are passive. Taken together, they rigidly fix the mirror in all six degrees of freedom. This is accomplished by constraining each bipod mount (i.e. each SPC) in two degrees of freedom, as shown in Figure 3-8. The SPCs are denoted by circles and are constrained in the direction parallel to the optical axis  $z$  and in the circumferential direction  $\theta$ . Each SPC can translate along the radial direction and can undergo all three rotations. Therefore each kinematic mount can be thought of as a frictionless ball-in-socket joint that is able to translate along a radial frictionless track parallel to the  $r$ - $\theta$  plane and



fixed at a particular  $z$  value.

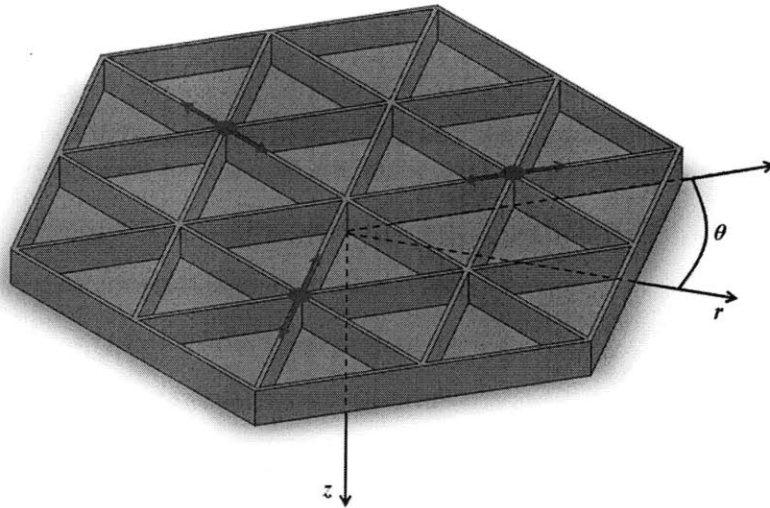


Figure 3-8: Point constraints used to emulate behavior of passive kinematic bipod mirror mounts.

### 3.3.5 Baseline parameters

The following list summarizes the mirror model parameters introduced thus far and used throughout this thesis.

- **Diameter [m]** Diameter of a single hexagonal mirror segment, as measured either from opposite vertices (point-point) or edges (flat-flat).
- **Areal density [kg/m<sup>2</sup>]** Mass of a single mirror segment per unit area.
- **Radius of curvature [m]** Radius of curvature of an on-axis mirror segment as measured at the center.
- **Number of rib rings [#]** Number of concentric hexagonal rings in the mirror rib lattice.
- **Rib cell length [cm]** Length of a rib cell, as measured from one rib vertex to an adjacent vertex.

- **Rib mass fraction** [#] Fraction of total substrate mass that resides in the ribs.
- **Rib height** [mm] Height of the ribs as measured from the back of the facesheet to the rib edge furthest from the facesheet.
- **Rib thickness** [mm] Thickness of the ribs.
- **Facesheet mass fraction** [#] Fraction of the total substrate mass that resides in the facesheet.
- **Facesheet thickness** [mm] Thickness of the facesheet.
- **Number of actuators** [#] Total number of surface-parallel actuators in the mirror segment.
- **Actuator length** [cm] or [fraction of rib cell] Length of an individual surface-parallel actuator, measured in physical units or relative to the rib cell length.
- **FE mesh density** [elements/m] Density of the finite element mesh.

Table 3.3 shows the parameters of the baseline mirror used in this thesis. It is a 1.0 m diameter (flat-flat) substrate with 156 embedded actuators. The areal density of the SiC substrate alone is 8 kg/m<sup>2</sup>. The embedded actuators add 2 kg/m<sup>2</sup>, miscellaneous cabling and electronics add 1 kg/m<sup>2</sup>, and the three kinematic bipod mounts add 1 kg/m<sup>2</sup>, approximately [24]. The total areal density of the baseline mirror segment is therefore approximately 12 kg/m<sup>2</sup>.

While not a parameter of the physical mirror, it is important to note that the density of the FE mesh is 83 elements per meter. This describes the length of each edge of the CTRIA3 triangular facesheet elements, which is also the same as the dimension of the CQUAD4 quadrilateral rib elements parallel to the mirror surface. At 83 elements/m, each CTRIA3 edge is 1.2 cm long. See Section 3.7.1 for additional discussion about mesh density and convergence behavior.

Table 3.3: Baseline mirror parameters.

Parameter	Baseline value
Diameter (flat-flat)	1.0 m
Areal density (SiC substrate only)	8 kg/m <sup>2</sup>
Radius of curvature	6 m
Number of rib rings	4
Rib cell length	14.4 cm
Rib mass fraction	0.27
Rib height	25.4 mm
Rib thickness	1 mm
Facesheet mass fraction	0.73
Facesheet thickness	1.8 mm
Number of actuators	156
Actuator length	7.2 cm
Actuator length (fraction of rib cell)	0.5
Finite element mesh density	83 elements/m

## 3.4 Actuation

Reflecting the design of mirrors in industry, each rib cell contains an embedded surface-parallel actuator that can expand or contract to locally alter the shape of the mirror. Note that because each rib cell contains a single actuator, the number of rib cells—and hence the number of rib rings—uniquely determines the number of actuators in a mirror. As will become evident in Section 4.3, the number of actuators has a significant impact on the amount of actuator quilting for a given  $\Delta\text{RoC}$ .

The remainder of this section describes the details of actuator implementation and commanding in the finite element model. The actuator model is described, including the actuator material properties used and actuation via thermal analogy. The method of influence function calculation is summarized, followed by the mathematics of commanding shape changes via least squares fitting.

### 3.4.1 Actuator model

The actuators used in the mirror segment are co-fired cylindrical electrostrictive devices that undergo a phase transition when exposed to an electric field [43]. The

resulting axial strain causes a bending moment and localized curvature change without the need for a reaction structure. As mentioned in Section 1.1.3, lead-magnesium niobate (PMN) is a common actuator material due to its combination of low CTE, low hysteresis, and high dimensional stability [19].

Electrostrictive materials of this type are characterized by their piezoelectric constant, which describes the bulk strain per unit voltage under free-free boundary conditions. The orientation of the voltage gradient is not necessarily the same as the strain, hence the piezoelectric constant is actually one element of a tensor in three-space. The relevant constant for surface-parallel cylindrical actuators is  $d_{33}$ , which describes axial strain due to an axial voltage gradient. The following is the constitutive equation for axial piezoelectric strains [8]:

$$\epsilon = d_{33} \frac{V}{l} + s_{33}^E T. \quad (3.4)$$

Here  $\epsilon$  is the mechanical strain,  $V$  is the applied voltage,  $l$  is the length of the piezoelectric,  $s_{33}^E$  is the compliance at short circuit, and  $T$  is the vector of material stress. Table 3.4 contains the actuator properties used in this thesis.

Table 3.4: Properties of the electrostrictive actuators.

Property	Symbol	Value
Elastic modulus	$E$	93 GPa
Shear modulus	$G$	10 GPa
Poisson's ratio	$\nu$	0.3
Density	$\rho$	7650 kg/m <sup>3</sup>
Coefficient of thermal expansion (CTE)	$\alpha$	$3.6 \times 10^{-10}$ m/°C
Piezoelectric constant	$d_{33}$	$3.6 \times 10^{-4}$ m/V
Radius	$r$	3 mm
Length	$l$	7.2 mm (baseline)

Note from equation (3.4) that an electrostrictive element in this configuration is neither a pure force nor a pure displacement actuator. Under a voltage load, the actuator will undergo strain and exert a force on the surrounding rib. But as the actuator extends, the rib in which it resides will apply an opposing force that attempts to compress the actuator back, resulting in a stress. Therefore the system

exhibits a combination of stress and strain that precludes modeling via simple forces or displacements.

Nastran does not support piezoelectric elements, so instead the MOST model uses a thermal analogy to model the actuators. Côté et al. [13] showed that there is an exact equivalence between thermal strains and piezoelectric strains. Nastran allows the user to apply temperature loads and can calculate thermal strains. The authors use this capability in MSC Nastran to model a piezoelectric element embedded in a non-active substrate, and go on to validate the approach experimentally. The same technique is used in the mirror model to simulate applied voltages and resulting piezoelectric strains. Note that this approach is valid only in the quasi-static case considered here. See Cohan [8] for an extensive treatment of modeling piezoelectric actuators in the case of a dynamic system.

Figure 3-9 shows the finite element implementation of a single actuator. As stated above, the ribs are modeled using quadrilateral CQUAD4 elements. The actuators are modeled using 1D CBAR elements, which undergo thermal strain to simulate the piezoelectric effect. The CBAR elements are connected to CQUAD4 rib element nodes using RBAR elements with zero thermal conductivity. This is done to thermally isolate the CBAR elements and prevent a thermal gradient from developing in the mirror substrate, which would cause an un-intended deformation. The RBAR elements have zero length, physically joining coincident nodes on the CBAR and CQUAD4 elements without adding a thermal connection.

### 3.4.2 Influence function calculation

The first step in commanding the mirror is to calculate the set of influence functions. The influence function for a given actuator is a map of the mirror surface response when that actuator alone is commanded (see Figure 3-10). Numerically, the influence function for the  $i^{\text{th}}$  actuator is a vector of surface node displacements  $h_i$  returned from Nastran. The 156 influence function vectors are collected into an influence function

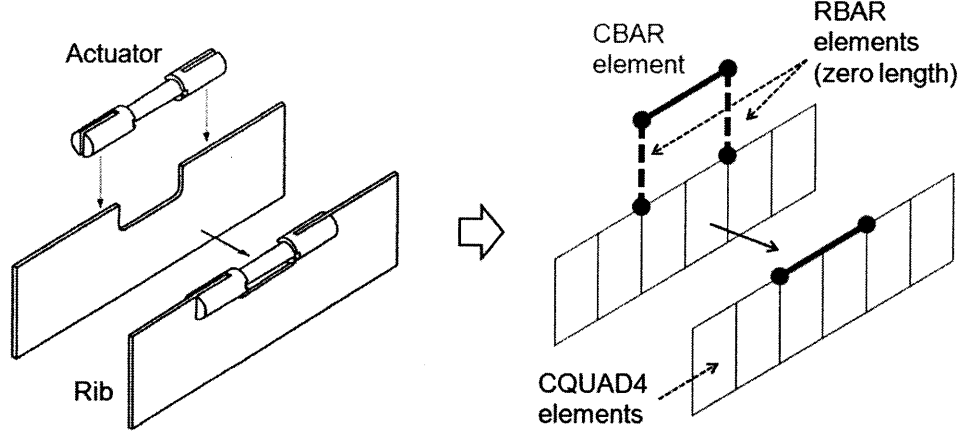


Figure 3-9: Placement of actuator within mirror ribs [21] (left) and the finite element implementation using CBAR elements, zero-length RBAR elements (shown here with non-zero length), and CQUAD4 elements (right).

matrix  $H$ :

$$H = \begin{bmatrix} | & | & & | \\ h_1 & h_2 & \dots & h_{156} \\ | & | & & | \end{bmatrix}. \quad (3.5)$$

The relatively high mesh density of the mirror model means that the surface nodes number in the thousands, therefore  $H$  is not square.

### 3.4.3 Command calculation

The first step in executing a  $\Delta$ RoC maneuver is to generate a set of desired node displacements  $\bar{z}$  in the optical axis direction  $z$ . A parabola of revolution is used to generate this set for the case of a 1 mm  $\Delta$ RoC (see Cohan [8] and Gray [31] for details). Given a set of desired displacements  $\bar{z}$ , the corresponding actuator commands  $\bar{u}$  for achieving those displacements are given by the solution to the following system of equations [37, 66]:

$$H\bar{u} + \bar{z} = \bar{0}. \quad (3.6)$$

Due to the non-square influence function matrix  $H$ , it is necessary to use a least squares approach to solving (3.6). This is accomplished using the Moore-Penrose

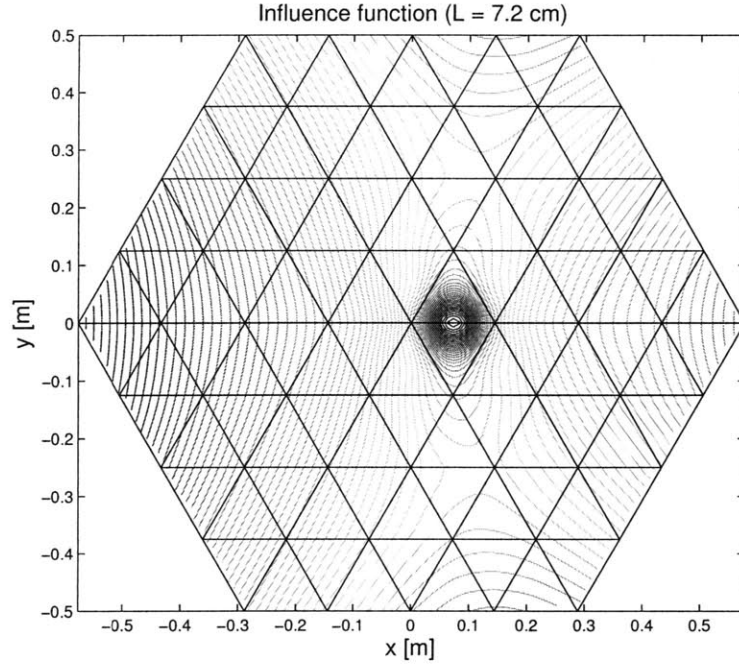


Figure 3-10: Sample influence function.

pseudoinverse  $(A^T A)^{-1} A^T$ . With the node displacements for 1 mm  $\Delta\text{RoC } \bar{z}_{+1 \text{ mm}}$ , the actuator commands are

$$\bar{u}_{+1 \text{ mm}} = - (H^T H)^{-1} H^T \bar{z}_{+1 \text{ mm}}. \quad (3.7)$$

Once calculated, the actuator commands are applied to the mirror and the post-actuation surface displacements are returned by Nastran. These raw displacement outputs are converted by the MOST model into one of several possible figures of merit, discussed in the following section.

### 3.5 Figures of merit

This section presents several figures of merit—both standard in the optical industry and others devised specifically for the MOST project—that describe the performance of actively controlled space telescope mirrors. The mirror model has the flexibility to output numerous user-defined figures of merit when evaluating a given architec-

ture, thus the following represents only the most immediately relevant subset of the available metrics.

### 3.5.1 Actuator-induced high frequency residual error (quilting)

Recall from Section 1.2 that commanding a low-order shape change using discrete surface-parallel actuators results in a golf ball-like “quilting” deformation. This is summarized pictorially in Figure 3-11 for a positive change in mirror radius of curvature ( $\Delta\text{RoC}$ ). For a mirror that is concave up, a positive  $\Delta\text{RoC}$  maneuver ideally results in the surface displacement shown in Figure 3-11a. However, due to the discrete actuator spacing and localized influence functions, the actual surface displacement is the quilted shape shown in Figure 3-11b.

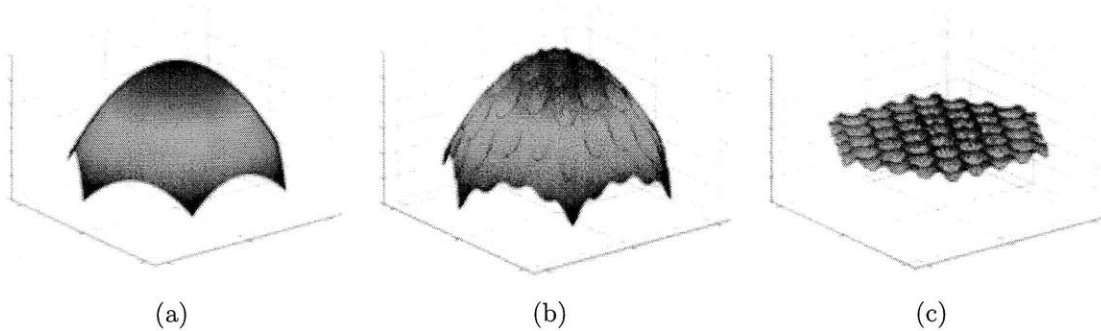


Figure 3-11: (a) Desired surface change for positive  $\Delta\text{RoC}$ , (b) actual surface change for positive  $\Delta\text{RoC}$  with discrete actuators, and (c) actuator-induced residual error (difference of a and b), termed here “actuator quilting”.

The difference between the ideal (desired) and actual surface displacements appears to the optical system as an aberration that degrades image quality (Figure 3-11c). This actuator-induced high frequency residual error is here termed “actuator quilting”, “quilting residual”, or simply “quilting”. In the finite element model, this is calculated by taking a node-by-node difference between the desired and actual displacements. Note that quilting is a representation of mirror *surface* error, as opposed to an optical path length error (which differs by a factor of two; see Section 3.5.2).



Quilting can be expressed either as a position-dependent map of the surface error value, or as the root mean square (RMS) of this map.

The magnitude of the quilting metric is dependent on the magnitude of the commanded  $\Delta\text{RoC}$  maneuver: larger prescription changes result in larger quilting values. Therefore to isolate the effect of changing mirror parameters, this thesis uses a 1 mm  $\Delta\text{RoC}$  maneuver as the standard prescription change used to calculate quilting.

### 3.5.2 Wavefront error (WFE)

In optics, a wavefront is a plane of constant phase that propagates perpendicular to rays. A point source at a finite distance emits spherical wavefronts outward, while a point source at infinity (e.g. a star) emits planar wavefronts. In the case of a space telescope, these planar wavefronts impinge on a curved primary mirror, which converts them into converging spherical wavefronts that meet at a focus where the imaging detector is located.

Any deviation from a perfect optical shape at the primary mirror will cause the wavefronts to become slightly non-spherical after reflection—i.e. they become aberrated. This causes imperfect focusing, resulting in a blurred image. The wavefront error (WFE) is the amount by which a wavefront is advanced or retarded after propagating past an aberration-inducing optical element. WFE can be measured in terms of phase (radians), waves (a non-dimensional number), or distance (e.g. nanometers). Stated another way, WFE is equivalent to the optical path difference (OPD) at a given point in the pupil plane between an ideal reference sphere and the actual aberrated wavefront (see Figure 3-12).

Because the primary mirror of a reflecting telescope acts as the entrance pupil, it is easy to see how quilting residual is directly related to WFE. If the quilting residual map over the mirror surface is given by  $R(x, y)$ , then the WFE at the pupil  $\phi(x, y)$  is simply,

$$\phi(x, y) = 2R(x, y) \quad [\text{nm}] \quad (3.8)$$

or expressed in radians,

$$\phi(x, y) = 2 \left( \frac{2\pi}{\lambda} \right) R(x, y) \quad [\text{rad}] \quad (3.9)$$

where  $\lambda$  is the wavelength of light. Here the factor of two is because of the round-trip distance to and from the primary mirror upon reflection.

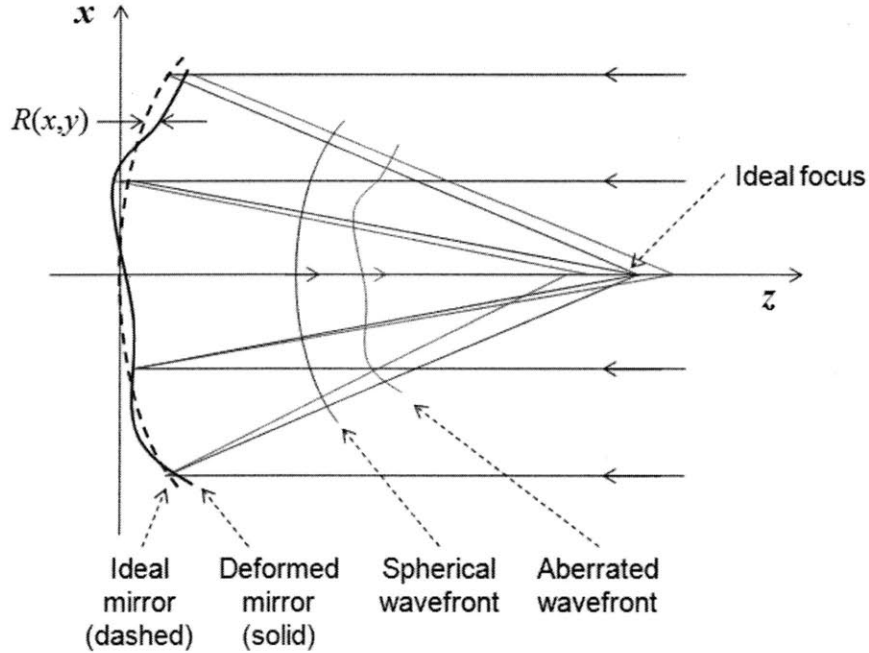


Figure 3-12: Geometry of residual error in a parabolic reflector.

### 3.5.3 Operational flexibility (max $\Delta\text{RoC}$ )

One of the aims of this thesis is to determine the range of prescription changes achievable using surface-parallel actuators. This motivates the creation of an operational flexibility metric—often denoted in this document as max  $\Delta\text{RoC}$ . It is defined as the maximum allowable radius of curvature change possible while keeping the WFE less than or equal to 30 nm RMS. As the amount of  $\Delta\text{RoC}$  is increased, WFE will also increase due to quilting. The max  $\Delta\text{RoC}$  metric establishes an upper bound on radius of curvature change while keeping the residual error below a given threshold. The 30

nm RMS limit corresponds to  $\lambda/20$  for a helium-neon laser at  $\lambda = 632.8$  nm.

Because it is directly related to the amount of residual, max  $\Delta\text{RoC}$  can be computed based on WFE. The MOST model is linear, so it can be assumed that WFE scales linearly with  $\Delta\text{RoC}$ . Therefore,

$$\max \Delta\text{RoC} [\text{mm}] = \frac{1 [\text{mm}]}{\sqrt{\frac{1}{N} \sum_i R(x_i, y_i) [\text{nm RMS}]}} \cdot \frac{30 [\text{nm RMS}]}{2} \quad (3.10)$$

where  $R(x, y)$  is the surface residual error map (i.e. quilting) discretized by  $N$  grid points according to the finite element geometry. The square root is simply the RMS of  $R$  and the 30 nm RMS WFE limit is divided by two because  $R$  is a surface error.

### 3.5.4 Strehl ratio

Finally, Strehl ratio is a very common metric for evaluating optical systems. It is defined as the ratio of the light intensity at the maximum of the point spread function (PSF) of the system with aberrations to that same maximum for the system in the absence of aberrations [30]. Mathematically,

$$S = \frac{\max h_{\text{aberrated}}(x, y)}{\max h_{\text{ideal}}(x, y)} \quad (3.11)$$

where  $h(x, y)$  is the PSF. The idea behind Strehl ratio is that as the image quality degrades due to aberrations, light is spread over a larger PSF. Because the PSF is normalized to have an integral of unity, the larger spread results in a lower maximum value. By dividing by the aberration-free maximum, Strehl ratio compares system performance to the ideal diffraction limited case.

The connection between aberrations at the pupil (i.e. the primary mirror in the case of a reflecting space telescope) and the PSF can be seen through the Fourier transform definition of imaging in wave optics. The broadband PSF is proportional to the squared magnitude of the Fourier transformed complex pupil mask, i.e.

$$h(x', y') \propto |G_{\text{pupil}}(u, v)|^2 \quad (3.12)$$

where

$$G_{\text{pupil}}(u, v) = \mathcal{F}[g_{\text{pupil}}(x, y)]. \quad (3.13)$$

Here  $g_{\text{pupil}}(x, y)$  is the complex pupil function. It can be written generally as,

$$g_{\text{pupil}}(x, y) = A_{\text{pupil}}(x, y) \exp\{i\phi_{\text{pupil}}(x, y)\} \quad (3.14)$$

where  $A_{\text{pupil}}(x, y)$  is a binary amplitude mask defining the physical extent of the entrance pupil and  $\phi_{\text{pupil}}$  is a real-valued phase mask that defines the amount of OPD (in radians) at a given point in the pupil. This phase mask  $\phi$  is precisely where aberrations due to quilting manifest themselves. Indeed,  $\phi$  is given exactly by the WFE equation (3.9). The amplitude and phase pupil masks for the baseline hexagonal segment under 1 mm  $\Delta\text{RoC}$  are shown in Figure 3-13.

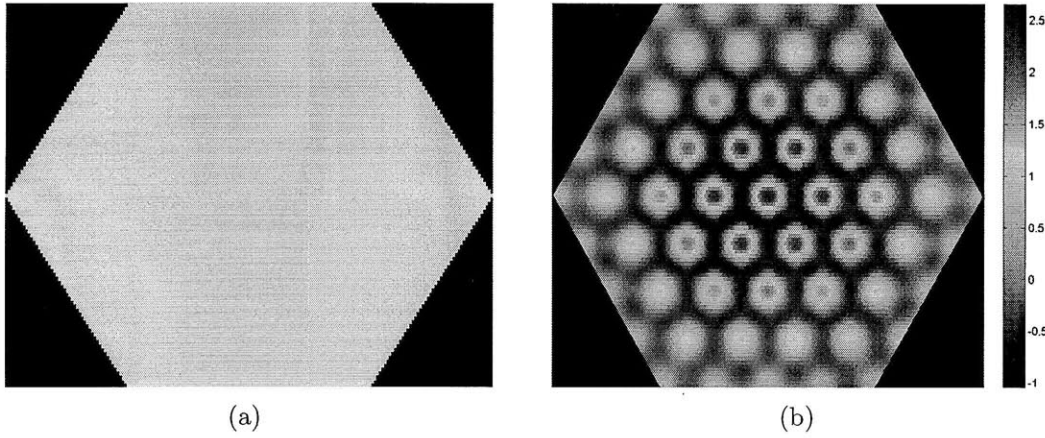


Figure 3-13: (a) Pupil amplitude mask  $A_{\text{pupil}}(x, y)$  and (b) phase mask  $\phi_{\text{pupil}}(x, y)$  [rad] for 1 mm  $\Delta\text{RoC}$ .

Using equation (3.12) and the finite element mirror model, it is possible to generate a PSF for a given radius of curvature change. Figure 3-14 compares the PSFs for a perfect hexagonal segment and a quilted segmented after 1 mm  $\Delta\text{RoC}$ .

With this simulation capability, it is possible to compute Strehl ratio as a function of  $\Delta\text{RoC}$  by substituting the maxima of the aberrated and ideal hexagonal PSFs into (3.11). As expected, the Strehl ratio decreases substantially with increasing  $\Delta\text{RoC}$ . This is due entirely to actuator quilting effects. Plotting Strehl ratio as a function of

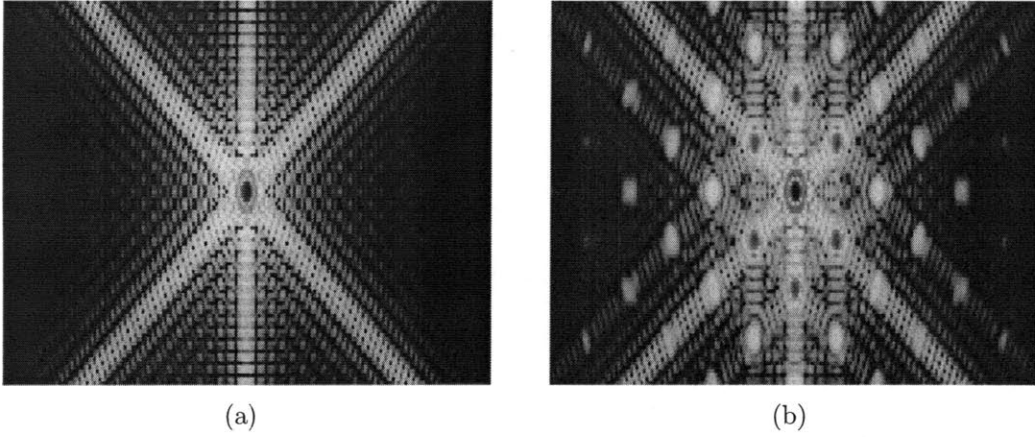


Figure 3-14: Simulated point spread functions for (a) a perfect hexagonal segment and (b) an actively-controlled hexagonal segment after commanding 1 mm  $\Delta\text{RoC}$ .

quilting produces an expected inverse dependence, as shown in Figure 3-15.

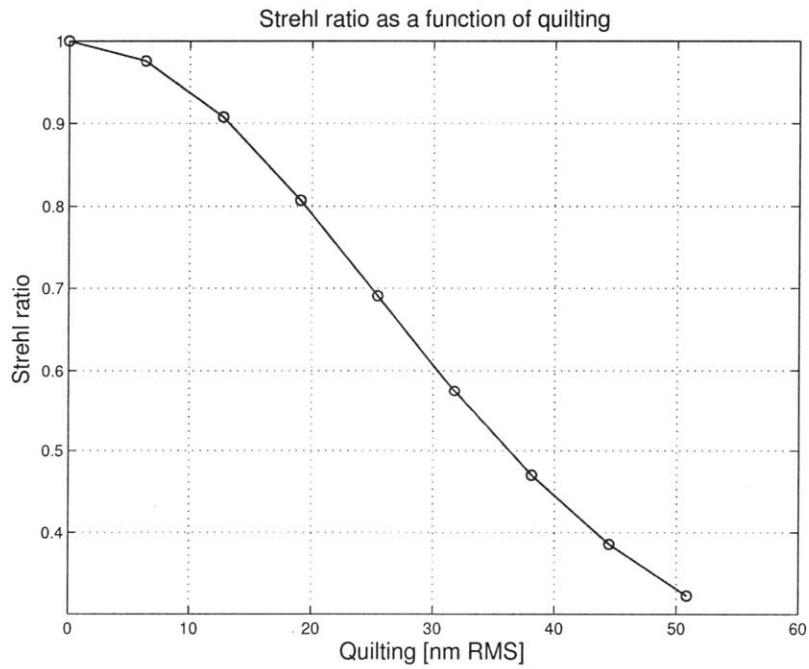


Figure 3-15: Strehl ratio as a function of actuator quilting.

### 3.5.5 Figure of merit summary

This section defined quilting, WFE, operational flexibility (max  $\Delta\text{RoC}$ ), and Strehl ratio as separate but related figures of merit. Because this thesis is primarily concerned with the effect of actuation on high spatial frequency residual errors, actuator quilting (for 1 mm  $\Delta\text{RoC}$ ) is the primary figure of merit. WFE will be referenced occasionally, and the intuitive meaning is largely the same as quilting. An important goal of this work is to bound the range of prescription changes attainable through surface-parallel application, while keeping actuator residual effects below a certain threshold. This is precisely what the operational flexibility (max  $\Delta\text{RoC}$ ) metric is intended to capture, hence this figure of merit is studied in addition to quilting. Indeed, they are closely related through equation (3.10). Finally, Strehl ratio, while an important figure of merit for many optical systems, will not be considered independently in this work. Figure 3-15 depicts the relationship between Strehl ratio and quilting, which is sufficient for determining the Strehl ratio based on the results given in Chapters 4 and 5.

## 3.6 Wavefront sensing

Any active space telescope must have means of sensing the residual WFE introduced by the primary mirror. A closed-loop controller uses this information in an attempt to drive the residual to zero by servoing the mirror actuators. As shown in Section 3.5.2, determining the WFE due to a given reflective optical surface is tantamount to determining the shape of that surface. Several techniques exist to measure optical surface shapes and this section discusses three such approaches that are common in the evaluation of space-based optics: Shack-Hartmann wavefront sensors, interferometry, and iterative phase retrieval.

### 3.6.1 Shack-Hartmann wavefront sensor

Common in many adaptive and active optics systems, Shack-Hartmann wavefront sensors provide information on the slope profile of the incident wavefront. First constructed by Shack by adding a lenslet array to a typical Hartmann screen [57], Shack-Hartmann wavefront sensors have been used for the past three decades in optical systems ranging from ground based large aperture telescopes to retinal imaging in ophthalmology [55]. Figure 3-16 shows a Shack-Hartman wavefront sensor in schematic form.

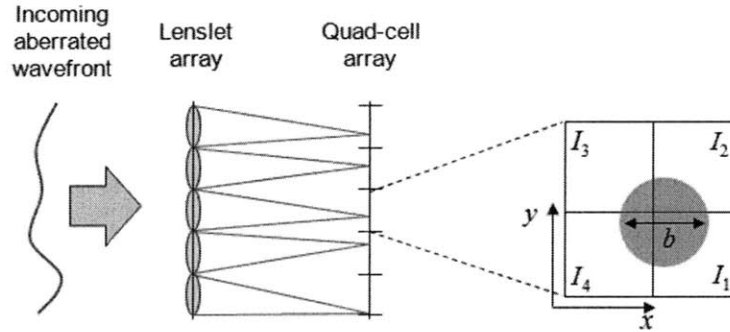


Figure 3-16: Shack-Hartmann wavefront sensor.

The incident wavefront impinges on an array of small lenses (i.e. “lenslets”), each of which focuses the local portion of the wavefront onto a corresponding detector cell made of four photodiodes (“quad-cells”). There is a one-to-one mapping between the lenslet and quad-cell arrays. Slope changes in an incident wavefront correspond to linear shifts at the image plane, making it possible to determine the wavefront slope across the lenslet array by measuring the movement in quad-cell spot locations. The latter is accomplished using the following formulae:

$$\delta_x = \frac{b}{2} \left[ \frac{(I_2 + I_1) - (I_3 + I_4)}{I_1 + I_2 + I_3 + I_4} \right] \quad (3.15)$$

$$\delta_y = \frac{b}{2} \left[ \frac{(I_3 + I_2) - (I_4 + I_1)}{I_1 + I_2 + I_3 + I_4} \right] \quad (3.16)$$

Here  $\delta_x$  and  $\delta_y$  are the horizontal and vertical spot displacements, respectively,  $I_i$

are intensities as measured by the photodiodes, and  $b$  is the spot diameter. Note that (3.15) and (3.16) only apply for small displacements, thus the lenslet array focal length must be tailored according to the expected amount of aberration and desired sensing range.

Once spot centroids are recorded, the local slope of the wavefront  $(\theta_x, \theta_y)$  can be computed as,

$$(\theta_x, \theta_y) = (\delta_x, \delta_y)/f \quad (3.17)$$

where  $f$  is the lenslet focal length. The desired output of the sensing process is knowledge of the aberrated wavefront's shape. At this point, however, only local slopes at each of the lenslet locations are known. These local slopes must be converted into wavefront knowledge over the entire sensed aperture, a process known as wavefront reconstruction. Grocott [34] and Miller [42] describe several wavefront reconstruction approaches.

Shack-Hartmann wavefront sensors offer high sampling rates due to the fast read-out times typical of photodiodes and the high bandwidth of available hardware implementations for reconstruction (e.g. digital signal processors). This capability for high temporal frequency sensing makes Shack-Hartmann wavefront sensors a common component in adaptive optics systems. Closed-loop bandwidths in the kilohertz range are now routine.

### 3.6.2 Interferometry

Another means of determining the surface shape of optical elements is the use of interferometry. This approach is particularly effective when high quality surface data are needed, given that interferometric measurements are precise to a fraction of the evaluating wavelength, which can be made deliberately small. A common arrangement is the Twyman-Green interferometer, shown in Figure 3-17. A variation on the Michelson interferometer, the Twyman-Green instrument uses a quasi-monochromatic point source to illuminate a test lens (or test mirror) using a plane wave.

In the typical arrangement, a laser-fed point source is used along with a collimating



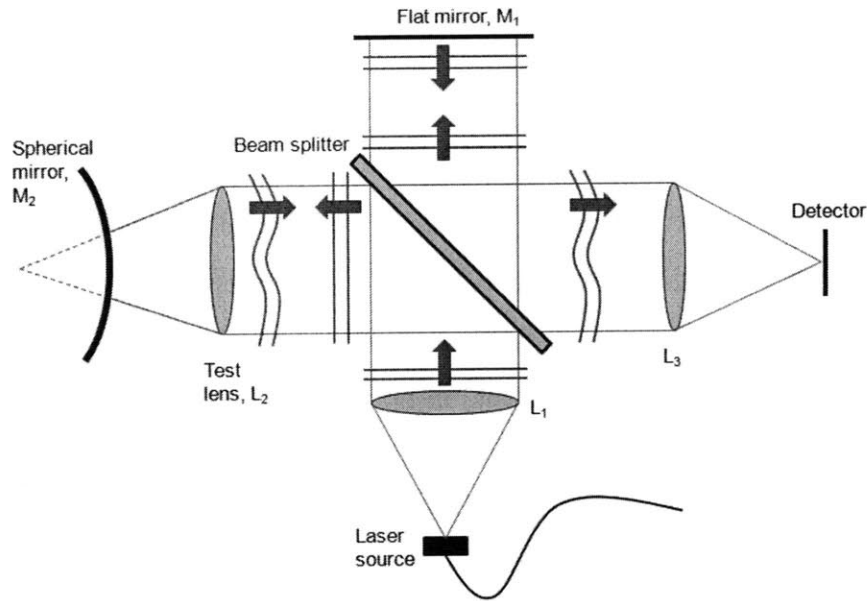


Figure 3-17: Twyman-Green interferometer for testing the wavefront error of a test lens  $L_2$ , adapted from Hecht [36].

lens  $L_1$  to produce plane waves. A beam splitter then divides the beam into a reference arm and the test article arm. A flat mirror  $M_1$  in the reference arm returns the plane wave, while a test lens  $L_2$  and spherical mirror  $M_2$  in the other arm returns an aberrated wavefront from the lens. Note that the two reference mirrors  $M_1$  and  $M_2$  must be very high optical quality. The interfering waves after the beam splitter are then imaged onto a detector using  $L_2$ . The result is a fringe pattern that contains a distinct signature of the aberration introduced by the lens. Modern digital processing techniques can be used to automatically extract the WFE function over the surface of the test element from the fringe image at the detector.

Figure 3-17 shows the arrangement for testing a refractive element, however testing a reflecting element is easily accomplished by simply replacing  $L_2$  and  $M_2$  with a single mirror to be evaluated. Note that when changing the test element, the core Michelson interferometer optical path (i.e. source,  $L_1$ ,  $M_1$ , beam splitter,  $L_3$ , detector) remains the same. The Zygo interferometer is a very common turnkey system that packages this core functionality into a portable unit [28]. External components augment the core unit to form various interferometric evaluation arrangements.

### 3.6.3 Phase retrieval

Another wavefront sensing technique is iterative phase retrieval. This approach is computationally intensive but is increasingly common due to improvements in computer performance. Phase retrieval uses a detector located at the image plane—the science camera in the case of space telescope—to generate a map of phase at the pupil. Such algorithms iteratively Fourier transform between the image plane and pupil plane, enforcing known constraints in both cases. It is common to inject known amounts of defocus (i.e. phase diversity) using a linear translation stage at the image plane. This spreads the relevant phase information over additional pixels in the image plane, enhancing the ability to accurately determine the aberrations that are present. Figure 3-18 from Dean et al. [14] gives a schematic representation of the iterative phase retrieval process.

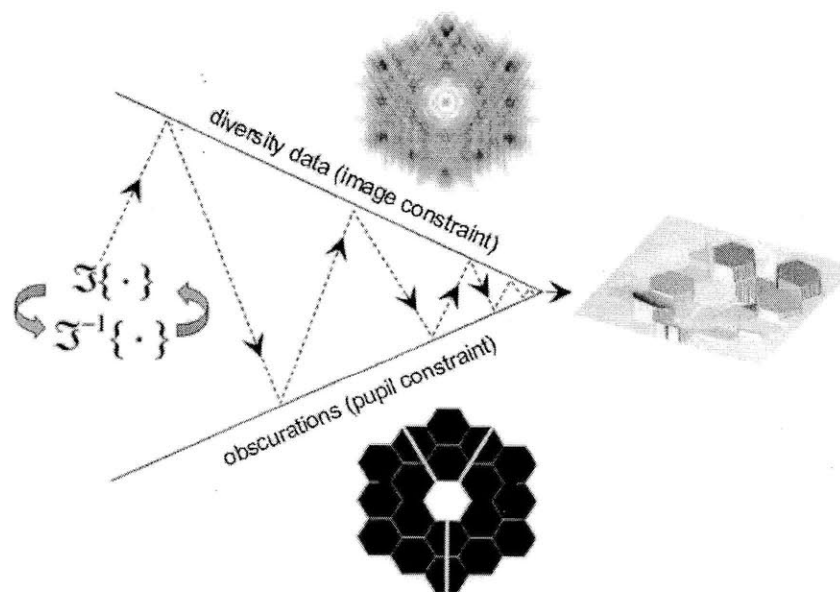


Figure 3-18: Generalized representation of phase retrieval by iteratively transforming between the image and pupil planes while enforcing known constraints; from Dean et al. [14].

The Modified Gerchberg-Saxton (MGS) algorithm is one approach to iterative phase retrieval. It begins with a random guess at the phase at the exit pupil (i.e. the OPD, which is related to the WFE) [52]. The illuminating wavelength and pupil

mask are assumed to be known. The initial guess for the pupil function is combined with the known mask to give a complex array that represents the estimated field at the pupil. This is Fourier transformed to the image plane, providing an estimate of the complex field at the image. The square root of the actual image data is then substituted for the transformed amplitude contribution of the field estimate. This field is propagated back to the pupil plane, where the known aperture mask is substituted for the amplitude contribution of the pupil field estimate. In short, the amplitude portion of the field estimate is continually replaced by known amplitudes at the image and pupil. The phase, however, continues to converge to a single, stationary map over the pupil. Once the phases ceases changing by some pre-defined amount, the algorithm terminates and the pupil (i.e. WFE) function is returned.

MGS has been used to successfully remove non-common path errors in the Palomar adaptive optics system [2]. It also is the basis of an instrument developed at the Jet Propulsion Laboratory (JPL) called the Phase Retrieval Camera (PRC), which provides a Zygo-like functionality for the evaluation of optical elements [47]. MGS was at one time the baseline algorithm for fine phasing of the JWST segmented primary [33], however it was found to be non-ideal for flight due to an additional computationally intensive phase unwrapping step that is necessary for high dynamic range [27]. Thus JWST will use a related iterative approach called the Hybrid Diversity Algorithm (HDA) that uses feedback to continually transfer aberration content into the diversity function, eliminating the need for phase unwrapping [14].

### 3.6.4 Wavefront sensing summary

For the purposes of this thesis, it is assumed that an iterative phase retrieval technique such as MGS or HDA is employed, using the imaging camera to sense mirror surface deformations. This approach is valid because this thesis only considers quasi-static disturbances such as thermal changes. The control bandwidth is low, thus the phase retrieval algorithm's iteration loop would have sufficient time to converge for each measurement. High frequency disturbances such as reaction wheel imbalance can be present as well, resulting in line-of-sight (LOS) jitter. However this can be mitigated

using a fast steering mirror (FSM) and separate Shack-Hartmann or similar wavefront sensor.

One of the main advantages of phase retrieval is that it uses the imaging detector to determine the mirror surface figure. Typical space telescope detectors have pixel counts in the millions, giving a finely sampled observation frame. This fine sampling—intended to produce high quality science measurements—has the additional benefit of producing a finely sampled mirror surface map. Thus in the modeling process described in Section 3.2, whenever knowledge of the surface figure is needed, the mirror surface is sampled at the grid points established by Nastran. For example, when influence functions are recorded (see Section 3.4.2), the displacements of the surface grid points are used. This is reasonable because the number of surface grid points in the finite element model is typically in the thousands—considerably less than the number of pixels in the image detector used for phase retrieval. Recording finite element grid point displacements can be used as a proxy for phase retrieval because doing so under-samples the mirror surface, serving as a conservative wavefront error measurement compared to what actual phase retrieval would give.

In short, phase retrieval is the baseline mirror surface measurement approach assumed in this thesis. Instead of actually running a phase retrieval algorithm, the mirror model simply records surface grid point displacements as a conservative proxy.

## 3.7 Validation

Model validation is an essential exercise whenever software tools such as those described in this thesis are used. The MOST finite element mirror model has undergone several validation steps, both in this work and previously. This section describes a three-part approach used to validate the model: 1) ensuring convergent figure of merit behavior for increasing mesh density, 2) comparing model outputs with empirical data, and 3) comparing individual model features with simpler analytical models.

### 3.7.1 Mesh convergence behavior

A common and essential activity when working with finite element models is to evaluate the behavior of key model outputs under changing mesh densities. Because the mesh is a modeling artifact unrelated to the actual mirror, the mesh should be fine enough to ensure that the mesh density parameter is decoupled from the figure(s) of merit. This was undertaken by Gray [31], who calculated mode frequencies (i.e. stiffness) and quilting as a function of mesh fidelity (i.e. number of elements per m). The results are shown in Figures 3-19 and 3-20. Note that while this work uses both quilting and max  $\Delta\text{RoC}$  as figures of merit, because the latter is calculated using the former, it is sufficient to simply test convergence of the quilting FOM. The convergence study results indicate that mesh densities of approximately 45 elements/m are sufficient to ensure that quilting remains within a 5% error band. Unless stated otherwise, all results in this thesis are from models with a mesh density of 83 elements/m.

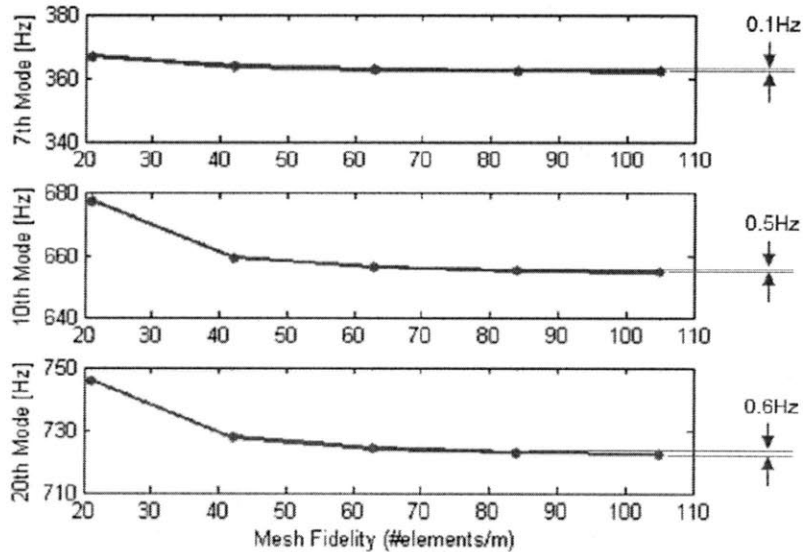


Figure 3-19: Primary mirror mode frequencies as a function of mesh fidelity [31].

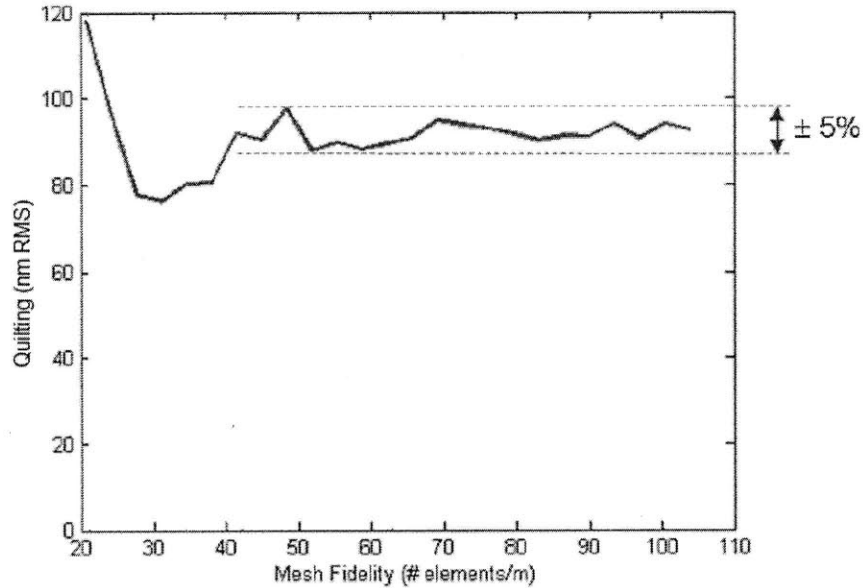


Figure 3-20: Primary mirror quilting (42 actuator case) as a function of mesh fidelity [31].

### 3.7.2 Comparison with empirical data

Sufficient validation requires an additional step beyond convergence analysis: not only must a given behavior of the model converge to a single value for increasing mesh density, but that value must have an acceptable amount of error with respect to empirical data. I.e. it is not enough that a model merely converge—it must converge to the correct value. As such, the MOST model outputs have been compared to the performance of laboratory test beds [8]. The predicted stiffness (fundamental frequency) matched empirical measurements within 2%. Predicted quilting residual for 1 mm  $\Delta$ RoC matched empirical measurements within 7%. These results are summarized in Table 3.5 below.

Table 3.5: Model performance compared to hardware test data.

Model output	Error compared to empirical data
Stiffness (fundamental frequency)	2%
Quilting residual (1 mm $\Delta$ RoC)	7%

### 3.7.3 Comparison with analytical models

The process described above—model convergence followed by empirical confirmation of the converged-to value—is well suited to models for which a robust set of hardware test data exist for the design parameters and figures of merit under consideration. The process is less compatible with models that attempt to incorporate new and untested design features. Indeed, as described briefly in Section 3.1, one of the advantages of modeling is to reduce the need for expensive and time-consuming hardware testing. One can expand the trade space and evaluate the feasibility of innovative designs before investing in fabrication. In such cases, model validation using the above process is difficult because empirical data cannot be immediately extrapolated to the new design.

An alternative is to compare the innovative aspects of the model with simpler analytical models that isolate the uncertain features. These simpler models, derived from first principles and therefore independently verifiable, are used to build confidence in the more complicated model. For example, the MOST mirror model was only compared with test articles that have a single actuator length. However, investigating the effect of changing actuator length is an important aspect of this study. Because hardware data were unavailable, a simple beam model was used to validate the results in which the actuator length was changed. This provides additional confidence that the model is still returning physically accurate results when used in new parts of the trade space. Section 4.2 describes the analytical beam model in detail.

## 3.8 Summary

This chapter outlines the thesis approach, namely the use of a parametric finite element mirror model for iterative design over a larger trade space than would otherwise be possible. The MOST mirror model is discussed in detail, including input parameters, substrate and actuator material properties. The mirror substrate is modeled as a collection of quadrilateral and triangular plate elements, and the actuators are modeled using cylindrical bar elements. Thermal analogy is used to simulate the

piezoelectric properties of the actuators.

A number of sensing architectures is presented, with iterative phase retrieval being the best-suited for the present application. When a map of the mirror surface displacement is required (e.g. when recording influence functions or computing residual error), finite element grid point locations are used as a proxy.

Various figures of merit are discussed, with actuator-induced residual error (quitting) and operational flexibility ( $\max \Delta \text{RoC}$ ) selected as the most relevant to this work. Finally, the chapter presents an approach to model validation that uses confirmation of convergence behavior, agreement with empirical data, and analytical modeling to establish confidence in model predictions.



# Chapter 4

## Actuator geometry

Recalling the research objective of reducing actuator-induced residual error through variations in geometric design parameters, this thesis will consider changes to both actuator and substrate geometry. Actuator geometry variation is the subject of this chapter, while changes in substrate geometry are discussed in Chapter 5. The most natural manner in which to vary actuator geometry is by changing the actuator length. This is explored using two approaches: the MOST mirror model, for which actuator length is a user-defined parameter, and a one-dimensional analytical beam model that provides additional insights. After actuator length, this chapter investigates the effect of actuator number. It is seen that a higher density of actuators over the surface of the mirror results in better performance with respect to actuator quilting. Finally, this chapter investigates the benefits of two-dimensional patch actuators located at the center of facesheet cells.

### 4.1 Actuator length: MOST model

Previous work with the MOST model has shown for a different baseline mirror that increasing actuator length significantly decreases actuator quilting [31, 32]. This section presents additional results for the baseline mirror defined in Table 3.3 and explores the underlying phenomenon in greater detail. These studies assume that the total number of actuators remains constant, thus avoiding increases in control system

complexity or wiring harness mass. There will be a slight mass penalty associated with the additional amount material needed to lengthen the actuators, however even using the longest actuators studied, the individual actuator mass is on the order of tens of grams. With hundreds of actuators in the baseline mirror, the result is still on the order of one kilogram allocated to actuator mass, compared to the approximately ten kilograms allocated to the substrate. Thus the areal density contributions described for the baseline mirror (see Section 3.3.5) are still applicable for the long actuator cases described below.

### 4.1.1 Implementation

Actuator length  $l$  is an adjustable parameter in the MOST mirror model, however because of the discrete nature of the finite element implementation, actuators must span an integer multiple of rib quadrilateral (CQUAD4) elements. This variation is shown for a single actuator in Figure 4-1 and the modeled range of actuator lengths is listed in Table 4.1. The actuator lengths are listed in terms of physical length (cm), the integer number of rib quadrilateral elements the actuator spans, and the fraction of a rib cell the actuator spans. For example, one rib cell is 14.4 cm long in the baseline mirror, thus a 2.4 cm long actuator spans 17% of the available of the space along the rib cell. This will become important below when discussing the underlying effect of actuator length on quilting.

Table 4.1: Range of actuator lengths in units of physical distance, number of rib elements, and fraction of rib cell. Note that for the baseline mirror, the rib cell length is 14.4 cm.

Physical length [cm]	No. of rib elements [#]	Rib cell fraction [-]
2.4	2	0.17
4.8	4	0.33
7.2	6	0.50
9.6	8	0.67
12.0	10	0.83

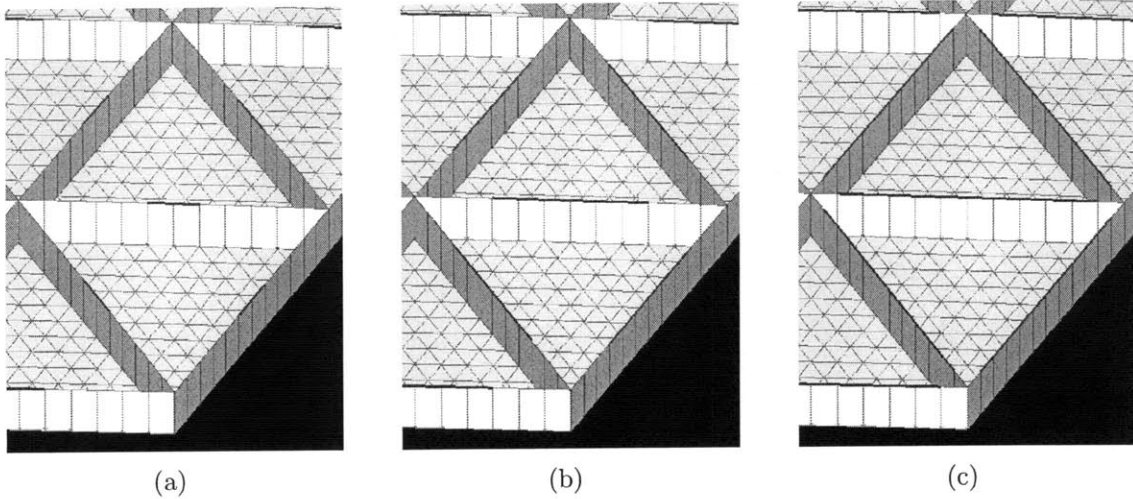


Figure 4-1: Varying actuator length  $l$  in the MOST model: (a)  $l = 2.4$  cm, (b)  $l = 7.2$  cm (the baseline actuator length), and (c)  $l = 12.0$  cm.

#### 4.1.2 Results

Actuator quilting and maximum  $\Delta\text{RoC}$  were computed using the MOST mirror model for the range of actuator lengths shown in Table 4.1. Figures 4-2 and 4-3 show the results for quilting and max  $\Delta\text{RoC}$ , respectively.

As actuator length increases from the baseline value of  $l = 7.2$  cm (0.5 rib cell fraction) to a maximum value of  $l = 12.0$  cm (0.83 rib cell fraction), the quilting goes from 25.4 nm RMS to 7.18 nm RMS—a 72% decrease. The trend is monotonic, therefore decreasing the actuator length from the baseline value will result in increased quilting. Considering the figure of merit for operational flexibility, the model outputs show that moving from the baseline actuator length to the maximum length results in max  $\Delta\text{RoC}$  growing from 0.59 mm to 2.09 mm, a 254% change. Thus increasing actuator length is a very effective means of decreasing quilting and increasing operational flexibility.

The beneficial effect of lengthening the actuators is reflected in the shape of the residual error at the baseline and maximum actuator lengths modeled, shown in Figures 4-4a and b, respectively. The overall reduction in residual is clearly noticeable when moving from the baseline to long actuator case. For ease of comparison, a slice is taken through the two residual plots at  $y = 0$  and the resulting residual traces are

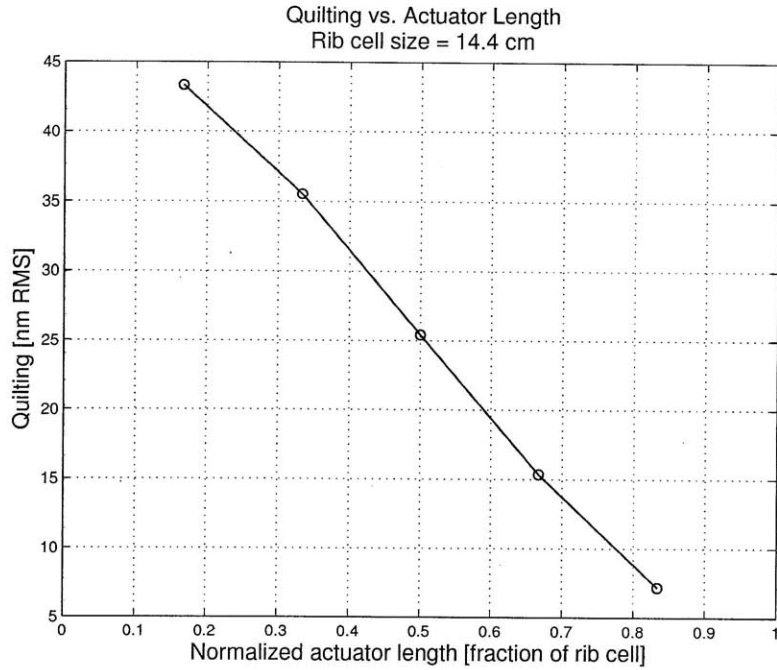


Figure 4-2: Actuator-induced quilting residual as a function of actuator length. Increasing the actuator length decreases the amount of quilting.

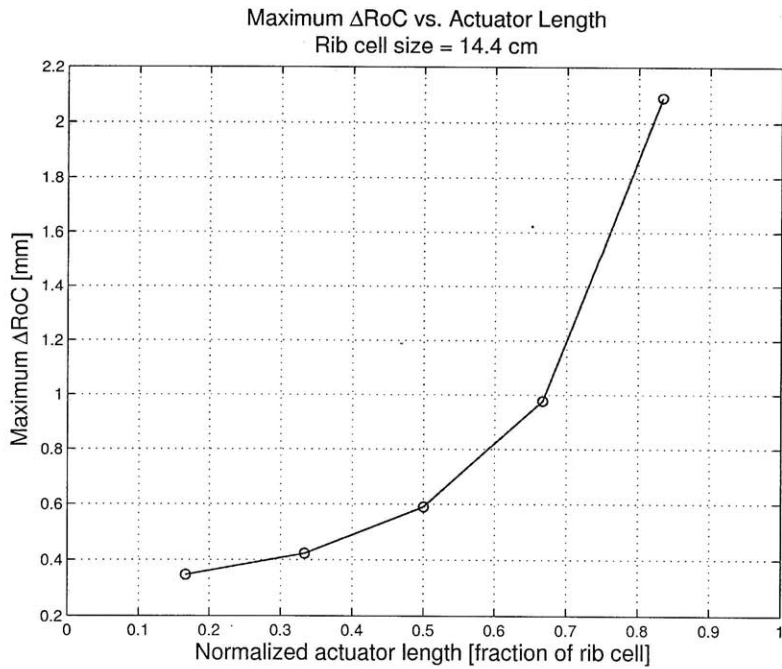


Figure 4-3: Operational flexibility (max  $\Delta\text{RoC}$ ) as a function of actuator length. Increasing the actuator length increases the operational flexibility of the mirror.

overlaid in Figure 4-5—the vertical dashed lines show the rib cell boundaries. There is a clear reduction in the amplitude of the residual when lengthening the actuators.

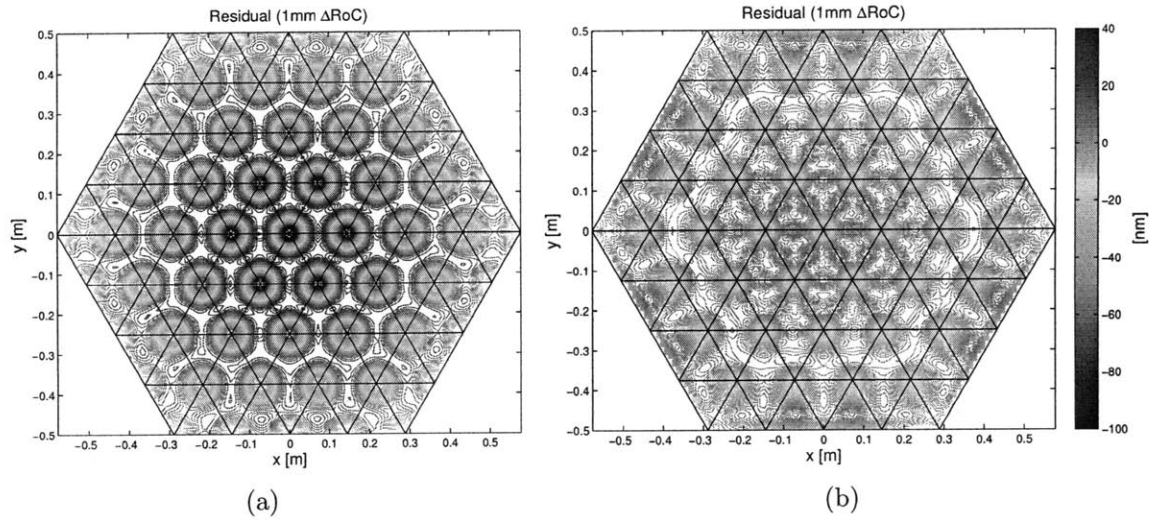


Figure 4-4: Contour plots of actuator-induced residual due to a 1 mm  $\Delta\text{RoC}$  maneuver for actuator lengths of (a) 7.2 cm and (b) 12.0 cm. The contours are in units of nanometers.

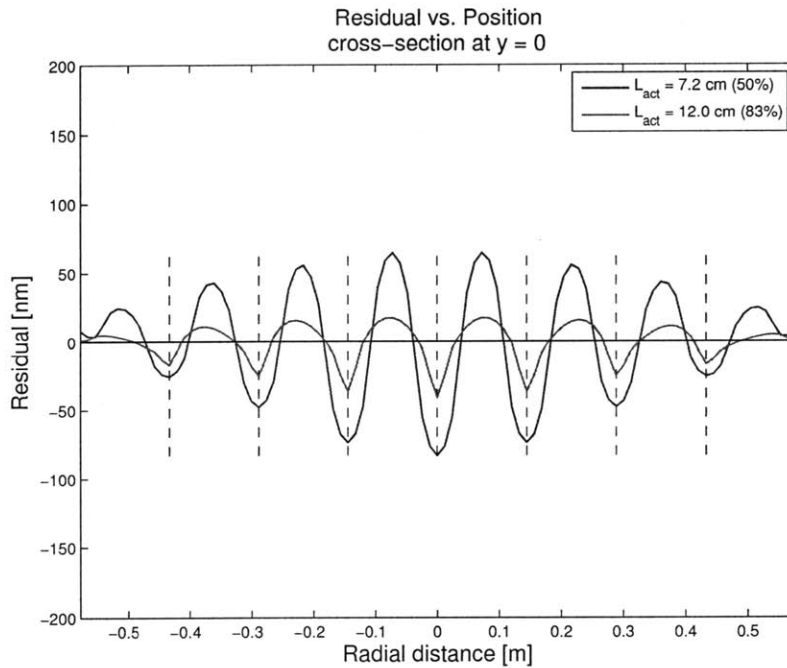


Figure 4-5: Overlaid slices from the residual contour plots, Figures 4-4a and b, at  $y = 0$ . Vertical dashed lines show rib cell boundaries.

### 4.1.3 Role of influence functions

Given the trend of significantly improved performance (i.e. lower quilting, higher operational flexibility) for increasing actuator length, the next step is to identify and analyze the underlying physical phenomenon. Considering the actuator influence functions offers some insights. An influence function for the baseline actuator length is shown in Figure 4-6a. While the actuator does have a discernable global effect on the overall mirror shape, most of the actuator's influence is localized in the facesheet cells above and below the rib in which the actuator resides (see Figure 4-6b). Recall that the discrete nature of the actuators and the resulting highly localized influence functions are the cause of actuator-induced quilting.

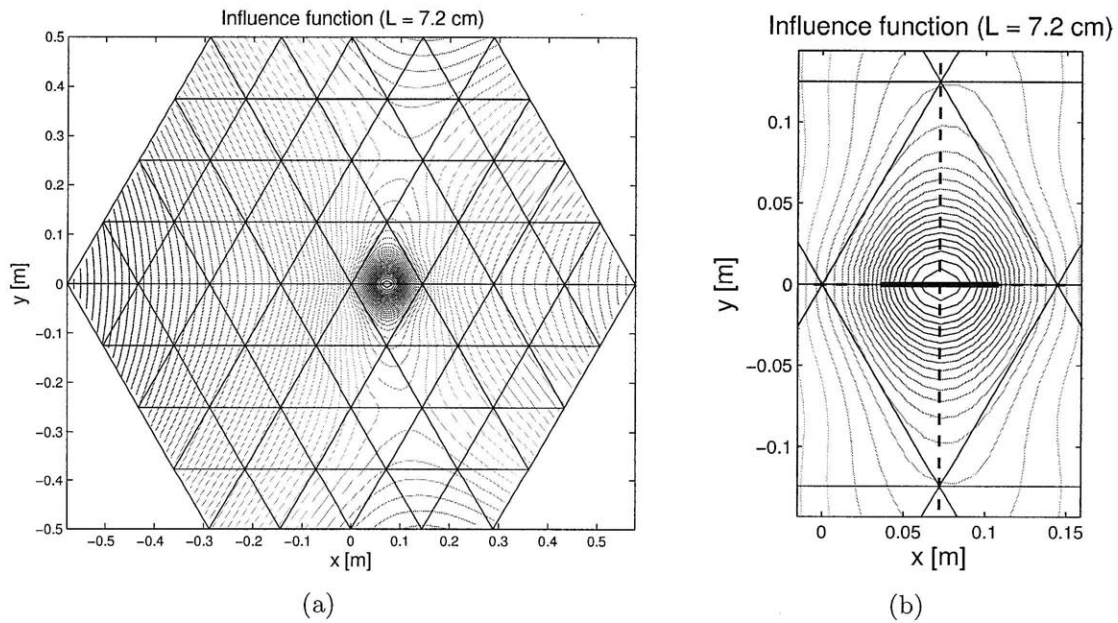


Figure 4-6: (a) Influence function for a single actuator and (b) zooming in on the local region around the actuator, which is shown as a solid black line.

Figure 4-7 shows how the influence function changes when moving from the baseline actuator length (7.2 cm) to the maximum modeled (12.0 cm). This change is difficult to see by comparing influence function contour plots alone, so Figure 4-7 takes horizontal (a) and vertical (b) slices through the contour plot Figure 4-6b along the dashed lines.

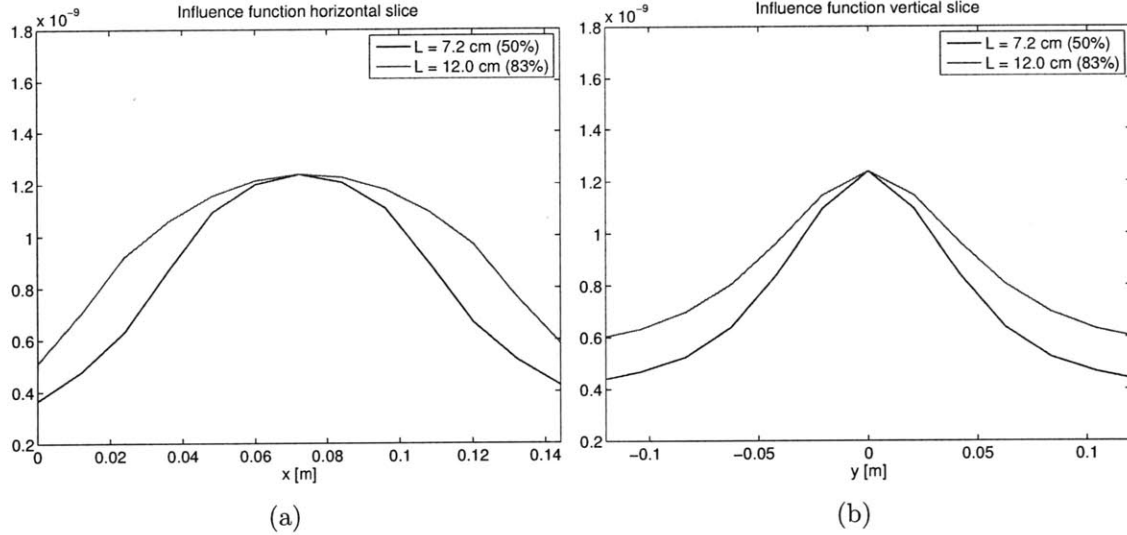


Figure 4-7: Horizontal (a) and vertical (b) slices along the dashed lines shown in Figure 4-6b.

As the actuator is lengthened, the “spread” of the influence function grows. While this is perhaps expected in the along-actuator direction (i.e. the horizontal slice, Figure 4-7a), it is also true for the direction perpendicular to the actuator (i.e. the vertical slice, Figure 4-7b). Lengthening the actuator causes the influence function to grow, making it slightly less highly localized. When these new, wider influence functions are superimposed over the surface of the mirror, the result is improved coverage. The actuators effectively become “less discrete”. This makes it possible to actuate global prescription changes—e.g.  $\Delta\text{RoC}$ —with reduced actuator quilting.

## 4.2 Actuator length: 1D beam model

The above results are generated using the finite element mirror model described in Section 3.2. This section presents an alternative model derived from first principles of physics. Based on the one-dimensional beam equation, this model provides additional insights about the FE results above. Furthermore, the analytical model provides a means of validating the actuator variation portion of the MOST model. As described in Section 3.7.3, comparing MOST model outputs with the predictions of a simpler

analytical model can provide a means of independent validation when hardware data are unavailable.

Figure 4-8 shows a single rib cell and the corresponding beam model. The rib cell and facesheet are abstracted as a single prismatic beam. Likewise, the actuator is modeled as a single moment couple acting at the points where the actuator attaches to the mirror rib. This model treats the piezoelectric as a pure force actuator. Although this does not fully capture the combined force and displacement actuator dynamics (see Section 3.4.1), the results still show good agreement with the finite element model.

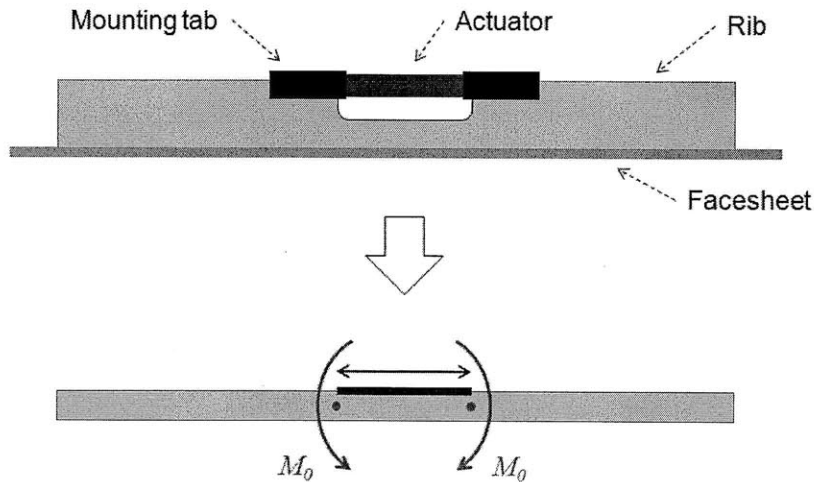


Figure 4-8: Deriving an analytical model from the mirror rib cell and actuator geometry.

This section develops two beam models that differ only by their boundary conditions. The first model uses pinned boundary conditions while the second uses rotational spring boundary conditions that most closely approximate the boundary conditions seen in the mirror itself.

The governing equation for a prismatic member in simple bending is,

$$\frac{1}{\rho} = \frac{M(x)}{EI} \quad (4.1)$$

where  $\rho$  is the radius of curvature,  $M(x)$  is the bending moment,  $E$  is the elastic



modulus, and  $I$  is the moment of inertia of the member's cross section about its neutral axis. From calculus, the curvature  $1/\rho$  of a curve at a point  $(x, y)$  is expressed as,

$$\frac{1}{\rho} = \frac{\frac{d^2y}{dx^2}}{\left[1 + \left(\frac{dy}{dx}\right)^2\right]^{3/2}}. \quad (4.2)$$

For small deflections,  $dy/dx$  is very small, so (4.2) becomes

$$\frac{1}{\rho} = \frac{d^2y}{dx^2}$$

and (4.1) therefore becomes,

$$\frac{d^2y}{dx^2} = \frac{M(x)}{EI}. \quad (4.3)$$

Equation (4.3) is the starting point for the three models that follow. The general approach is to determine the bending moment  $M(x)$  and then integrate twice to arrive at an expression for the beam deflection  $y(x)$ , using boundary conditions to solve for the constants of integration.

### 4.2.1 Pinned boundary conditions

Figure 4-9 below shows the beam model with pinned-pinned boundary conditions. The mounts on either end provide an upward reaction force and zero torque (in order for the zero torque condition to hold, the right support is allowed to freely translate horizontally). While the pinned-pinned boundary conditions are not the most realistic for modeling the mirror facesheet, this model provides initial insights and mathematical development that is useful in later models. The beam (i.e. rib cell) has length  $L$  and the actuator has length  $l$ . The actuator causes a moment couple  $M_0$  while the supports provide a reaction force  $R_0$  at each end of the beam.

The first step in solving equation (4.3) is to define the position-dependent bending moment  $M(x)$ . This is made easier by turning to *singularity functions*, a set of piecewise differentiable curves that are extremely useful for describing and integrating

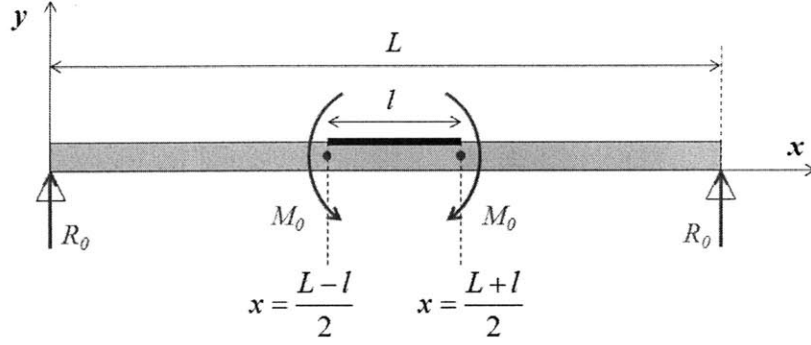


Figure 4-9: Beam model with pinned boundary conditions.

beam loadings. They are defined in Beer et al. [1] according to the following formula:

$$\langle x - a \rangle^n \equiv \begin{cases} (x - a)^n & \text{when } x \geq a \\ 0 & \text{when } x < a. \end{cases} \quad (4.4)$$

Therefore whenever the quantity in the brackets is positive or zero, the brackets are replaced by normal parentheses. Whenever the bracketed quantity is negative, the brackets are replaced by zero. Note that the zeroth order singularity function is simply a step at  $x = a$ :

$$\langle x - a \rangle^0 = \begin{cases} 1 & \text{when } x \geq a \\ 0 & \text{when } x < a. \end{cases} \quad (4.5)$$

Similarly, the first order singularity function is a linear ramp beginning at  $x = a$ , the second order function is a quadratic function, the third order is cubic, and so on. From the definition (4.4) it follows that singularity functions follow the usual rules for integration and differentiation [1]:

$$\int \langle x - a \rangle^n dx = \frac{1}{n+1} \langle x - a \rangle^{n+1} \quad \text{for } n \geq 0 \quad (4.6)$$

and,

$$\frac{d}{dx} \langle x - a \rangle^n dx = n \langle x - a \rangle^{n-1} \quad \text{for } n \geq 1. \quad (4.7)$$

These functions can be used to represent any piecewise polynomial loading, shear,

or bending moment profile. In fact, these profiles are all related by integration and differentiation. Beer et al. [1] show that the load on a beam  $w(x)$  and the resulting shear  $V(x)$  are related by,

$$\frac{dV}{dx} = -w. \quad (4.8)$$

Similarly, the bending moment  $M(x)$  in a beam with shear  $V(x)$  is,

$$\frac{dM}{dx} = V. \quad (4.9)$$

Therefore once either  $M$ ,  $V$ , or  $w$  is expressed in terms of a singularity function, the other quantities can be determined using the moment-shear-loading relationships (4.8) & (4.9) and the integration-differentiation properties (4.6) & (4.7). This is captured in Table 4.2 from Beer et al. [1], which shows basic loading conditions and the corresponding shears and bending moments using singularity functions.

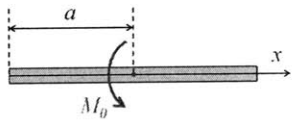
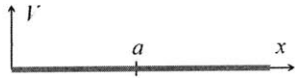
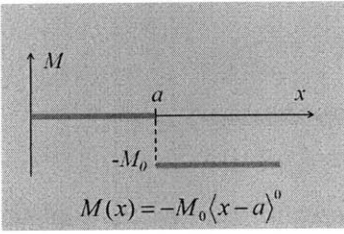
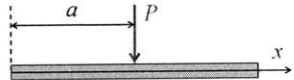
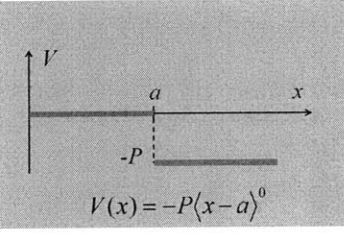
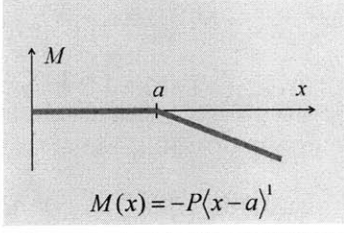
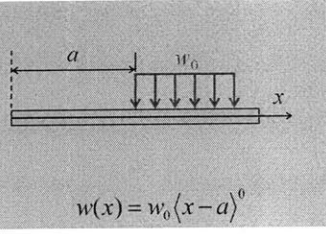
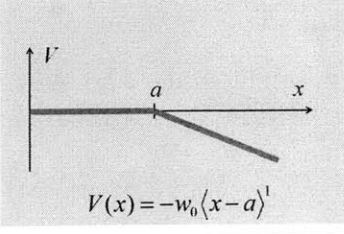
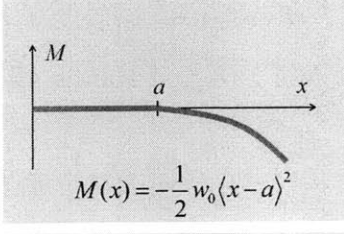
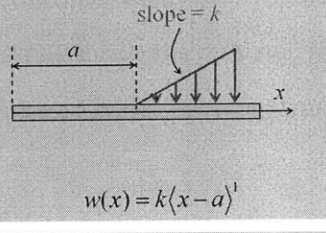
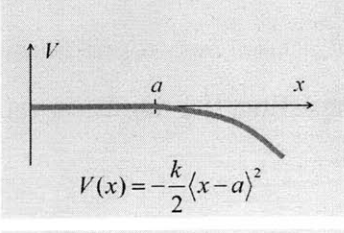
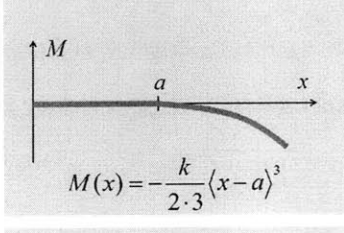
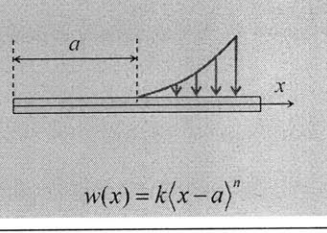
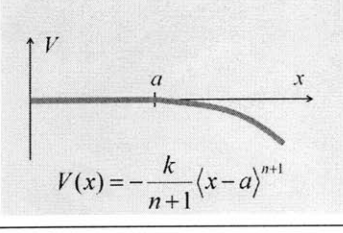
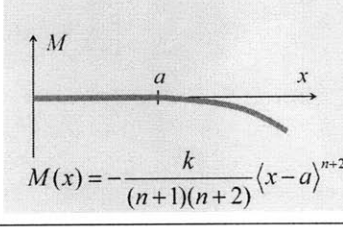
Returning to the beam shown in Figure 4-9, singularity functions can be used to conveniently represent the bending moment  $M(x)$ . Using the first two rows of Table 4.2 to find the bending moment under the shown loading,

$$M(x) = R_0x + R_0\langle x - L \rangle^1 - M_0 \left\langle x - \frac{L-l}{2} \right\rangle^0 + M_0 \left\langle x - \frac{L+l}{2} \right\rangle^0$$

The reaction forces  $R_0$  can be set to zero immediately because there is no vertical loading (including gravity). Inserting the resulting moment equation into the beam deflection ODE (4.3) gives,

$$\frac{d^2y}{dx^2} = -\frac{M_0}{EI} \left\langle x - \frac{L-l}{2} \right\rangle^0 + \frac{M_0}{EI} \left\langle x - \frac{L+l}{2} \right\rangle^0. \quad (4.10)$$

Table 4.2: Basic loadings and corresponding shears and bending moments, expressed using singularity functions; from Beer et al. [1].

Loading	Shear	Bending Moment
		 $M(x) = -M_0 \langle x-a \rangle^0$
	 $V(x) = -P \langle x-a \rangle^0$	 $M(x) = -P \langle x-a \rangle^1$
 $w(x) = w_0 \langle x-a \rangle^0$	 $V(x) = -w_0 \langle x-a \rangle^1$	 $M(x) = -\frac{1}{2} w_0 \langle x-a \rangle^2$
 $w(x) = k \langle x-a \rangle^1$	 $V(x) = -\frac{k}{2} \langle x-a \rangle^2$	 $M(x) = -\frac{k}{2 \cdot 3} \langle x-a \rangle^3$
 $w(x) = k \langle x-a \rangle^n$	 $V(x) = -\frac{k}{n+1} \langle x-a \rangle^{n+1}$	 $M(x) = -\frac{k}{(n+1)(n+2)} \langle x-a \rangle^{n+2}$

The current model assumes that  $E$ ,  $I$ , and  $M_0$  are not functions of  $x$ , so (4.10) can be integrated twice using (4.6),

$$y(x) = -\frac{M_0}{2EI} \left\langle x - \frac{L-l}{2} \right\rangle^2 + \frac{M_0}{2EI} \left\langle x - \frac{L+l}{2} \right\rangle^2 + c_1x + c_2. \quad (4.11)$$

To determine the constants of integration  $c_1$  and  $c_2$ , the boundary conditions  $y(0) = 0$  and  $y(L) = 0$  are used. The condition at the origin forces  $c_2$  to be zero. For the condition at  $x = L$ , (4.11) becomes,

$$\begin{aligned} 0 &= -\frac{M_0}{2EI} \left( L - \frac{L-l}{2} \right)^2 + \frac{M_0}{2EI} \left( L - \frac{L+l}{2} \right)^2 + c_1L \\ &= -\frac{M_0Ll}{2EI} + c_1L \\ \Rightarrow c_1 &= \frac{M_0l}{2EI}. \end{aligned}$$

The resulting equation for beam deflection is then,

$$\boxed{y(x) = -\frac{M_0}{2EI} \left\langle x - \frac{L-l}{2} \right\rangle^2 + \frac{M_0}{2EI} \left\langle x - \frac{L+l}{2} \right\rangle^2 + \frac{M_0l}{2EI}x}. \quad (4.12)$$

Equation (4.12) was used to simulate the deflection of a single rib cell across the same range of actuator lengths used with the finite element model in Section 4.1.2. The quantities  $E$  and  $I$  are set to unity, as is the rib cell length  $L$ . The desired shape is a representative parabolic curve, which the beam model attempts to fit by finding the values of  $M_0$  which minimizes the RMS difference between the beam deflection and the desired curve. This optimization is done using Matlab's built-in `lsqcurvefit` function, which solves nonlinear curve-fitting problems in the least-squares sense.[61]

Figure 4-10a shows the results of this simulation compared with the finite element output (Figure 4-10b). The analytical model shows the appropriate trend, wherein longer actuators better approximate the desired curve shape. One key insight gained upon studying Figure 4-10a and equation (4.12) is the fact that the central portion of the beam deflection, the section from  $x = (L-l)/2$  to  $x = (L+l)/2$ , is parabolic,

while the exterior portion is linear. This parabolic region has length  $l$  and therefore is determined by the length of the actuator. As the distance between the actuator's applied moment couples increases, more of the beam deflection is parabolic, matching the desired parabolic curve more closely. This provides a fitting analogy with the finite element mirror model results in Section 4.1.3. The analytical model confirms that increasing the influence function breadth will reduce the error between the actual and desired displacements.

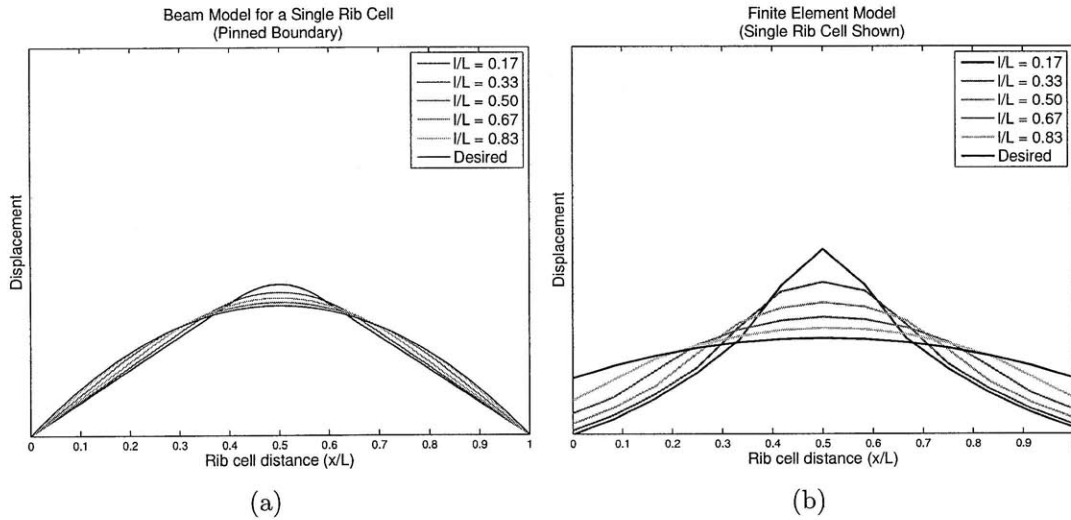


Figure 4-10: Simulated deflection within a single rib cell using (a) the pinned-pinned beam model and (b) the finite element model.

While the two models compare relatively well in the center of the rib cell, there is an obvious mismatch between the boundary conditions. The pinned-pinned analytical model has a downward slope on the edges but the finite element model flattens out. This is due to the fact that neighboring rib cells cause a counter-acting moment that resists changes to the mirror shape. This motivates the need for a new set of boundary conditions for the analytical model, which is the topic of the following section.

## 4.2.2 Rotational spring boundary conditions

Figure 4-11 shows a beam model in which the pure pinned-pinned boundary conditions are augmented by rotational springs with spring constant  $k$ . This provides a higher

fidelity representation of the mirror dynamics. As the beam deflects, the springs will impose a counter-acting reaction torque  $M_t$ , which mimics the restoring force that a rib cell undergoing actuation would feel from the neighboring rib cells. As with the previous beam model, it is assumed that the pins provide zero horizontal force, even when the beam is under deflection.

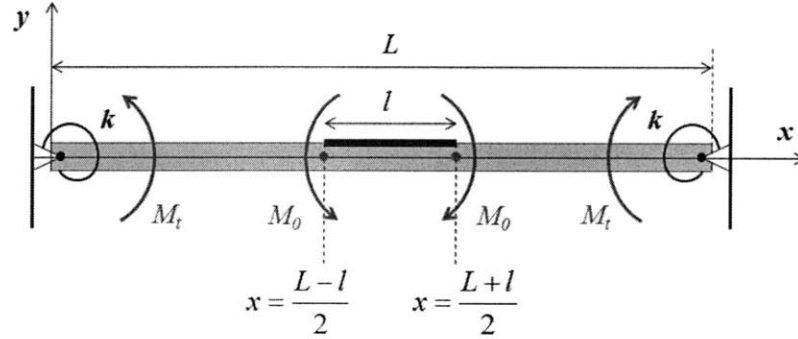


Figure 4-11: Beam model with rotational spring boundary conditions.

As before, the first step in determining the beam deflection is expressing the bending moment, which in this case is:

$$\begin{aligned}
 M(x) &= M_t \langle x - 0 \rangle^0 - M_0 \left\langle x - \frac{L-l}{2} \right\rangle^0 + M_0 \left\langle x - \frac{L+l}{2} \right\rangle^0 - M_t \langle x - L \rangle^0 \\
 \Rightarrow M(x) &= M_t - M_0 \left\langle x - \frac{L-l}{2} \right\rangle^0 + M_0 \left\langle x - \frac{L+l}{2} \right\rangle^0. \tag{4.13}
 \end{aligned}$$

At this point, however, the beam is statically indeterminate and the reaction torque  $M_t$  cannot be determined *a priori*. The goal is to find  $M_t$  as a function of the applied moment  $M_0$  and the spring constant  $k$ . To do this, consider the deflection of a clamped-clamped beam under the equivalent applied moments. Figure 4-12 shows this case (which is also statically indeterminate) as the linear superposition of two statically determinate examples.

Using the same approach as the pinned-pinned case, it is simple to show that the

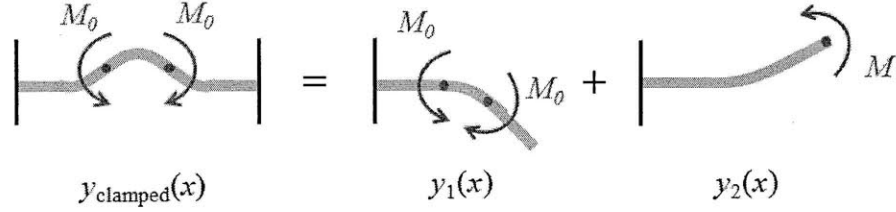


Figure 4-12: Deflection of a clamped-clamped beam as a superposition of two clamped-free deflections.

deflections of the statically determinate examples are,

$$y_1(x) = -\frac{M_0}{2EI} \left\langle x - \frac{L-l}{2} \right\rangle^2 + \frac{M_0}{2EI} \left\langle x + \frac{L-l}{2} \right\rangle^2$$

$$y_2(x) = \frac{M}{2EI} x^2$$

and the resulting overall deflection is therefore,

$$y_{\text{clamped}}(x) = -\frac{M_0}{2EI} \left\langle x - \frac{L-l}{2} \right\rangle^2 + \frac{M_0}{2EI} \left\langle x + \frac{L-l}{2} \right\rangle^2 + \frac{M}{2EI} x^2. \quad (4.14)$$

At this point,  $M$  is unknown and must be determined from boundary conditions. In the clamped-clamped example, the relevant boundary condition is  $y(L) = 0$ . In the spring-spring model of Figure 4-11, the boundary condition is the fact that the angle of the beam end must satisfy the torsional spring equation  $M_t = -k\theta$ . Mathematically,

$$\left. \frac{dy}{dx} \right|_{x=L} = \tan \theta \approx \theta = -\frac{M_t}{k} \quad (4.15)$$

where the tangent approximation is possible because the model only considers small deflections (and therefore small slopes). Enforcing this torsional spring boundary condition on the clamped-clamped deflection makes it possible to solve for the reaction torque  $M_t$  in the spring-spring model. Applying (4.15) to (4.14) gives,

$$\left. \frac{dy}{dx} \right|_{x=L} = -\frac{M_0}{EI} \left\langle L - \frac{L-l}{2} \right\rangle^1 + \frac{M_0}{EI} \left\langle L - \frac{L+l}{2} \right\rangle^1 + \frac{M_t}{EI} L = -\frac{M_t}{k} \quad (4.16)$$



Using the fact that,

$$\left\langle L - \frac{L-l}{2} \right\rangle^1 = \frac{L+l}{2}$$

and

$$\left\langle L - \frac{L+l}{2} \right\rangle^1 = \frac{L-l}{2},$$

equation (4.16) can be written as,

$$\frac{M_t}{k} + \frac{M_t L}{EI} = \frac{M_0}{EI} \left( \frac{L+l}{2} \right) - \frac{M_0}{EI} \left( \frac{L-l}{2} \right).$$

Solving for the reaction torque  $M_t$  gives

$$M_t = \frac{M_0 l}{L + EI/k}. \quad (4.17)$$

Now that  $M_t$  is fully defined, returning to the overall moment equation (4.13) and integrating twice gives the beam deflection for the spring-spring case:

$$y(x) = \frac{M_t}{2EI} x^2 - \frac{M_0}{2EI} \left\langle x - \frac{L-l}{2} \right\rangle^2 + \frac{M_0}{2EI} \left\langle x - \frac{L+l}{2} \right\rangle^2 + c_1 x + c_2. \quad (4.18)$$

Again the constants of integration  $c_1$  and  $c_2$  must be determined by enforcing the boundary conditions  $y(0) = y(L) = 0$ . As before, the boundary condition at the origin means that  $c_2 = 0$ . Applying the condition at  $x = L$  to (4.18),

$$\begin{aligned} 0 &= \frac{M_t}{2EI} L^2 - \frac{M_0}{2EI} \left( L - \frac{L-l}{2} \right)^2 + \frac{M_0}{2EI} \left( L - \frac{L+l}{2} \right)^2 + c_1 L \\ c_1 L &= -\frac{M_t L^2}{2EI} + \frac{M_0 L l}{2EI} \\ \Rightarrow c_1 &= \frac{M_0 l - M_t L}{2EI}. \end{aligned} \quad (4.19)$$

Substituting this result into (4.18), the deflection equation for the spring-spring case

becomes,

$$y(x) = \frac{M_t}{2EI}x^2 - \frac{M_0}{2EI} \left\langle x - \frac{L-l}{2} \right\rangle^2 + \frac{M_0}{2EI} \left\langle x - \frac{L+l}{2} \right\rangle^2 + \frac{M_0l - M_tL}{2EI}x \quad (4.20)$$

where  $M_t = \frac{M_0l}{L + EI/k}$

Note that as  $k \rightarrow 0$ , the expression for the beam deflection goes to the pinned-pinned case (4.12). This makes intuitive sense: as the spring stiffness goes to zero, the restoring torque is eliminated and the support on each end becomes a simple torque-less pin.

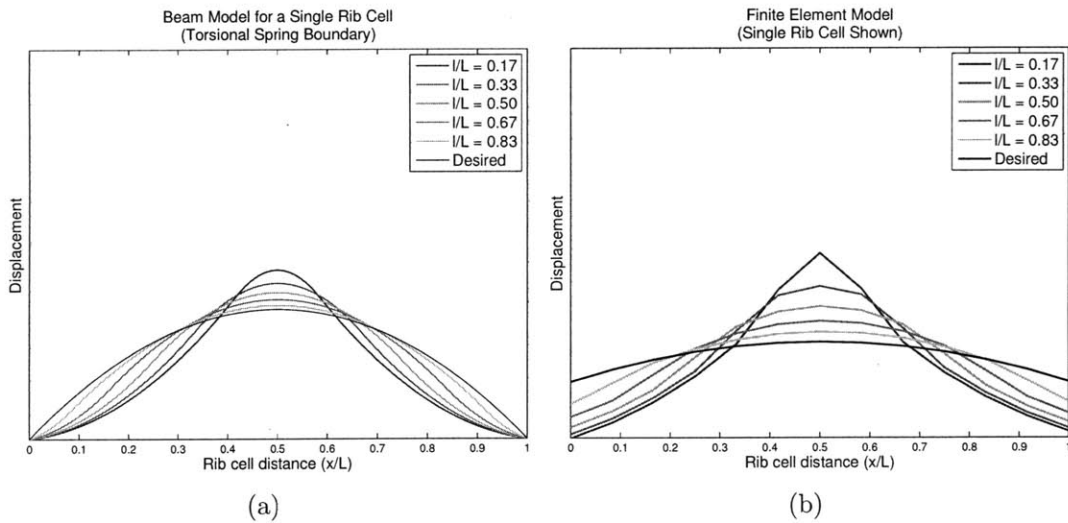


Figure 4-13: Simulated deflection within a single rib cell using (a) the torsional spring beam model and (b) the finite element model.

Figure 4-13a shows the simulated rib cell deflection using (4.20). As before, the physical quantities (including  $k$ ) are set to unity and Matlab's `lsqcurvefit` is used to solve for the actuator commands  $M_0$  that minimize the RMS error between the beam deflection and desired parabola. Like the pinned-pinned model, the torsional spring beam model exhibits the expected behavior, in which the beam deflection approaches the desired shape as the actuator becomes longer. And the agreement between the analytical and finite element simulations is again good in the center of the rib cell, where again the analytical equation is parabolic over the actuator span  $l$ . Comparing

the boundary conditions shows improved agreement over the pinned-pinned model. The torsional springs in the beam model cause a change in concavity moving from the center of the rib cell to the edge. This is also present in the finite element results, indicating that the springs are a reasonable first approach to modeling the reaction forces caused by the neighboring rib cells in the actual mirror.

### 4.3 Number of actuators

Investigations to this point have only considered changes to actuator geometry. The number of actuators has been deliberately kept fixed to avoid increasing system complexity, which would have detrimental effects on mass and other system-level figures of merit. For completeness, however, this section considers the effect of changing the number of actuators. There is a trade-off between actuator length and number of actuators that may be of interest to the designers of such systems.

As discussed in Section 3.4, there is a relationship between the number of concentric rib rings in a mirror and the number of actuators. This is due to the fact that each rib cell contains a single actuator and the number of rib rings uniquely determines the number of rib cells. Table 4.3 shows the number of actuators in a single mirror segment as a function of the number of rib rings.

Table 4.3: Number of actuators for a given number of rib rings.

Rib rings	Actuators
2	42
3	90
4	156
5	240

Thus while actuator length can change smoothly, the number of actuators must take on one of the integer values shown in Table 4.3. The finite element model was used to study quilting and max  $\Delta\text{RoC}$  in mirrors across this range of actuator numbers. This was done in conjunction with changing actuator length. Specifically,

three actuator lengths were modeled for each rib ring setting: ‘short’, ‘medium’, and ‘long’ with respect to the rib cell size. Table 4.4 shows the actuator lengths modeled for each rib ring setting. Note that the fractional actuator lengths cannot be made exactly equal for each number of rib rings because the rib cell size changes.

Table 4.4: Range of actuator lengths used when changing the number of actuators in a single mirror.

Number of rib rings	Number of actuators	Fractional actuator length ( $l/L$ )	Physical actuator length [cm]
2	42	0.11 (short)	3.2
		0.55 (medium)	16.0
		0.89 (long)	25.6
3	90	0.17 (short)	3.2
		0.50 (medium)	9.6
		0.83 (long)	16.0
4	156	0.17 (short)	2.4
		0.50 (medium)	7.2
		0.83 (long)	12.0
5	240	0.16 (short)	1.9
		0.49 (medium)	5.8
		0.82 (long)	9.6

Figures 4-14 and 4-15 show quilting and max  $\Delta\text{RoC}$ , respectively, as a function of absolute actuator length for varying numbers of rib rings (and actuators). The previously-noted trend of reduced quilting and increased max  $\Delta\text{RoC}$  for longer actuators is still present. In addition, increasing the number of actuators significantly improves performance. This is due to the fact that with more actuators, the influence function coverage on the mirror is higher, even for relatively short actuators. As a result, quilting is reduced when commanding global prescription changes like  $\Delta\text{RoC}$ . These results show that designs can trade between actuator length and number of actuators. Manufacturing constraints or cost may guide a mirror architecture toward one or the other.

While increasing the number of actuators in a mirror segment is beneficial, there are drawbacks. Primarily, the complexity of the mirror control system increases when actuators are added. While not studied in detail here, this has a cascading

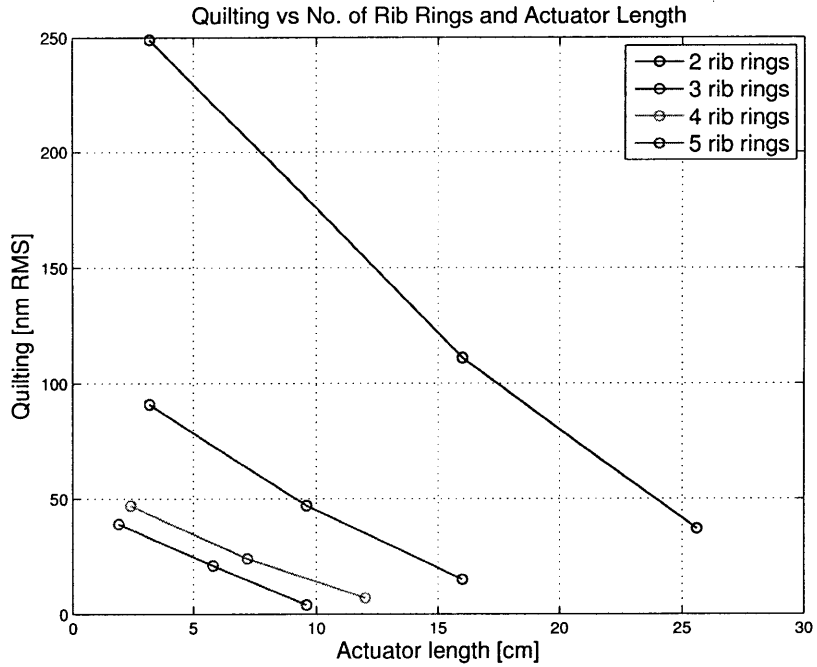


Figure 4-14: Actuator-induced quilting residual as a function of number of rib rings (actuators) and actuator length.

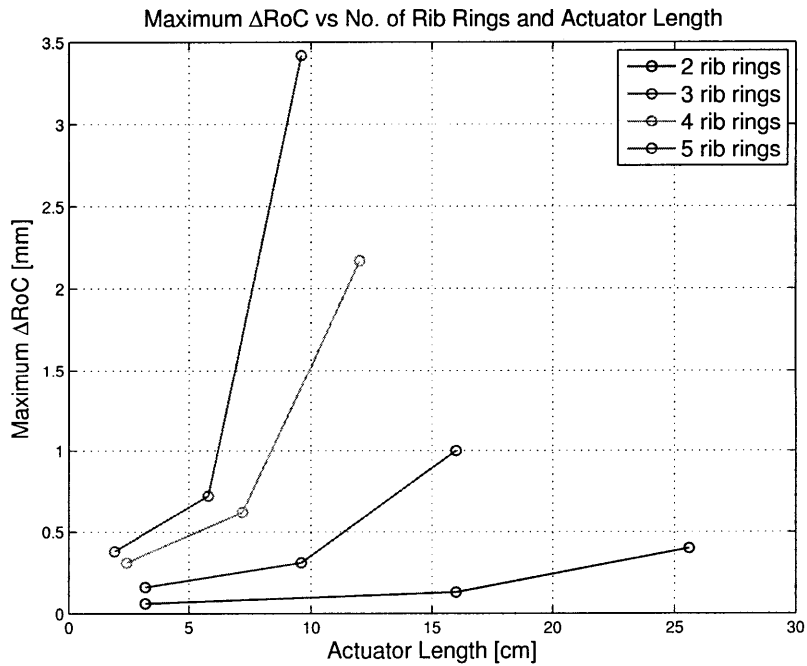


Figure 4-15: Operational flexibility (max  $\Delta RoC$ ) as a function of number of rib rings (actuators) and actuator length.

effect on overall system mass. New piezoelectric control channels require additional wiring and high voltage drive circuitry, and the latter places additional demands on the spacecraft power subsystem. Furthermore, there is additional complexity in the control algorithm, which requires a more capable flight computer with potentially higher power requirements. The net result is an increase in system mass much greater than simply the mass of additional actuators.

## 4.4 Patch actuators

To this point it has been assumed that all of the embedded actuators use the surface-parallel geometry defined in Section 3.4.1. This causes the influence functions to be centered on the mirror ribs (see Figure 3-10). When summed to perform the representative  $\Delta$ RoC maneuver, the combination of rib-based influence functions result in an actuator-induced residual pattern that is likewise aligned with the rib pattern. For example, in Figure 4-4 the quilting pattern is overlaid on the rib lines. The facesheet cells, where there are no ribs, are only weakly influenced by the actuators. Surface-parallel actuators embedded in the ribs are ill-suited to influencing the mirror shape in the open facesheet cells.

This points to a need for another set of influence functions—one that is aligned with the facesheet cells instead of the ribs. Actuators embedded in the center of the facesheet cells would create such an influence function pattern. Furthermore, facesheet actuators could be used to correct for manufacturing-induced print-through residual, which Gray [31] discusses in detail. Print-through occurs due to variations in wear rate during mirror polishing. The variations are caused by decreased reaction pressure within the facesheet cells, resulting in a high frequency residual pattern aligned those triangular regions.

Due to a lack of ribs within the facesheet cells, rod shaped actuators are a poor choice for generating the desired set of influence functions. Instead, 2D “patch” actuators are the more natural solution. These would be bonded to the facesheet opposite the reflecting surface and would serve as a means of changing the mirror shape in re-

gions the rib actuators cannot reach. As described in Section 3.4.1, the rib actuators exploit the  $d_{33}$  electrostrictive effect of certain piezoceramic materials, wherein a voltage gradient across the axial dimension of an actuator causes a corresponding axial strain. The proposed patch actuators could utilize a similar electrostrictive material, but instead exploit the  $d_{31}$  effect wherein a voltage gradient normal to the patch surface causes an in-plane strain. Dürr et al. [16] and Shepherd et al. [58] provide two relevant examples of this approach.

The finite element mirror model was used to evaluate the ability of a patch actuator to create the intended influence function between ribs. Figure 4-16 shows an example of the implementation in Nastran. The actuator is constructed from a group of triangular CTRIA3 elements overlaid on the triangular facesheet elements. Both the actuator and facesheet use CTRIA3 elements of the same size, so the nodes are coincident. As with the cylindrical actuators, the coincident nodes are linked with zero length RBAR elements to thermally isolate the patch actuator from the mirror substrate (see Section 3.4.1).

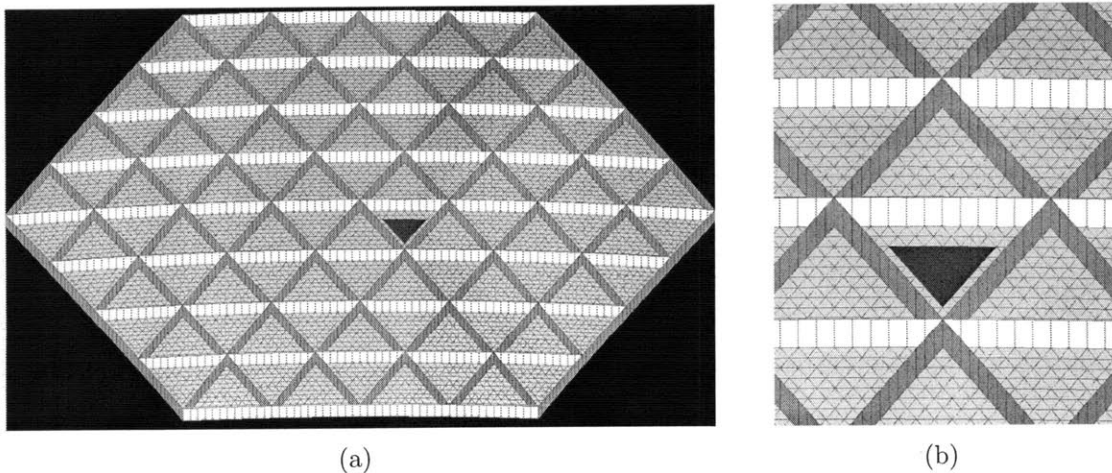


Figure 4-16: (a) Patch actuator implemented using 2D triangular plate elements and (b) detailed view of the patch actuator.

The piezo strain of the patch actuator is simulated using thermal analogy and Nastran's built-in CTE modeling capability, as was the case with the cylindrical actuators (Section 3.4.1). Figure 4-17 shows the influence function associated with the

single actuator depicted in Figure 4-16. The surface deformation is highly localized within the triangular inter-rib facesheet.

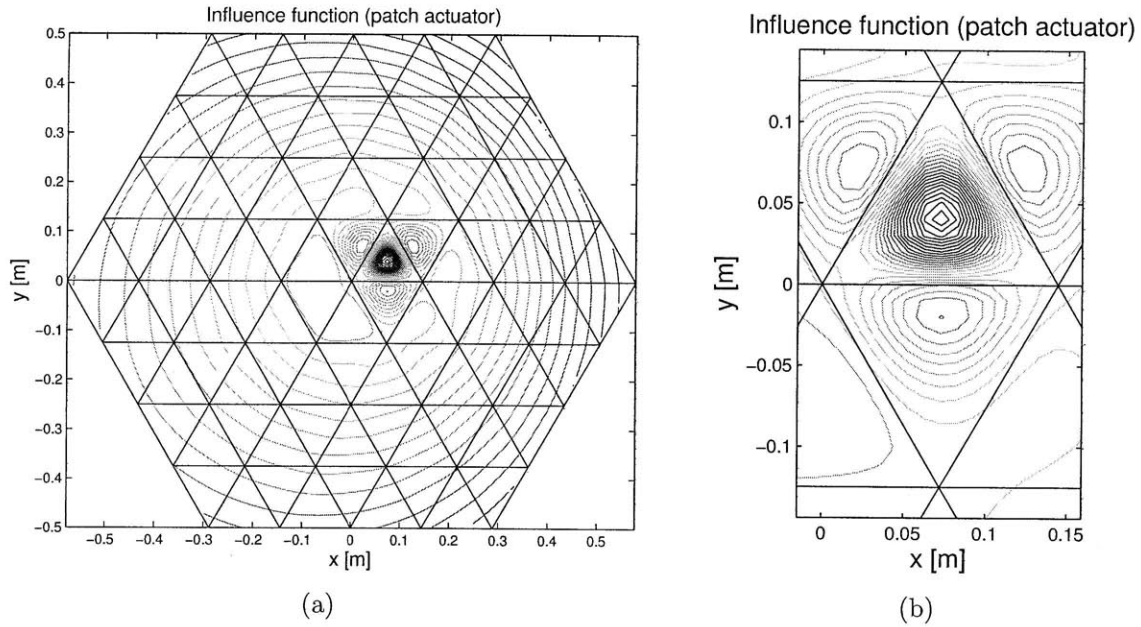


Figure 4-17: (a) Influence function of a patch actuator and (b) magnified view of the influence function.

In an actual implementation, the entire back side of the mirror facesheet would be covered with patch actuators to augment the cylindrical actuators distributed among the ribs. The resulting influence functions would be inserted into the matrix  $H$  in equation (3.6), improving coverage over the mirror surface significantly. This would result in a corresponding decrease in quilting and improvement in operational flexibility. However, this addition of actuators (roughly by a factor of two) would increase system complexity. New requirements would be levied on the avionics that compute the commands (3.7) and the power needed to drive the actuators would increase. These new requirements would flow up into the mass and power budgets of the spacecraft bus, possibly increasing overall mission cost. Therefore, while the influence function result is promising in terms of surface quilting, the performance benefits of embedding patch actuators would need to be carefully traded against the system-wide drawbacks.



## 4.5 Summary

This chapter is devoted to the study of creative actuator geometry as a means of decreasing actuator-induced error. The goal is to reduce quilting without increasing areal density or, if possible, the number of actuators.

The effect of actuator length is studied first, initially using the finite element mirror model, which has actuator length as one of its parameters. Quilting and max  $\Delta\text{RoC}$  are computed for a range of actuator lengths, and the results show that longer actuators offer significant performance advantages. When comparing the baseline actuator length (7.2 cm) to the longest modeled (12.0 cm), there is a 72% decrease in quilting and a factor of 2.5 increase in max  $\Delta\text{RoC}$ . The actuator influence functions are found to play a significant role, with longer actuators producing broader influence functions. This effective reduction in actuator “discrete-ness” aids in the creation smoother global shape changes.

These finite element results are compared with those from two analytical beam models. A rib cell is abstracted as a 1D prismatic beam under pure bending. This model is derived for both pinned-pinned and torsional spring boundary conditions, and the results are shown to roughly capture the behavior of the finite element simulations. Importantly, the beam models illustrate that the effective distance between applied actuator moments drives influence function size.

The effect of actuator number is studied briefly, with more actuators resulting in decreased quilting. Drawbacks to this approach are noted, however, including increased system complexity and power consumption.

Finally, this chapter introduces 2D patch actuators as a potential source of additional control authority. Bonded to the facesheet cells, such actuators create a new, complementary set of influence functions to augment those created by the rib actuators. A sample finite element implementation demonstrates a highly localized influence function suitable for the removal of rib actuator-induced quilting, or manufacturing print-through. However, as with adding more rib actuators, the addition of patch actuators increases power and possibly computation requirements.



# Chapter 5

## Substrate geometry

Variations in actuator geometry were found in Chapter 4 to decrease actuator-induced residual (quilting) and increase operational flexibility (max  $\Delta\text{RoC}$ ). This chapter explores ways of doing the same using variations in substrate geometry. The motivation for exploring substrate geometry is two-fold. First, Budinoff & Michels [4] found that judicious alterations in substrate geometry yielded significant reductions in actuator-induced residual in the SPOT mirror segment. Second, while increasing the space between actuator attachment points was found in the previous chapter to be highly effective, this may not always be feasible. Manufacturing constraints may limit actuator length to only a small fraction of the rib cell. Adding extension tabs is a potential solution, however stroke limitations will persist for short actuators. Therefore altering the substrate geometry, rather than the actuator geometry, may be an alternative worth pursuing.

In the case of the SPOT mirror segment, Budinoff & Michels selected a set of basis functions that were utilized as a linear combination to define the shape of the mirror back-structure. Choosing the coefficients of the linear combination was a relatively straightforward process that used computer optimization to minimize a cost function (in that case, actuator-induced residual). The subtler problem is selecting the form of the basis functions in the first place. Budinoff & Michels chose a radial power series combined with two circumferential sinusoids with 6- and 12-fold periodicity. The authors selected these basis functions because they span the space

of possible shapes for the SPOT hexagonal mirror [41]. This chapter investigates candidate basis functions for rib-stiffened mirrors with surface-parallel actuators. The following sections present two such candidates along with results that demonstrate their respective ability to mitigate actuator-induced residual. After considering rib shaping, this chapter then considers a different approach wherein the ribs are more smoothly blended into the facesheet.

## 5.1 Parabolic rib shaping

In searching for basis functions with which to represent substrate shaping, analyzing the residual provides insights as to which shapes may offer the most promise. Figure 4-5 shows a residual profile with high spatial frequency variation within a low frequency envelope. The high frequency component is considered in Section 5.2 below, while the low frequency envelope is the topic of this section. This envelope appears reasonably quadratic, hence the first shaping function attempted is a parabolic radial variation in rib height. Figure 5-1 shows a sample mirror with such a shaping function applied to the rib structure.

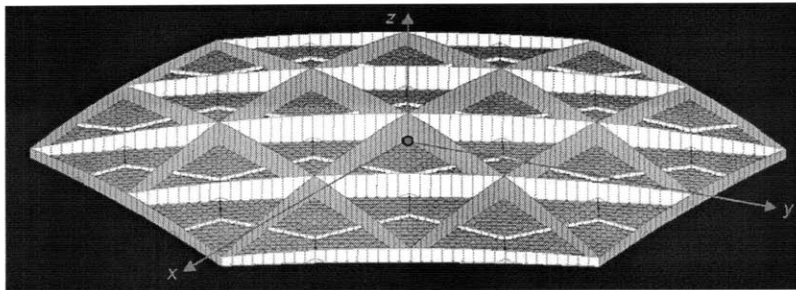


Figure 5-1: Mirror with a parabolically shaped substrate; from Gray [31].

### 5.1.1 Implementation

The parabolic rib shaping function is parameterized by the quantity  $a$ , which is defined as the difference in rib height between the center and edge of the mirror, i.e.

$$a \equiv h_{\text{rib}}(r = R_{\text{hex}}) - h_{\text{rib}}(r = 0) \quad (5.1)$$

where  $R_{\text{hex}}$  is “hexagonal” radius as given by half the point-point diameter. When  $a$  is negative, the ribs are taller in the center of the mirror and taper to a shorter height near the edges; this is the case in Figure 5-1. Conversely, when  $a$  is positive, the ribs are taller at the edge of the mirror compared to the center. The finite element mirror model was used to calculate quilting and max  $\Delta\text{RoC}$  from  $a = -10$  mm to  $a = +10$  mm. For each mirror realization, a DC term is added or subtracted from the rib height across the entire back surface to maintain a constant areal density.

### 5.1.2 Results

Figures 5-2 and 5-3 show the results of this single-axis parameter study. The parabolic shaping function shows only modest performance gains over the range studied. Quilting in the the best-performing design ( $a = -10$  mm) was 23.9 nm RMS, compared with 25.4 nm RMS in the baseline mirror ( $a = 0$  mm)—a 6% reduction. Likewise, max  $\Delta\text{RoC}$  went from 0.59 mm in the baseline case to 0.63 mm, which is a 7% improvement. While the performance gains are modest, it should be noted that  $a$  was varied over a relatively small range compared to the rib height (25.4 mm in the baseline mirror). The 20 mm range was selected to be consistent with the sinusoidal case (below). Therefore, it may possible to extract larger gains from parabolic shaping by using a larger magnitude for (negative)  $a$ . Still, even after extrapolating this trend, parabolic height variation yields limited increases in performance.

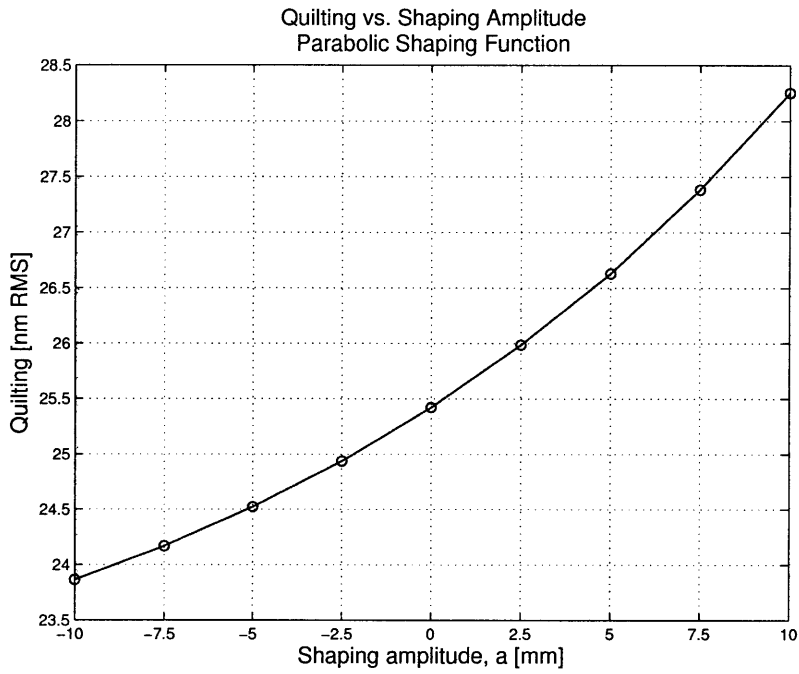


Figure 5-2: Actuator-induced quilting residual as function of parabolic shaping parameter  $a$ .

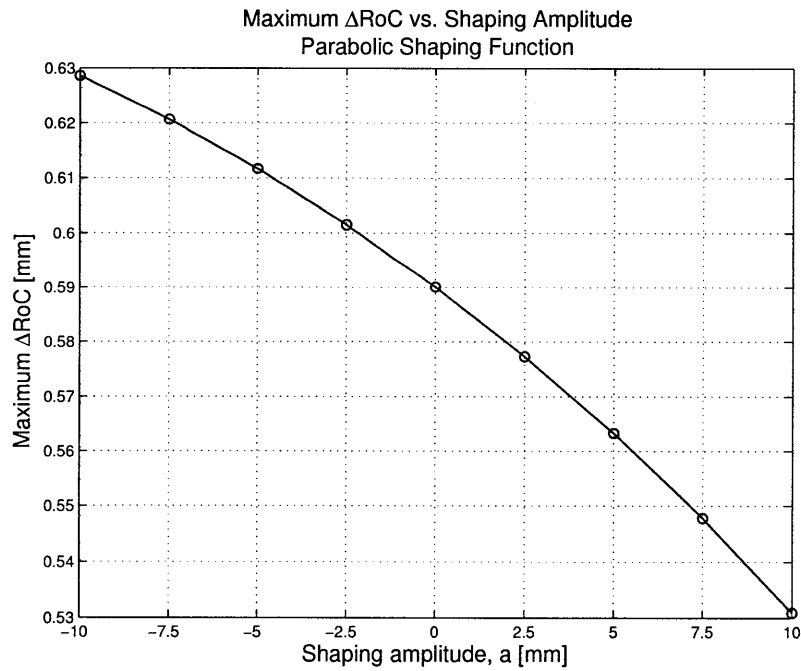


Figure 5-3: Operational flexibility (max  $\Delta$ RoC) as function of parabolic shaping parameter  $a$ .

## 5.2 Sinusoidal rib shaping

Recall from Section 4.1.2 that the actuator-induced residual has a strongly periodic nature due to the regular spacing of the embedded actuators. In seeking candidate basis functions for rib shaping functions, it is intuitive to seek periodic forms. Furthermore, the results in Section 4.1.2 revealed that the actuator influence function plays an important role; any rib shaping efforts that broaden the influence function will likely reduce quilting. This can be envisioned as more smoothly spreading the impulse-like actuator load into the mirror substrate.

### 5.2.1 Implementation

With this in mind, the finite element mirror model was used to evaluate the feasibility of a sinusoidal rib shaping function, shown in Figure 5-4. Here the height of each rib cell varies according to a cosine whose period is equal to the rib cell length. This shaping function was designed to address the above considerations regarding load spreading and influence function broadening.

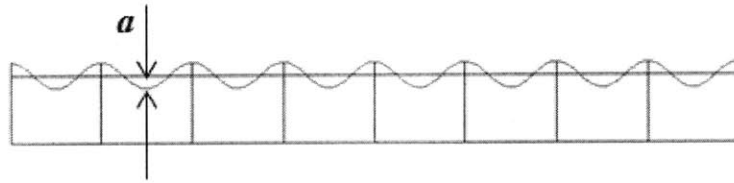


Figure 5-4: Side view of the sinusoidal shaping function applied to a set of rib cells, with shaping parameter  $a$ .

The sinusoidal shaping function is parameterized by  $a$ , the amplitude of the cosine profile with respect to the original non-shaped rib height. Note that using a sinusoid to vary the rib height is convenient because the average value is constant regardless of the choice of  $a$ . This ensures that the mirror areal density remains constant across the range of modeled  $a$  values.

Figure 5-5 shows the finite element mirror model before and after sinusoidal shaping has been added to the ribs. The amount of material near the rib vertices grows

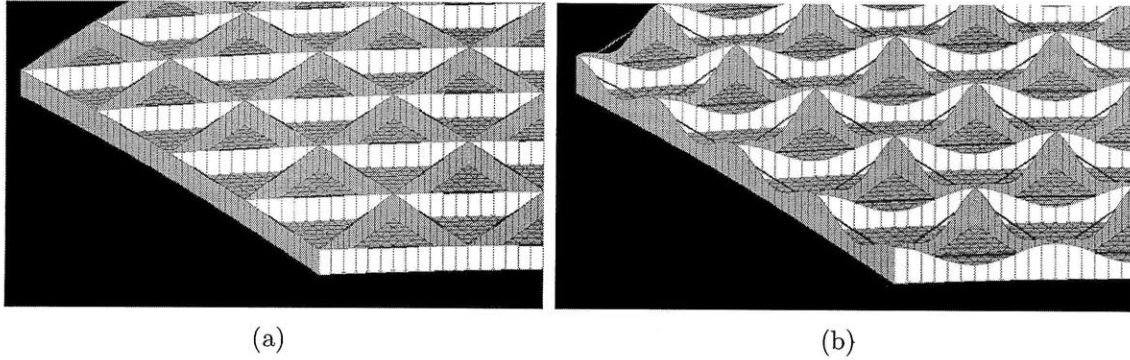


Figure 5-5: Mirror ribs with (a) no shaping function applied and (b) sinusoidal shaping with  $a = 10$  mm.

as  $a$  increases, leaving a trough in each rib cell spanned by the actuators. As with the parabolic shaping case above, the shaping parameter was varied over a range of 20 mm, however for the sinusoidal profile,  $a$  cannot be negative without impinging on the actuators. Therefore instead of  $-10 \text{ mm} \leq a \leq +10 \text{ mm}$ , the shaping parameter varied from  $a = 0 \text{ mm}$  to  $a = 20 \text{ mm}$ .

### 5.2.2 Results

Mirrors were created for each value of  $a$  and subjected to the standard 1 mm  $\Delta\text{RoC}$  maneuver to calculate quilting and max  $\Delta\text{RoC}$ . The results are shown in Figures 5-6 and 5-7.

The simulation output shows that the sinusoidal shaping function reduces quilting and increases max  $\Delta\text{RoC}$  relative to the baseline case with constant rib height. A shaping amplitude of  $a = 12.5$  mm is optimal over the range modeled. When moving from  $a = 0$  mm to  $a = 12.5$  mm, quilting decreases from 25.4 nm RMS to 18.6 nm RMS (a 27% reduction) and max  $\Delta\text{RoC}$  increases from 0.59 mm to 0.81 mm (a 37% improvement). While the performance gains are not as drastic as the actuator lengthening case, the results are significant nonetheless and demonstrate the potential usefulness of the proposed sinusoidal basis function.

The surface residual map—i.e. the difference between the desired and actual surface change—reflects the above findings. Figure 5-8 shows the value of the residual



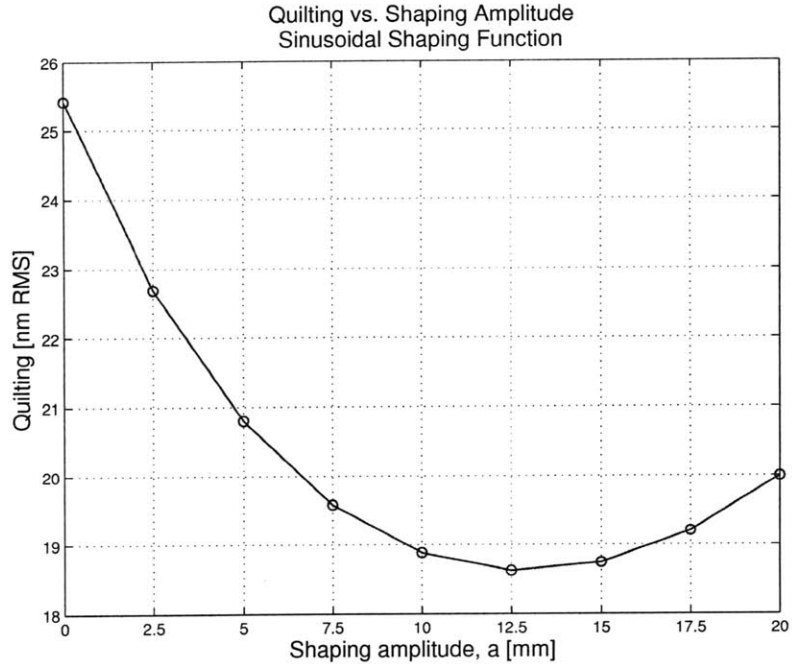


Figure 5-6: Actuator-induced quilting residual as function of sinusoidal shaping parameter  $a$ . Quilting is minimized for  $a = 12.5$  mm.

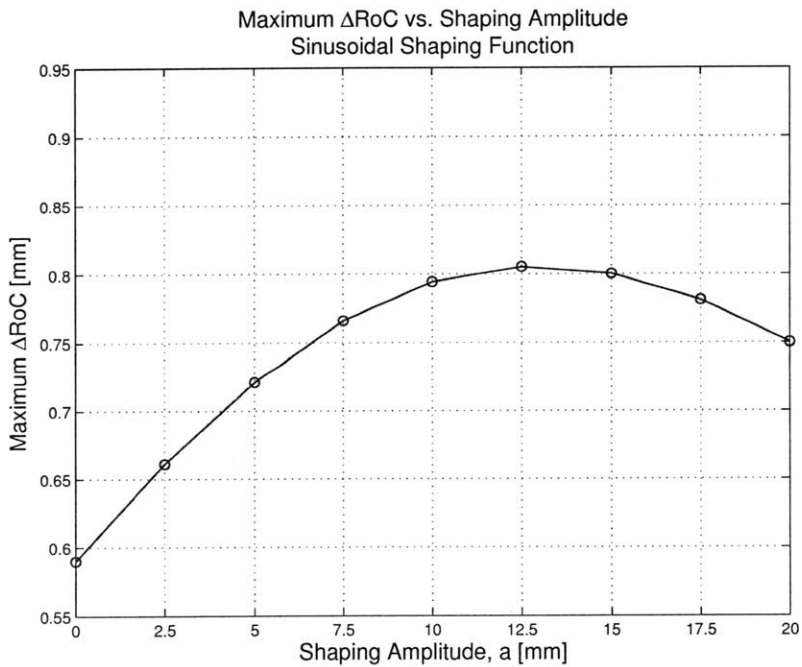


Figure 5-7: Operational flexibility (max  $\Delta RoC$ ) as function of sinusoidal shaping parameter  $a$ . Max  $\Delta RoC$  is maximized for  $a = 12.5$  mm.

after taking a horizontal slice through the mirror surface at  $y = 0$ . Vertical dashed lines denote the rib cell boundaries. There is a clear reduction in the residual amplitude when using sinusoidal shaping with  $a = 12.5$  mm. This translates into a reduced value for quilting when the residual map grid points are combined using the RMS operation.

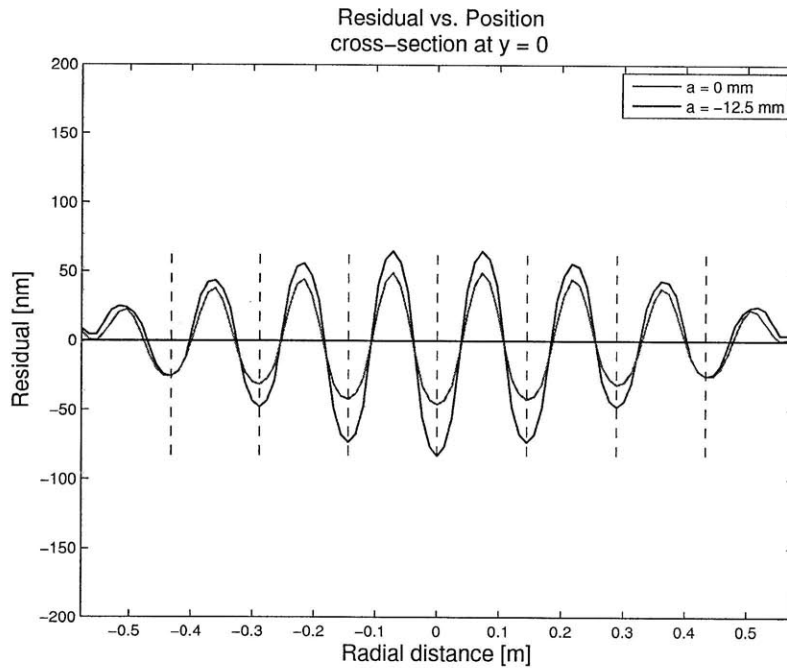


Figure 5-8: Comparing residual across the mirror surface for zero rib shaping and sinusoidal shaping with  $a = 12.5$  mm

As with the case of actuator geometry (Chapter 4), additional insights can be gained by comparing the influence functions in the baseline and optimal case. This is shown in Figure 5-9, where increasing the shaping amplitude increases the spread of the influence function in a manner similar to that of actuator lengthening. This is difficult to see from the contour plots, so Figure 5-10 shows slices of the contour plots taken through the horizontal (a) and vertical (b) lines shown in Figure 5-9.

As the shaping amplitude increases, the spread of the influence function increases both along the rib (the horizontal slice) and perpendicular to the rib into the facesheet (the vertical slice). This is remarkable given that only the substrate geometry changes, yet the influence function is broadened as if the actuator is lengthened. Therefore si-

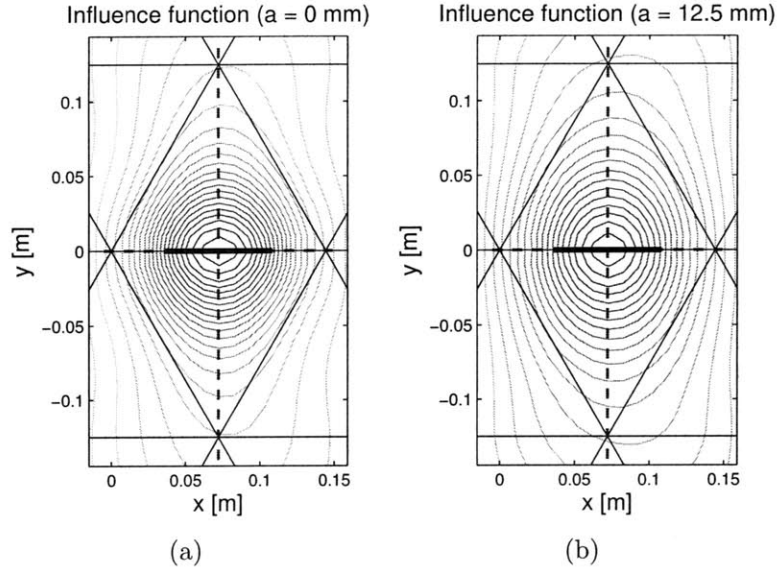


Figure 5-9: Zoomed view of an influence function for the case of (a) zero rib shaping and (b) sinusoidal shaping with  $a = 12.5$  mm.

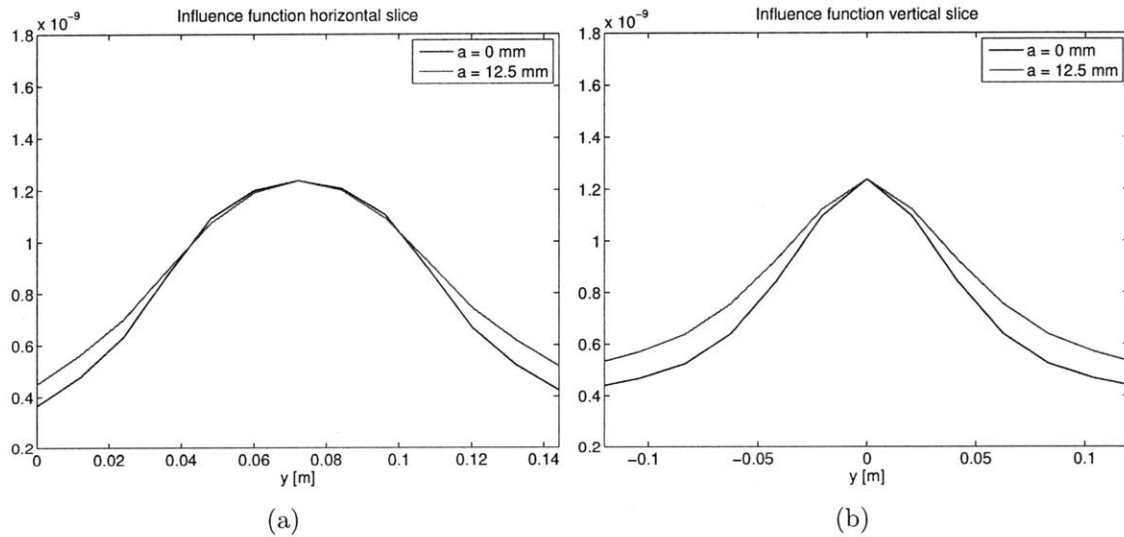


Figure 5-10: Horizontal (a) and vertical (b) slices along the dashed lines shown in Figure 5-9.

sinusoidal rib shaping is a suitable alternative when manufacturing constraints prohibit the actuators from becoming longer. Care must be taken, however, to establish the correct shaping amplitude. Quilting will begin to increase if the shaping is increased past the optimal value due to the fact that additional material is being removed from

the ribs. As the rib gets shorter in the center of the rib cell, it offers less stability to the facesheet, which eventually starts folding under the strain of the actuators. This accounts for the increase in quilting past  $a = 12.5$  mm in Figure 5-6.

### 5.2.3 Actuator length variation

Having shown that sinusoidal shaping can be used to reduce actuator quilting, it is useful to explore whether or not this effect is dependent on the length of the embedded actuator. Intuition suggests that there may be a relationship between the period of the sinusoid and the actuator length. Furthermore, the actuator lengths in actual prototype mirrors tend to be considerably shorter than the 7.2 cm baseline used in this thesis.

To address these questions, quilting and max  $\Delta\text{RoC}$  were calculated over a range of  $a$  using three actuator lengths: the baseline ( $l = 7.2$  cm), a shorter actuator ( $l = 2.4$  cm), and a longer actuator ( $l = 12.0$  cm). Figures 5-11 and 5-12 show the results. As noted in the previous chapter, increasing the actuator length results in decreased quilting and increased max  $\Delta\text{RoC}$ . Consequently, the three curves are substantially displaced with respect to each other along the vertical axes. As for variation as a function of  $a$ , it is clear that  $a = 12.5$  mm minimizes quilting for the 2.4 cm actuator case in addition to the baseline. This is encouraging, as it shows that shaping can still have an effect in the more realistic implementation with shorter actuators. Interestingly, there is no local minimum in the center of the parameter space for the 12.0 cm actuator case. The baseline of no shaping offers the best performance when the actuators are long. Tables 5.1 and 5.2 summarize these results in terms of percent change between the baseline and best cases.

While the performance gains using substrate geometry variation are less pronounced than using actuator geometry variation, such an approach may be useful when constraints—manufacturing or otherwise—prohibit changes to the actuator design. The above results indicate that sinusoidal shaping should be considered as a basis function when conducting a more extensive SPOT-like optimization of mirror substrates (see Chapter 6 for details).

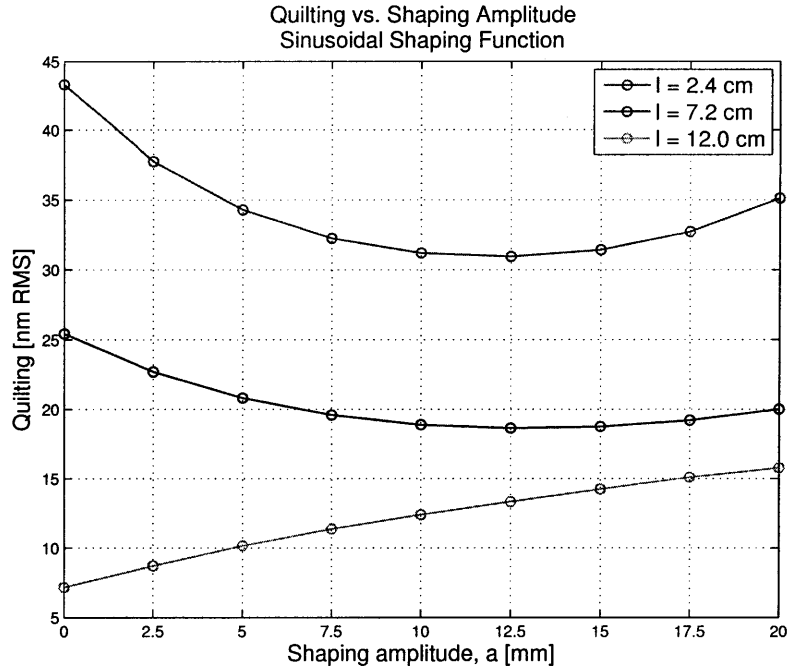


Figure 5-11: Actuator-induced quilting residual as function of sinusoidal shaping parameter  $a$  for actuator lengths  $l = \{2.4, 7.2, 12.0\}$  cm.

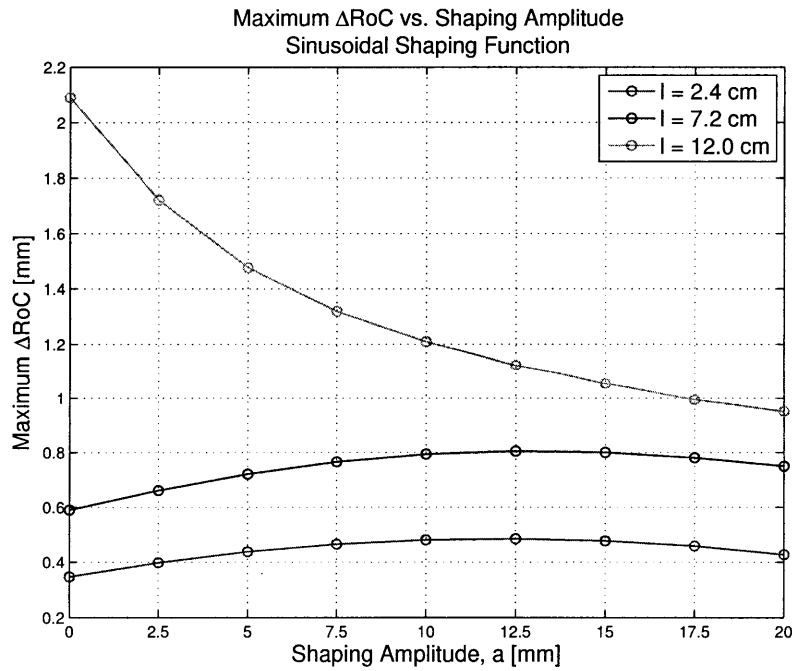


Figure 5-12: Operational flexibility (max  $\Delta\text{RoC}$ ) as function of sinusoidal shaping parameter  $a$  for actuator lengths  $l = \{2.4, 7.2, 12.0\}$  cm.

Table 5.1: Summary of quilting results for combined shaping and actuator length variation.

Actuator length [cm]	Quilting [nm RMS] (baseline)	Quilting [nm RMS] (best)	Change
2.4	43.3 ( $a = 0$ )	30.9 ( $a = 12.5$ )	-29%
7.2	25.4 ( $a = 0$ )	18.6 ( $a = 12.5$ )	-27%
12.0	7.2 ( $a = 0$ )	7.2 ( $a = 0$ )	n/a

Table 5.2: Summary of operational flexibility (max  $\Delta\text{RoC}$ ) results for combined shaping and actuator length variation.

Actuator length [cm]	max $\Delta\text{RoC}$ [mm] (baseline)	max $\Delta\text{RoC}$ [mm] (best)	Change
2.4	0.35 ( $a = 0$ )	0.48 ( $a = 12.5$ )	+37%
7.2	0.59 ( $a = 0$ )	0.81 ( $a = 12.5$ )	+37%
12.0	2.09 ( $a = 0$ )	2.09 ( $a = 0$ )	n/a

### 5.3 Rib blending

The substrate geometry variations considered thus far all consist of changing the height of the ribs. This along-rib shaping was found to spread the actuator loads and expand the influence function shape, improving performance in the case of low order prescription changes (i.e.  $\Delta\text{RoC}$ ). In the above cases, however, the rib meets the facesheet at a  $90^\circ$  angle regardless of shaping function used. A natural extension of load spreading via rib shaping is to use rib-to-facesheet blending to accomplish the same thing. In such an arrangement, the sharp  $90^\circ$  junction between the rib and facesheet is replaced by a smooth transition that expands the influence function perpendicularly away from ribs in addition to expanding it along the ribs. Options for rib-to-facesheet blending are shown in Figure 5-13.

Figure 5-13b shows the geometry of a standard rib, with a section of the mirror facesheet facing downward. In this arrangement the rib is similar to a fence in the ground: it meets the facesheet at a right angle. Figure 5-13c shows an implementation of blending wherein the transition from the rib to the facesheet is a linear ramp. Slope

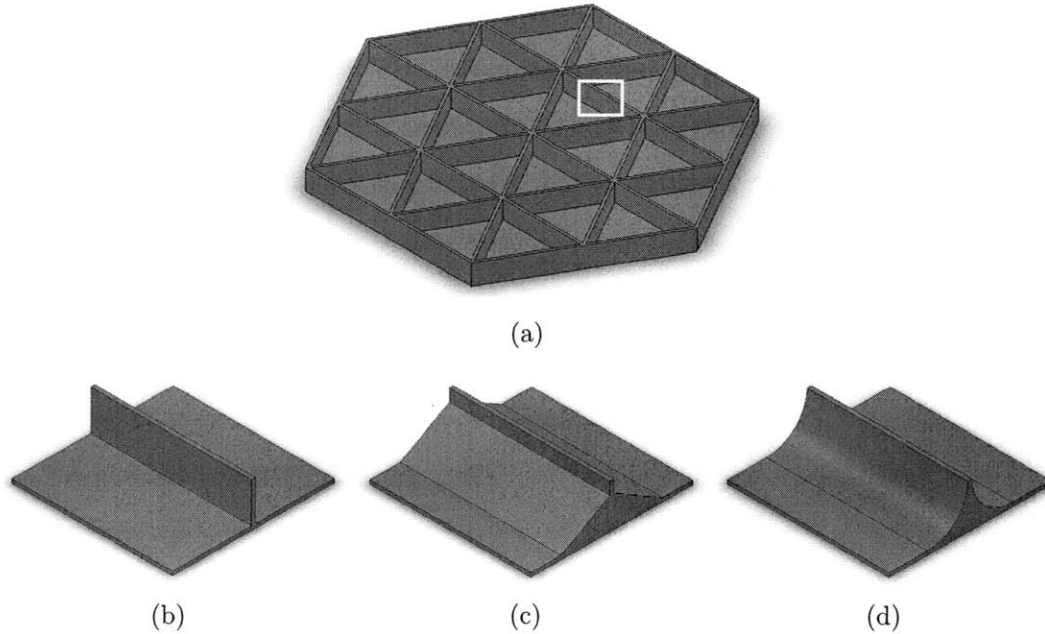


Figure 5-13: Rib blending options. (a) Location of figures (b)-(d) in the mirror rib structure (white square), (b) a standard mirror rib wherein the rib-facesheet junction is  $90^\circ$ , (c) rib that uses linear blending between the rib and facesheet, and (d) rib with smoothed rib-to-facesheet blending.

discontinuities still exist where the linear ramp intersects the rib and the facesheet, however the  $90^\circ$  junction has been eliminated. Figure 5-13d shows an intersection in which the rib smoothly blends into the facesheet. In the case shown, the blending profile on either side of the rib is one quarter of a cylinder, thus both the rib and facesheet are tangent to the profile and there are no slope discontinuities.

### 5.3.1 Implementation

The finite element mirror model was used to assess the potential benefits of rib-to-facesheet blending. The linear blending profile (Figure 5-13c) was modeled as a first case. As currently implemented, the mirror model uses 2D plate elements—specifically CTRIA3 and CQUAD4—to construct the facesheet and ribs, respectively. While Jordan [37] built a plate mirror model using 3D elements, the MOST model is generally limited to 2D elements. As a proxy for the 3D nature of the linear blending, the thicknesses of the facesheet elements were varied such that the facesheet cell has

a linearly increasing thickness profile starting from nearly zero at the center. This is depicted in Figure 5-14. Note that volume of the facesheet material within the blended facesheet cell is conserved, therefore there is no change in the mirror areal density.

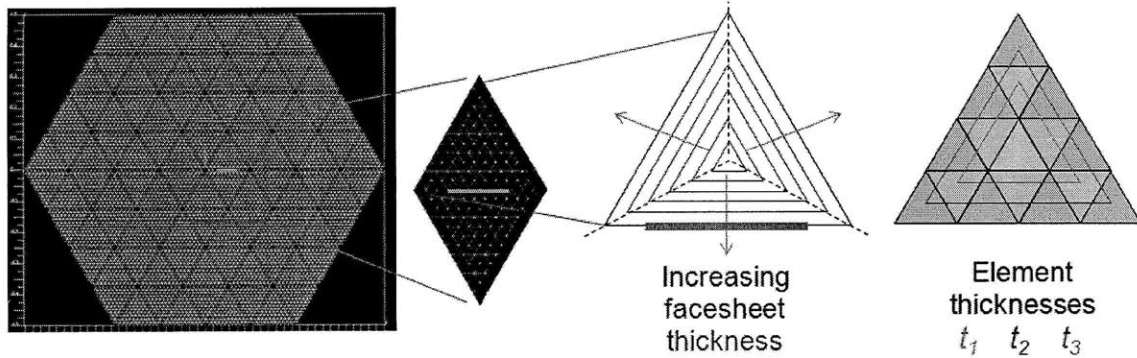


Figure 5-14: Linear rib-to-facesheet blending using 2D triangular plate elements with varying thickness. In this implementation, the facesheet thickness increases linearly from the center of the facesheet cell.

### 5.3.2 Results

Rib-to-facesheet blending was implemented as described above in a pair of facesheet cells straddling a single cylindrical actuator. The influence function for this actuator was then calculated and the results were compared to the non-blended case. These results are shown in Figure 5-15, which reveals a slight vertical elongation of the influence function when moving from the non-blended case to the blended one. This result is intuitive from the standpoint of spreading the actuator load away from the rib and into the two adjacent facesheet cells. Taking horizontal and vertical slices (Figures 5-16a and 5-16b, respectively) confirms this observation. The horizontal slice taken along the rib direction is practically unchanged. The vertical slice, however, shows a broadening of the influence function. Thus rib-to-facesheet blending does offer an ability to broaden the influence function and, following the results from previous sections, potentially reduce actuator quilting.



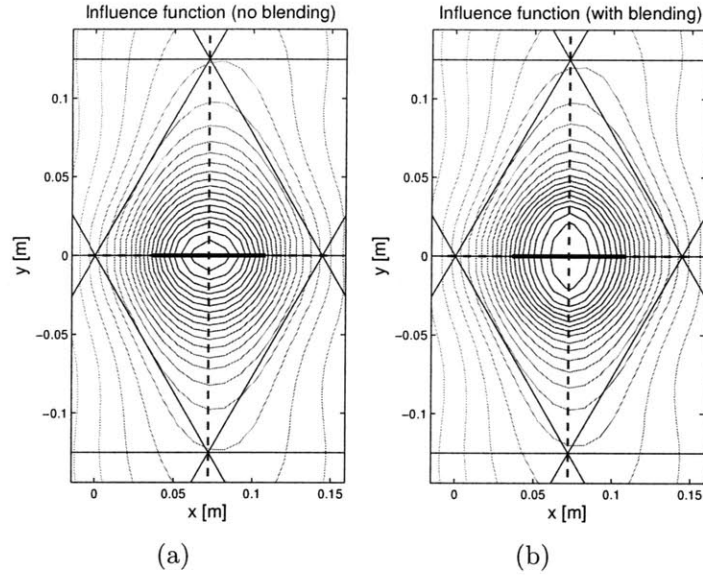


Figure 5-15: Zoomed view of an influence function (a) without blending and (b) with blending.

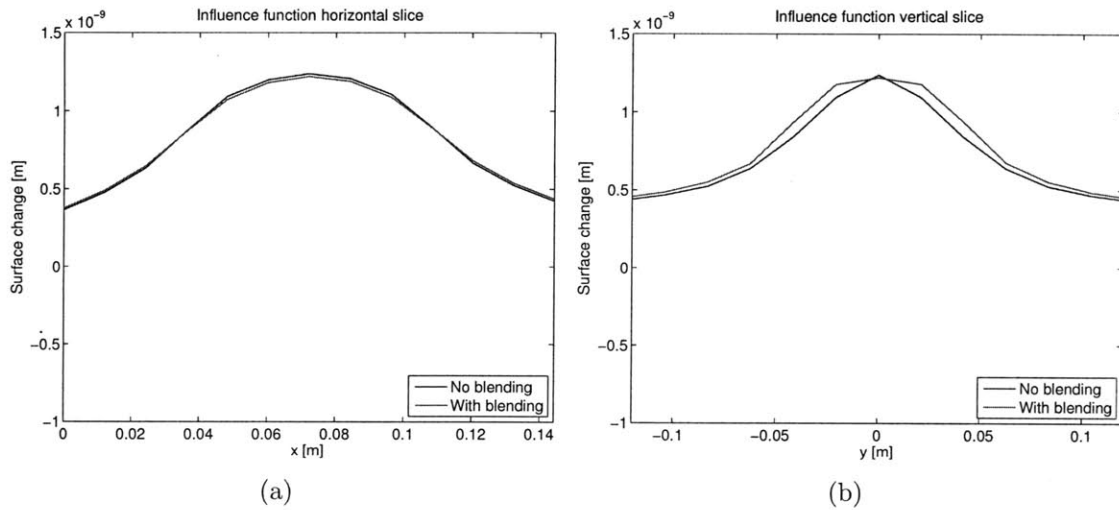


Figure 5-16: Horizontal (a) and vertical (b) slices along the dashed lines shown in Figure 5-15.

### 5.3.3 Limitations

Despite the promising results, there are several limitations to the current implementation of rib-to-facesheet blending. First, the process described above ignores manufacturing limits for minimum facesheet thickness. By assigning the linear profile

depicted in Figure 5-14 and by redistributing all of the facesheet material, the current implementation causes the CTRIA3 elements at the center of the facesheet cells to have very low thickness. Actual implementations of such blended features would have lower limits on manufacturable facesheet thickness that would prevent such a thin facesheet at the cell centers.

Second, this initial study only modeled a single pair of facesheet cells. Changes to the auto-mesh code could allow the user to rapidly generate a blended facesheet and evaluate the effect of simultaneously increasing the width of all actuator functions. This would also allow for the parametrization of blending, permitting the type of study undertaken in the case of rib shaping above.

Finally, the current finite element model is composed entirely of 2D plate elements of varying thicknesses. With sufficiently fine mesh density, this approximates 3D blending. However a higher-fidelity implementation would use 3D elements to capture the complex geometry at the rib-facesheet interface. Employing 3D elements would open up a wide range of possible blending profiles, greatly expanding the design space and potentially allowing further reductions in actuator quilting.

## 5.4 Summary

This chapter presents several variations in mirror substrate geometry along with the associated effects on actuator-induced quilting. Along-rib shaping is explored first using two candidate basis functions: parabolic and sinusoidal. These are parameterized representations of rib height that act as low and high spatial frequency basis functions, respectively. There is slight performance increase of approximately 6% to 7% when using parabolic rib shaping. Sinusoidal shaping, on the other hand, offers a more significant benefit. In this latter case, quilting was reduced by 27% and operational flexibility (max  $\Delta\text{RoC}$ ) increased 37% over the baseline values. This improved performance is due the influence functions, which tend to broaden when the ribs take on a sinusoidal profile. The effect is similar to that seen in Chapter 4 when lengthening the actuators. Sinusoidal rib shaping is explored for shorter and longer actuators

than the baseline case of  $l = 7.2$  cm. The results show that such shaping is beneficial in the case of short actuators, but can actually be detrimental for long actuators. Finally, this chapter also explores rib-to-facesheet blending as another possible form of substrate geometry variation. This is done using a linearly varying thickness profile in two facesheet cells. The idea, as in rib shaping, is to smooth the load from the actuator to the facesheet, and in doing so, broaden the influence function to reduce quilting. After implementing the concept using 2D plate elements, the simulation results showed modest success in expanding the influence function in the direction perpendicular to the actuator. Further studies of blending should use 3D elements, which would expand the space of blending profiles that can be modeled.



# Chapter 6

## Conclusion

The research objective of this thesis is to reduce actuator-induced high spatial frequency residual error by manipulating mirror geometry using a parametric finite element model, while keeping areal density and number of actuators constant. A subsequent and complementary aim is to bound the range of prescription changes attainable through surface-parallel actuation in lightweight rib stiffened mirrors. This work shows that it is indeed possible to reduce mirror quilting through judicious use of actuator and substrate geometry. Several designs are identified which achieve an increase in performance without adding actuators—and hence complexity—or mass. This chapter summarizes these outcomes and proposes several follow-on studies for future work.

### 6.1 Thesis summary

Chapter 1 presents a background on space telescope technology, the thesis motivation in terms of high spatial frequency residual error, and an overview of the Modular Optical Space Telescope (MOST) finite element model. The move to lightweight actively-controlled silicon carbide (SiC) mirrors is traced back to previous generations of space telescope mirror technology, specifically the James Webb Space Telescope (JWST) and Hubble Space Telescope (HST). While actively controlled rib-stiffened mirrors offer mass and volume savings, actuator quilting imposes a limit on imaging

performance. This is the primary motivation for the research.

Chapter 2 provides an overview of relevant literature and identifies the gap to be filled by this thesis. Prior research is divided into three main areas: finite element mirror modeling, rib-stiffened space telescope mirrors, and shape optimization to decrease high frequency residual. Recent work by Gray [31, 32] and Cohan [8, 12, 11] applies finite element modeling to the case of rib-stiffened mirrors. Budinoff & Michels [4] and Park et al. [49] use finite element models along with geometrical optimization to reduce mirror surface errors. A gap exists between these two groups of authors, wherein geometry variation may be applied to the case of rib-stiffened SiC mirror designs.

### 6.1.1 Modeling approach

Chapter 3 contains a detailed description of the modeling approach used in this thesis: parametric variation of a high fidelity finite element mirror model. Nastran and Matlab are used to automatically create a single hexagonal mirror segment based on a user-supplied parameter file. This allows for the generation and evaluation of many geometric design features without the need for time-consuming meshing by hand. Relevant parameters include the optical figure, rib geometry, actuator geometry, constraints, and areal density. A four rib-ring, 1 m flat-flat diameter baseline configuration is used throughout the thesis for consistency. Likewise, the standard prescription change used in this work is a 1 mm increase in radius of curvature (RoC).

An analogy between thermal and piezoelectric strains is used to model the actuators via coefficient of thermal expansion (CTE) effects in Nastran. Mirror figure control is a two step process. First, a set of influence functions is collected by sequentially commanding individual actuators and recording the mirror surface displacements. Then, a least-squares minimization via the Moore-Penrose pseudoinverse determines the set of actuator commands that create a desired radius of curvature change.

In addition to allowing the rapid generation of mirror designs, one advantage of the model used here is tremendous flexibility in the definition of figures of merit.

This thesis discusses several: actuator-induced high frequency residual error (quilting), wavefront error (WFE), operational flexibility ( $\max \Delta\text{RoC}$ ), and Strehl ratio. These metrics are inter-related, with WFE being twice the quilting and  $\max \Delta\text{RoC}$  being defined in terms of a 30 nm RMS limit on WFE. Likewise, Strehl ratio is inversely related to the amount of quilting present on the mirror surface. Quilting and  $\max \Delta\text{RoC}$  are the main figures of merit used in this work, given that they are best aligned with the objectives of reducing actuator-induced residual error and bounding the range of achievable prescription changes.

Several common approaches to wavefront sensing are considered: the Shack-Hartmann wavefront sensor, the Twyman-Green interferometer, and iterative phase retrieval. Due to the quasi-static nature of the control scheme and following the trend in advanced segmented optical systems, this thesis assumes phase retrieval is used to measure the mirror shape. Instead of performing a phase retrieval algorithm, however, the model simply uses the mirror surface grid point locations as a proxy for wavefront knowledge. This is conservative, as the camera performing the sensing would typically have many more pixels than there are grid points in the model.

Finally, Chapter 3 gives a summary of the steps taken to verify the model. The convergent behavior of mirror stiffness and quilting is verified for increasing mesh density. These two metrics are also shown to closely match empirical data from hardware test beds.

### **6.1.2 Results for actuator geometry variation**

Chapter 4 presents results on the effect of parametric variations in actuator geometry. Embedded surface-parallel electrostrictive actuators are considered first. A range of actuator lengths is simulated, revealing a significant reduction in quilting for longer actuators. Specifically, changing the actuator length from the baseline value of 7.2 cm to 12.0 cm results in a 72% decrease in the amount of quilting and a factor of 2.5 increase in  $\max \Delta\text{RoC}$ . Influence functions are found to be the underlying reason for this improvement. Specifically, a longer actuator results in a larger, less-localized influence function. This is true not only along the rib, but also perpendicular to the

rib into the facesheet cell. Actuator coverage over the mirror surface is improved with these larger influence functions, hence smooth prescription changes such as  $\Delta\text{RoC}$  can be actuated with less residual. Shorter actuators exhibit the reverse: by effectively increasing the “discrete-ness” of the influence functions, short actuators have difficulty obtaining the necessary mirror coverage and result in higher quilting.

After presenting results for the finite element model, Chapter 4 develops two actuation models based on the theory of linear elastic mechanics. These models are derived using the 1D ordinary differential equation that describes a prismatic beam in bending. The beam is analogous to the mirror ribs and the embedded actuators are modeled as a moment couple. After defining the bending moment and boundary conditions appropriately, the beam equation is integrated twice to obtain an expression for beam (i.e. rib) deflection as a function of bending moment (i.e. actuator command). Singularity functions—a set of piece-wise differentiable curves—are found to be particularly useful in defining moments and deflections.

This analytical approach, developed from first principles, provides additional insights on the relationship between longer actuators and a broader along-rib influence function. The beam region between actuators is found to be quadratic and concave downward, matching the curve of the intended parabola better than the linear or concave up regions outside of the actuators. The extent of this quadratic region depends only on the spacing of the moment couples, indicating that actuator length as a fraction of rib cell size is a key parameter for determining influence function size. The actuator lengthening effect can therefore be achieved by simply increasing the separation distance between the actuator mounting points. This can be accomplished using actuator extension tabs, however actuator stroke may impose a limitation.

### **6.1.3 Results for substrate geometry variation**

Changes in actuator geometry of the type discussed above may not always be feasible due to constraints on actuator manufacturing. Chapter 5 therefore presents studies on the effect of changing the mirror substrate geometry, which may offer more design flexibility due to the casting method of manufacturing. The goal is to identify,



via parametric single-axis variation, a set of basis functions that could serve as the foundation of future rib shaping optimizations (see Section 6.3 below).

The first substrate variation considered is parabolic shaping of the ribs. This is parameterized by a single quantity that determines the relative height between ribs at the center of the mirror and those at the edge. Designs with increasing and decreasing radial rib height were simulated separately, and the results showed a slight reduction in quilting residual for the case of decreasing rib height near the mirror edge. Areal density and actuator geometry was held constant during these investigations.

A more promising basis function candidate is a sinusoidal rib shaping profile. Instead of being flat, each rib cell has a cosinusoidal height variation whose period is equal to that of the rib cell length. The shaping function is parameterized by the amplitude of the cosine. This is a convenient basis function because changing the amplitude parameter keeps the average rib height the same. Therefore the mirror areal density is automatically maintained across the range of amplitudes modeled. Simulations results show that actuator-induced residual is minimized for an amplitude of 12.5 mm, which gives a 27% reduction relative to the baseline (flat rib) case. Comparing actuator influence functions between the baseline and optimal case, the shaped rib showed a broader region of influence both along the rib and perpendicularly away from rib into the facesheet. This behavior—essentially making the actuator appear less “discrete” through a broadening of the influence function—mimics that of actuator lengthening. Therefore sinusoidal rib shaping may be a solution to reducing quilting when manufacturing constrains limit actuator length.

Finally, Chapter 5 introduces rib-to-facesheet blending as another means of altering the substrate geometry. Instead of having mirror ribs that intersect the back of the facesheet at a sharp right angle, blending attempts to smooth the transition from rib to facesheet. The idea is to more effectively spread the load from the rib actuators into the surrounding facesheet cells. The goal is to create a broader influence function in the direction perpendicular to a given rib cell. While an ideal finite element implementation would use 3D elements, an initial attempt was made using 2D elements with linearly varying thickness. As before, the substrate material

is allocated so as to maintain areal density. The results show a modest broadening of the influence function as intended, with almost no changes in the along-rib direction.

## 6.2 Thesis contributions

Below is a summary of the main contributions of this thesis.

- Quantified the dependence of actuator-induced residual error on actuator length.
  - Determined the range of prescription changes attainable using embedded surface-parallel actuators of varying lengths.
  - Analyzed performance gains by considering actuator influence function size and consequent coverage over the mirror surface.
  - Derived analytical mirror deflection models using the mechanics of linear elastic beams and used the results to interpret finite element results in terms of spacing between actuator moment couples.
- Demonstrated the desirable influence function characteristics of 2D patch actuators affixed to the mirror facesheet.
- Introduced the concept of substrate shape optimization to reduce actuator quilting effects in rib-stiffened space telescope mirrors.
  - Identified a sinusoidal basis function for rib shaping.
  - Demonstrated that rib shaping can reduce high spatial frequency residual due to actuator effects, while keeping areal density constant.
  - Demonstrated the benefits of rib-to-facesheet blending in terms of broadening influence functions.

## 6.3 Future work

This thesis presents several first steps in the process of exploring creative geometry variation in rib-stiffened actively controlled space telescope mirrors. The purpose

of this section is to outline a set of proposed follow-on investigations that build on the present research. The ultimate goal is a highly optimized, geometrically efficient substrate design that balances stiffness, mass, and quilting performance. Such a design, described in the concluding paragraphs of this section, would leverage existing techniques for the manufacture of replicated reaction bonded SiC substrates.

With regard to actuation, a natural next step is to expand on the results on patch actuators given in Section 4.4. The present work showed that patch actuators have the potential to offer a new set of highly localized influence functions that reside within the facesheet cells. This would fill in the “gaps” in coverage that arise when using only using rib-embedded cylindrical actuators. The finite element model auto-mesh code would need to be updated to generate this new set of actuators. Once implemented, the patch actuators could be commanded via the same means as the cylindrical ones. The influence function matrix  $H$  would then include surface maps for both types of actuators, however the command solution would be carried out using the same least-squares approach. Given the complimentary nature of cylindrical and patch influence functions, it is suspected that this would offer significant gains in terms of quilting, however at a cost in terms of mass, power, and complexity.

Key to the work of Budinoff & Michels on SPOT was the identification of a suitable set of basis functions that were used to parameterize and then optimize the shape of the mirror substrate. A first step in performing this substrate optimization is to find the rib shape that minimizes quilting. The single-axis parameter studies in Sections 5.1 and 5.2 explored initial rib basis functions. The sinusoidal variation was particularly effective, therefore a series of cosines centered on each rib cell is a promising basis. An optimization routine could be used to find weights on a Fourier series-type sum that produces the least quilting (see Figure 6-1).

As discussed in Section 5.3, adjusting rib-to-facesheet blending is another means of optimizing the substrate geometry to minimize quilting. The model used in this thesis used 2D elements exclusively, but an implementation with 3D elements would allow many more parameterizations of the blending profile. As a result, the design space would become significantly larger and an extensive optimization of the blending

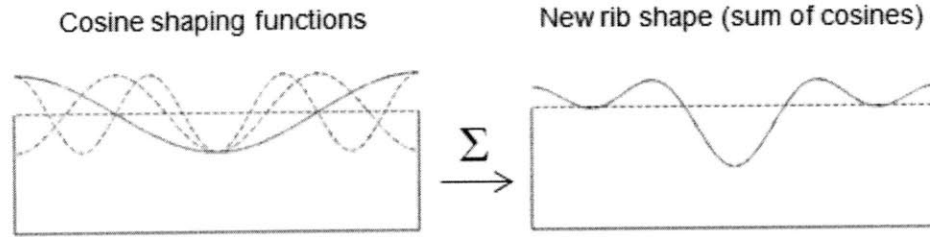


Figure 6-1: Concept for a new rib shape as an optimized sum of cosine shaping functions. A single rib cell is shown.

topology could yield resins with lower quilting than would be otherwise possible without blending. Such an optimization, however, must consider the stiffening effect that arises due to features intersecting at right angles. As blending increases, the ribs are less able to provide stiffness to the facesheet, which could prevent the mirror from surviving launch [8]. The proposed optimization could either treat stiffness as a constraint that must be satisfied, or use multi-disciplinary optimization (MDO) techniques to find a Pareto front that trades between quilting and stiffness.

Once a set of basis functions is separately established for rib shaping and rib-to-facesheet blending, a proposed next step is to conduct a combined optimization using both sets. The ultimate goal is a rib-stiffened mirror that contains a combination of shaped and blended features that more efficiently spread loads throughout the structure so as to minimize actuator quilting. This evolution is shown in Figure 6-2.

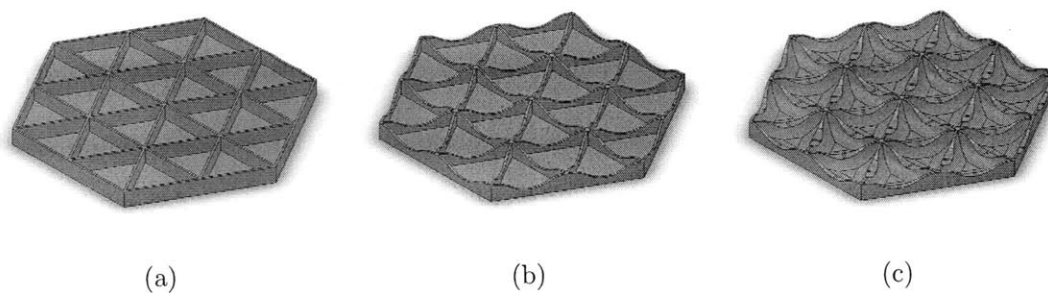


Figure 6-2: (a) Standard mirror substrate with constant rib height, (b) mirror substrate with along-rib shaping, and (c) mirror substrate with along-rib shaping and rib-to-facesheet blending.

This proposed substrate geometry optimization could be used in conjunction with

cylindrical actuators, patch actuators, or both. Stress analysis would be a necessary accompaniment to this optimization for the reason stated above—i.e. increasing the amount of blending, while beneficial from a quilting standpoint, could decrease stiffness to a point that the mirror cannot survive launch.

The output of this optimization would be a completely new family of highly optimized, blended and shaped lightweight mirror architectures. It would represent a new paradigm in mirror design. Instead of creating specialized actuators to augment an existing rib-stiffened mirror layout, this process treats actuator geometry as generally fixed and attempts instead to customize the substrate. This is intended to leverage the mold and casting process by which replicated SiC substrates are fabricated—a method much better suited to complex geometrical features than the traditional approach of milling ribs out of a metal blank. The blended structures can be machined into the substrate mold as a one-time process, and replicating multiple segments from this single mold would spread the development costs over multiple mirrors. The result would be a relatively low-cost, highly adaptable mirror segment optimized for low mass, sufficient stiffness, and minimal actuator-induced residual error.



# Bibliography

- [1] Ferdinand P. Beer, E. Russell Johnston, John T. Dewolf, and David F. Mazurek. *Mechanics of Materials*. McGraw-Hill, 5th edition, 2009.
- [2] Siddarayappa Bikkannavar, Catherine Ohara, and Mitchell Troy. Autonomous phase retrieval control for calibration of the Palomar adaptive optics system. *Proc. SPIE*, 7015, 2008.
- [3] Max Born and Emil Wolf. *Principles of Optics*. Pergamon Press, 6th edition, 1980.
- [4] Jason G. Budinoff and Gregory J. Michels. Design and optimization of the Spherical Primary Optical Telescope (SPOT) primary mirror segment. *Proc. SPIE*, 5877, 2005.
- [5] David M. Chaney, Robert J. Brown, Steve E. Kendrick, Patrick J. Reardon, and James B. Hadaway. Results of the beryllium AMSD mirror cryogenic optical testing. *Proc. SPIE*, 5487:833–841, 2004.
- [6] Lucy E. Cohan. Control system architecture for space telescopes. *AIAA Guidance, Navigation and Control Conference*, 6600, 2007.
- [7] Lucy E. Cohan. Integrated modeling to facilitate control architecture design for lightweight space telescopes. Master’s thesis, Massachusetts Institute of Technology, 2007.
- [8] Lucy E. Cohan. *Integrated Modeling and Design of Lightweight Active Mirrors for Launch Survival and On-Orbit Performance*. PhD thesis, Massachusetts Institute of Technology, 2010.
- [9] Lucy E. Cohan, Elizabeth O. Jordan, and David W. Miller. Tradespace exploration for a parameterized modular optical space telescope (MOST). *AIAA/ASME/ASCE/AHS/ASC Structures, Structural Dynamics, and Materials Conference*, 2245, 2007.
- [10] Lucy E. Cohan and David W. Miller. Dynamic wavefront control for lightweight mirrors in space telescopes. *Proc. SPIE*, 6687, 2007.
- [11] Lucy E. Cohan and David W. Miller. Integrated modeling for determining launch survival and limitations of actuated, lightweight mirrors. *Proc. SPIE*, 7010, 2008.

- [12] Lucy E. Cohan and David W. Miller. Vibroacoustic analysis and optimization of lightweight, silicon carbide mirrors. *Proc. SPIE*, 7436, 2009.
- [13] F. Côté, P. Masson, N. Mrad, and V. Cotroni. Dynamic and static modelling of piezoelectric composite structures using a thermal analogy with MSC/NASTRAN. *Composite Structures*, 65:471–484, 2004.
- [14] Bruce H. Dean, David L. Aronstein, J. Scott Smith, Ron Shiri, and D. Scott Acton. Phase retrieval algorithm for JWST flight and testbed telescope. *Proc. SPIE*, 6265, 2006.
- [15] Alan Dressler. HST and beyond - exploration and the search for origins: A vision for ultraviolet-optical-infrared space astronomy. *Association of Universities for Research in Astronomy, Inc.*, 1996.
- [16] Johannes K Dürr, Robert Honke, Mathias von Alberti, and Rudolf Sippel. Development and manufacture of an adaptive lightweight mirror for space application. *Smart Materials and Structures*, 12:1005–1016, 2003.
- [17] Mark A. Ealey. Large low temperature silicon carbide mirrors. *NASA Technology Days, Marshall Space Flight Center*, May 2002.
- [18] Mark A. Ealey. Large optics in the 21<sup>st</sup> century: A transition from discrete manufacturing to highly integrated techniques. *Proc. IEEE Aerospace Conference*, 4:1705–1716, 2003.
- [19] Mark A. Ealey. Integrated actuator meniscus mirror. *United States Patent*, 0165289, August 2004.
- [20] Mark A. Ealey. Integrated actuator meniscus mirror without reaction mass. *United States Patent*, 0046976, March 2005.
- [21] Mark A. Ealey. Agile mandrel apparatus and method. *United States Patent*, 0250672, November 2006.
- [22] Mark A. Ealey and Thomas R. Price. Actuator issues in deformable mirrors and adaptive optics. *Proc. SPIE*, 2865:50–53, 1996.
- [23] Mark A. Ealey and Gerald Q. Weaver. Developmental history and trends for reaction bonded silicon carbide mirrors. *Proc. SPIE*, 2857:66–72, 1996.
- [24] Mark A. Ealey and John A. Wellman. Highly adaptive integrated meniscus primary mirrors. *Proc. SPIE*, 5166:165–171, 2004.
- [25] Mark A. Ealey and John A. Wellman. High authority deformable optical system. *United States Patent*, 0262434, November 2006.
- [26] Mark A. Ealey and John A. Wellman. Method of fabricating replicated optics. *United States Patent*, 0249246, November 2006.



- [27] Lee D. Feinberg, Bruch H. Dean, David L. Aronstein, Charles W. Bowers, William Hayden, Richard G. Lyon, Ron Shiri, J. Scott Smith, D. Scott Acton, Larkin Carey, Adam Contros, Erin Sabatke, John Schwenker, Duncan Shields, Tim Towell, Fang Shi, and Luis Meza. TRL-6 for JWST wavefront sensing and control. *Proc. SPIE*, 6687, 2007.
- [28] Paul F. Forman. The zygo interferometer system. *Proc. SPIE*, 0192:41 – 48, 1979.
- [29] Jonathan P. Gardner, John C. Mather, Mark Clampin, Rene Doyon, Matthew A. Greenhouse, Heidi B. Hammel, John B. Hutchings, Peter Jakobsen, Simon J. Lilly, Knox S. Long, Jonathan I. Lunine, Mark J. McCaughrean, Matt Mountain, John Nella, George H. Rieke, Marcia J. Rieke, Hans-Walter Rix, Eric P. Smith, George Sonneborn, Massimo Stiavelli, H.S. Stockman, Rogier A. Windhorst, and Gillian S. Wright. The James Webb Space Telescope. *Space Science Reviews*, 123(4):485–606, April 2006.
- [30] Joseph W. Goodman. *Introduction to Fourier Optics*. Roberts & Company, 3rd edition edition, 2005.
- [31] Thomas L. Gray. Minimizing high spatial frequency residual in active space telescope mirrors. Master’s thesis, Massachusetts Institute of Technology, 2008.
- [32] Thomas L. Gray, Matthew W. Smith, Lucy E. Cohan, and David W. Miller. Minimizing high spatial frequency residual in active space telescope mirrors. *Proc. SPIE*, 7436, 2009.
- [33] Joseph J. Green, Bruce H. Dean, Catherine M. Ohara, David C. Redding, and Yan Zhang. Target selection and imaging requirements for JWST fine phasing. *Proc. SPIE*, 5487, 2004.
- [34] Simon C. O. Grocott. *Dynamic Reconstruction and Multivariable Control for Force-Actuated, Thin Facesheet Adaptive Optics*. PhD thesis, Massachusetts Institute of Technology, 1997.
- [35] Suresh T. Gulati and Mary J. Edwards. ULE - Zero expansion, low density, and dimensionally stable material for lightweight optical systems. *Proc. SPIE*, CR67:107–136, 1997.
- [36] Eugene Hecht. *Optics*. Addison Wesley, 4th edition, 2002.
- [37] Elizabeth Jordan. Design and shape control of lightweight mirrors for dynamic performance and athermalization. Master’s thesis, Massachusetts Institute of Technology, 2007.
- [38] Elizabeth Jordan and David W. Miller. Primary mirror shape control for athermalization using embedded sensors. *Proc. SPIE*, 6687, 2007.

- [39] M. Lampton and M. Sholl. Comparison of On-Axis Three-Mirror-Anastigmat Telescopes. *Proc. SPIE*, 6687, 2007.
- [40] John C. Mather. The James Webb Space Telescope and future IR space telescopes. *AIAA Space*, 5985, September 2004.
- [41] Gregory J. Michels. Personal communication, October 2009.
- [42] David W. Miller and Simon C. O. Grocott. Robust control of the Multiple Mirror Telescope adaptive secondary mirror. *Opt. Eng.*, 38(8):1276–1287, August 1999.
- [43] Maureen L. Mulvihill and Mark A. Ealey. Large mirror actuators in the 21<sup>st</sup> century. *Proc. SPIE*, 5166:197–206, 2004.
- [44] NASA. Hubble Space Telescope primary mirror. *NASA Image Exchange (NIX)*, MSFC-8109563, 1981.
- [45] NASA. Hubble Space Telescope and Earth limb. *NASA Image Exchange (NIX)*, GPN-2000-001064, 1997.
- [46] H. F. Nied and A. A. Rudmann. Temperature induced distortions in space telescope mirrors. *Proc. AIAA Aerospace Sciences*, January 1993.
- [47] Catherine M. Ohara, Jessica A. Faust, Andrew E. Lowman, Joseph J. Green, David C. Redding, Scott A. Basinger, David Cohan, and Fang Shi. Phase Retrieval Camera optical testing of the Advanced Mirror System Demonstrator (AMSD). *Proc. SPIE*, 5487:954–962, 2004.
- [48] Ben R. Oppenheimer, Dean L. Palmer, Richard G. Dekany, Anand Sivaramakrishnan, Mark A. Ealey, and Thomas R. Price. Investigating a Xinetics Inc. deformable mirror. *Proc. SPIE*, 3126:569–579, 1997.
- [49] Kang-Soo Park, Jun Ho Lee, and Sung-Kie Youn. Lightweight mirror design method using topology optimization. *Opt. Eng.*, 44(5), May 2005.
- [50] Thomas Parsonage. JWST beryllium telescope: Material and substrate fabrication. *Proc. SPIE*, 5494:39–48, 2004.
- [51] Ronald S. Polidan. Hubble Space Telescope overview. *29<sup>th</sup> AIAA Aerospace Sciences Meeting*, January 1991.
- [52] David Redding, Scott Basinger, David Cohen, Andrew Lowman, Fang Shi, Pierre Bely, Chuck Bowers, Richard Burg, Laura Burns, Pamela Davila, Bruce Dean, Gary Mosier, Todd Norton, Pete Petrone, Brendon Perkins, and Mark Wilson. Wavefront control for a segmented deployable space telescope. *Proc. SPIE*, 4013:546–558, 2000.
- [53] Timothy Reed, Stephen E. Kendrick, Robert J. Brown, James B. Hadaway, and Don Byrd. Final results of the Subscale Beryllium Mirror Demonstrator (SMBD) program. *Proc. SPIE*, 4451:5–14, 2001.

- [54] Daniel J. Schroeder. *Astronomical Optics*. Academic Press, 2nd edition, 2000.
- [55] Jim Schwiegerling and Daniel R. Neal. Historical development of the shack-hartmann wavefront sensor. *Robert Shannon and Roland Shack, Legends in Applied Optics, SPIE Press*, pages 132–139, 2005.
- [56] Bernard D. Seery. The James Webb Space Telescope (JWST): Hubble’s scientific and technological successor. *Proc. SPIE*, 4850:170–178, 2003.
- [57] R. B. Shack and B. C. Platt. Production and use of a lenticular Hartmann screen. *J. Opt. Soc. Am.*, 61(5):656, 1971.
- [58] Michael J. Shepherd, Richard G. Cobb, Anthony N. Palazotto, and William P. Baker. Modal transformation method for deformable membrane mirrors. *Journal of Guidance, Control, and Dynamics*, 32(1):276–289, 2009.
- [59] H. Philip Stahl. JWST lightweight mirror TRL-6 results. *Proc. IEEE Aerospace Conference*, pages 1–12, 2007.
- [60] H. Philip Stahl. JWST mirror technology development results. *Proc. SPIE*, 6671, 2007.
- [61] Inc. The Math Works. Matlab product help. *Ver. 7.4.0.287*, 2007.
- [62] Michael E. Thomas. Infrared- and millimeter-wavelength continuum absorption in the atmospheric windows: Measurements and models. *Infrared Physics*, 30(2):161–174, 1990.
- [63] Scott A. Uebelhart. Conditioning, reduction, and disturbance analysis of large order integrated models for space-based telescopes. Master’s thesis, Massachusetts Institute of Technology, 2001.
- [64] Scott A. Uebelhart. *Non-Deterministic Design and Analysis of Parameterized Optical Structures during Conceptual Design*. PhD thesis, Massachusetts Institute of Technology, 2006.
- [65] Scott A. Uebelhart, Deborah Howell, and David W. Miller. Evaluating alternative architectures for lightweight space telescope parameterized models. *Proc. IEEE Aerospace Conference*, 2006.
- [66] S. E. Winters, J. H. Chung, and S. A. Velinsky. Modeling and control of a deformable mirror. *Journal of Dynamic Systems, Measurement, and Control*, 124:297–302, June 2002.
- [67] Xinetics. Agile production of SiC mirrors. *NASA Technology Days, Marshall Space Flight Center*, September 2003.